ABSTRACT

CHARACTERIZATION AND FABRICATION OF α(6H)-SIC AS A PIEZORESISTIVE PRESSURE SENSOR FOR HIGH TEMPERATURE APPLICATIONS

by
Robert Sylvester Okojie

A prototype monolithic 6H-SiC pressure sensor operational up to 350°C, with potential to operate up to 600°C, was batch fabricated and tested. At temperatures higher than 450°C, silicon diaphragms creep under minimal load. To operate beyond 450°C, therefore, the use of 6H-SiC was proposed. However, three key technological issues - fabrication, high temperature metallization, and gage factor characterization - had to be resolved. Since conventional fabrication technology is not applicable to SiC due to its near inert chemistry, photoconductive selectivity techniques to etch the piezoresistors were developed. Techniques to wet etch the cavities in a dark current mode were developed, resulting in 25μm diaphragms free of etch-pits and hillocks. Average etch-rates between 0.6 and 0.8μm/min. were achieved. Ti/TiN/Pt and Ti/$TaSi_2$/Pt multilayer metallization schemes that maintained stable contact resistivity on n-type 6H-SiC epilayers after more than twenty hours of heat treatment at 600°C in air were demonstrated. The characterization research revealed that the longitudinal and transverse gage factors were -22 and 19, respectively, at room temperature. They increased in absolute values with temperature, and then assumed constant values of 11 and 9, respectively, above 400°C. The experimental data obtained demonstrated for the first time that 6H-SiC pressure sensors capable of operating up to 600°C can be fabricated and manufactured.

CHARACTERIZATION AND FABRICATION OF α(6H)-SiC AS A PIEZORESISTIVE PRESSURE SENSOR FOR HIGH TEMPERATURE APPLICATIONS

by
Robert Sylvester Okojie

A Dissertation
Submitted to the Faculty of
New Jersey Institute of Technology
in Partial Fulfillment of the Requirements for the Degree of
Doctor of Philosophy

Department of Electrical and Computer Engineering

May 1996

APPROVAL PAGE

CHARACTERIZATION AND FABRICATION OF α(6H)-SIC AS A PIEZORESISTIVE PRESSURE SENSOR FOR HIGH TEMPERATURE APPLICATIONS

by
Robert Sylvester Okojie

Dr. William N. Carr, Dissertation Advisor — Date
Professor, Department of Electrical and Computer Engineering and Physics
Director, Microelectronics Research Center, NJIT.

Dr. Roy H. Cornely, Committee Member — Date
Professor of Electrical and Computer Engineering, NJIT

Dr. Robert B. Marcus, Committee Member — Date
Research Professor, Department of Electrical Engineering, NJIT

Dr. Roland Levy, Committee Member — Date
Professor, Department of Physics, Materials Science Division, NJIT

Dr. Anthony D. Kurtz, Committee Member — Date
Chairman, Kulite Semiconductor Products, Inc., Leonia, NJ.

Dr. Lawrence G. Matus, Committee Member — Date
Senior Research Scientist, NASA Lewis Research Center, Cleveland, OH.

BIOGRAPHICAL SKETCH

Author: Robert Sylvester Okojie

Degree: Doctor of Philosophy

Date: May 1996

Undergraduate and Graduate Education

- Doctor of Philosophy in Electrical Engineering
  New Jersey Institute of Technology, Newark, NJ, 1996
- Master of Science in Electrical Engineering
  New Jersey Institute of Technology, Newark, NJ, 1993
- Bachelor of Science in Electrical Engineering
  New Jersey Institute of Technology, Newark, NJ, 1992
- National Diploma in Communication,
  School of Communications, Lagos, Nigeria, 1982

Major: Electrical Engineering

Presentations and Publications

Okojie, Robert S. Alexander A. Ned, Anthony. D. Kurtz, and William N. Carr
"α(6H)-SiC Pressure Sensors for High Temperature Applications." IEEE-MEMS 96. The Ninth International Workshop on Microelectromechanical Systems. San Diego, CA. Feb. 10-14, 1996

Okojie Robert. S.,
"6H-SiC Pressure Sensor for High Temperature Applications". Bi-Annual Seminar for NASA Phase II SBIR Contract # NAS3-027011. NASA Lewis, Cleveland, OH. 1995.

Shor, J. S., R. S. Okojie, and A. D. Kurtz,
"Photoelectrochemical Etching of n-type 6H- SiC". Institute of Physics Conference Series Number 137, Chapter 6, pp 523-526

To the memory of my late wife, Debbie, and to those that hang in there and survive.

ACKNOWLEDGMENT

I wish to thank NASA-Lewis for awarding the Phase II SBIR contract to Kulite Semiconductor Products.

My deepest appreciation goes to Dr. Anthony D. Kurtz, the chairman of Kulite Semiconductor Products, Leonia, NJ, for thrusting upon me the challenge to implement the objectives of this project.

My gratitude to Dr. William N. Carr for giving me the opportunity to be his graduate student.

At Israel Institute of Technology, Technion, many thanks go to Dr. Ben Weiss for his technical support and editing the NASA final report, and Dr. Ilana Grimberg for the Auger Electron Spectroscopy(AES) analysis.

At Kulite, the full and continuous support of Alex Ned, Director of Sensor Operations is greatly appreciated. I am grateful to the entire staff of department 200 with special reference to Gary Provost for metallization/dielectric depositions and other equipment support, to Mahesh Patel for support in testing the sensors, to Scott Goodman for material support in testing the sensors.

TABLE OF CONTENTS

TABLE OF CONTENTS

LIST OF TABLES

LIST OF FIGURES

Figure **Page**

Figure **Page**

Figure **Page**

CHAPTER 1

INTRODUCTION

1.1 Objectives

In September 1993 a research program entitled "6H-SiC Pressure Sensors for High Temperature Applications - Phase II" was initiated under sponsorship of NASA (contract # NAS3-2701). The main objective of this program was to develop and characterize prototype 6H-SiC monolithic pressure sensor capable of operation at 600°C for minimum of 10 hours. At large, the scope of the work included an investigation of key processes and fabrication steps that, when integrated, would lead to successful completion of the main goal.

1.2 Tasks

The research and the development program was subdivided into specific tasks. The objective of Task I was experimental evidence that the developed ohmic contact metallization scheme would be capable to endure for at least 10 hours at 600°C with minimum allowable degradation of the contact resistivity. The deliverable for Task II was experimental data on the longitudinal and transverse gage factors of 6H-SiC as a function of temperature and doping level, as well as, data on temperature coefficient of resistivity (TCR) as a function of doping level and temperature. The testing range of the latest was set between room temperature and 600°C. The objective of Task III was experimental demonstration of a capability to thin uniformly SiC substrates applying photoelectrochemical etching at etch rates of about 1μm/min. The aim of Task IV was

fabrication and characterization of a diaphragm SiC pressure sensor complete with sensor packaging. The maximum operational temperature for testing was set as 600°C. The purpose of this task was also to identify fabrication problematic areas. The deliverable of Task V could be subdivided into two parts: a) fabrication of 6H-SiC pressure sensor on a substrate material and proving that the mounting technique can be applicable for sensor operation from room temperature to 600°C and survive at least 10 hours and, b) mounting of the sensor/substrate assembly (part a) into housing hardware and testing at 600°C for endurance for at least 10 hours. The objective of Task VI was consolidation of all the experimental and theoretical data acquired in Task I to V to assemble and test the SiC pressure sensor at temperatures up to at least 600°C for time period of at least 10 hours. Six SiC sensors had to be delivered to NASA (three that had not undergone the testing and three that have undergone the testing). The goal of Task VII were all aspects of reliability inspection.

In Phase I of this program[1], the feasibility of 6H-SiC sensors was established. This doctoral dissertation was essentially to implement Phase II of the project, which was devoted to the evaluation of 6H-SiC as a piezoresistor, to the development of a new micromachining processes, and to the fabrication and testing of the new generation of high temperature pressure transducers for operation up to 600°C. The objective of Phase II of this program was to develop and characterize high temperature monolithic pressure transducers. In the initial stage, novel process technology developed in Phase I was extended to micromachine thin sensor diaphragms in 6H-SiC. The piezoresistive properties of SiC were investigated, as a function of doping type and levels to determine

the optimal parameters for sensing elements. Subsequently, using the established SiC microfabrication processes, detailed later, first generation prototype SiC transducers were fabricated for the temperature regime 25-300°C. Concurrent with this, innovative new high temperature SiC metallization systems, were developed. The final stage was devoted to detailed characterization and improvement of the structural properties of the sensor in an effort to extend the operation temperature to 600°C. To accomplish the objectives, the following studies were embarked upon:

I. High temperature metallization;

II. Piezoresistivity and temperature coefficient of resistivity evaluation;

III. SiC wafer thinning;

IV. Low temperature (<500 C) prototype SiC pressure sensors;

1.3 Why 6H-SiC?

Semiconductor sensing elements are distinguished by large piezoresistive coefficients and therefore have been applied extensively in the measurement of pressure, strain, flow, acceleration and force. Silicon pressure sensors have been developed using pn-junction isolated piezoresistors for low temperatures (<175°C)[2] and dielectrically isolated elements for high temperatures (up to 450°C)[3]. However, at higher temperatures silicon undergoes creep under minimal load which makes it unsuitable for sensor applications[4]. Control of operating conditions in many engineering systems requires pressure measurements at temperatures exceeding maximum usable range of silicon transducers. Typical examples are aeronautical propulsion systems, wind tunnels, nuclear power plants,

materials processing and space technology. To meet these needs, new innovative processes were proposed to develop 6H-SiC as a high temperature sensor material.

Silicon carbide has long been viewed as a potentially useful semiconductor for high temperature application. A general comparison between the popular and conventional silicon crystal and silicon carbide is shown in Table 1. Its excellent electrical characteristics - wide-bandgap of about 3eV, high-breakdown electric field, and high electron saturation drift velocity - makes it a superior candidate for high-temperature electronic applications. Furthermore, SiC exhibits excellent thermal and mechanical properties at high temperature[5] and large piezoresistive coefficients, a combination which makes it suitable for electromechanical sensing at high temperatures beyond the capability of conventional silicon technology.

Table 1-1 Comparison of properties of α-(6H)-SiC with silicon

Properties	**Silicon**	**α(6H)-SiC**
Bandgap(eV)	1.12	~3
Melting Point(°C)	1420	>1800
Breakdown Voltage ($x10^6 Vcm^{-1}$)	.3	2.5
Young's modulus of elasticity(GPa)	165	448
Thermal Conductivity [$W(cm^0C)^{-1}$]	1.5	5
Electron Saturation Velocity($x10^7 cms^{-1}$)	1	2
Maximum Operating Temperature(°C)	300	1240

CHAPTER 2

DESIGN CONSIDERATIONS OF THE SENSOR

2.1 Overview

Generally, the design of devices that sense physical phenomena and electrical readouts call for the interpolation of two or more kinds of mathematical relationships. In the design of the proposed high temperature pressure sensor, the equations that explain the physical phenomena, (i.e. pressure and diaphragm deflection) are interpolated with equation of the output voltage. The equations of deflecting diaphragms are in two categories. One supports maximum diaphragm deflections less than its thickness while the other supports diaphragms with maximum deflections larger than its thickness. One fundamental reason for having separate expressions has to do with the problem of linearity in membrane deflection. It was found that there was need to restrict the maximum deflection to less than the membrane thickness for applications of short range pressure measurement in order to preserve a reasonable degree of linearity of diaphragm deflection in response to applied pressure. For wide band pressure measurements, however, the deflection of the diaphragm in response to applied pressure is no longer linear. For the device to be used continuously over a long period of time, the membrane must be capable of responding to applied pressure with precision and with little hysterisis. To achieve this, the membrane must retain its elastic property after applied maximum pressure differential. To that effect, there is need to choose materials with an appreciable linear region on the Stress-Strain curve shown in Fig. 2-1. In this figure, for the diaphragm to retain its elastic

integrity, the stress induced by pressure must not exceed point A (yield point). In essence, the operating point should swing between O and A. If the stress reaches point D (elastic limit), there is very strong likelihood the diaphragm would lose its elasticity and become permanently deformed.

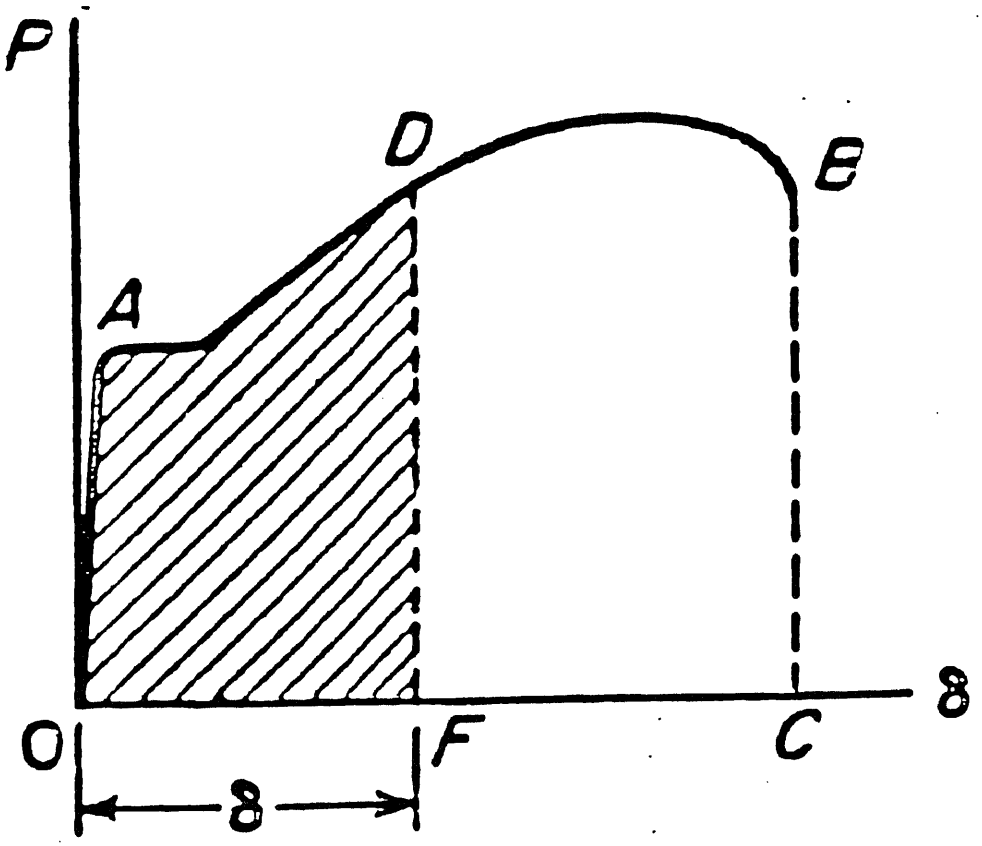

Figure 2-1
Typical Stress-Stress curve(Hooke's Law)

When the maximum deflection, w, of a clamped circular plate is less than its thickness, the equation that describes it is expressed as[6]

$$w = 0.89\frac{Pa^4}{64D} \tag{2-1}$$

where P is the applied pressure,

D is the flexural rigidity of the membrane material and is expressed as:

$$D = \frac{Et^3}{12\left(1-\upsilon^2\right)} \tag{2-2}$$

where v is the Poisson constant, E is the Young's modulus, and t = membrane thickness. The total stress on the membrane associated with such small deflection is expressed as:

$$\left(\sigma_r\right)_r = \frac{3}{4}\frac{Pa^2}{t^2} \tag{2-3}$$

The choice of large or small deflection equation, as stated before, is basically dictated by device application. A deflection and stress analysis is conducted on small deflections. Figure 2-2 shows the theorectical deflection of a circular 6H-SiC diaphragm in response to applied pressure. For a membrane deflection of 5μm,the maximum applied pressure differential is approximately 7MPa for 6H-SiC membrane of thickness, t = 25μm; radius, a = 440μm, for a Poisson constant of 0.3.

In the first generation of high temperature transducers developed at Kulite a circular diaphragm geometry was utilized. A circular diaphragm can be easily mounted and in the case of materials with high elastic moduli, high pressures can be applied on diaphragms with reasonable ratios between the diameter and thickness. According to the theory of plates and shells by Timoshenko[6] the radial and tangential stresses at any point on the front side of a circular, edges fixed, diaphragm (Fig.2-3) can be respectively related to the applied pressure on the front of the diaphragm, its thickness, radius and the distance from the center of the point of interest as[6]:

$$\sigma_r = \frac{3}{4}\frac{Pa^2}{t^2}\left[(3m+1)\frac{r^2}{a^2} - (m+1)\right] \tag{2-4}$$

and

$$\sigma_t = \frac{3}{4}\frac{Pa^2}{t^2}\left[(m+3)\frac{r^2}{a^2} - (m+1)\right] \tag{2-5}$$

where P is the total applied pressure; t is the diaphragm thickness; a is the diaphragm radius; r is the radial distance from the center of a circular plate, and m is the reciprocal of Poisson's ratio. The same set of equations can be used to define stresses on the back of the diaphragm, where pressure is applied, but with negative sign. A simple analysis of the radial and tangential stress distribution on the front side of the diaphragm shows, that both stresses change (as a result of applied pressure from the front side) at a certain distance from the center of the diaphragm from compressive to tensile, as shown in Fig. 2-4. The magnitude of the deflection of the center of the diaphragm where a uniform pressure is impressed on the diaphragm is given by:

$$\omega_c = \frac{3}{16}\frac{Pa^4}{Et^3}\left(1-\upsilon^2\right) \tag{2-6}$$

Any piezoresistor, on the back or on the front side of the diaphragm, diffused or etched from an epitaxially grown layer, will be subjected, depending on its location, as a result of applied pressure on the front side, to parallel and perpendicular stresses. The functional relationship between the fractional change in electrical resistance (ΔR/R) of the piezoresistor and the perpendicular and parallel stress components is given by:

$$\frac{\Delta R}{R} = \Pi_t \sigma^{''} + \Pi_l \sigma^{'} \tag{2-7}$$

where Π_t and Π_r are parallel and perpendicular piezoresistive coefficients, respectively and σ^{II} and $\sigma^{\perp}$ are parallel and perpendicular stress components, respectively. For tangentially and radially oriented piezoresistors e.g. diffused or etched on a circular diaphragm, whose radius is large as compared with the resistor dimensions, this fractional change in resistance can be expressed as follows:

for tangential resistors:

$$\left(\frac{\Delta R}{R}\right)_t = \Pi_t \sigma_t + \Pi_r \sigma_r \tag{2-8}$$

and for radial resistors:

$$\left(\frac{\Delta R}{R}\right)_r = \Pi_t \sigma_r + \Pi_r \sigma_t \tag{2-9}$$

According to *Samaun* [7] the parallel and perpendicular piezoresistive constants for cubic structure can be expressed for n-type and p-type dopings in terms of two independent dominant piezoresistive coefficients Π_{11} and Π_{44} (see eq's 2-10 and 2-11): (Π_{11} and Π_{44} are the main constants in the piezoresistance tensor)

n-type:

$$\Pi_t = \Pi_{11} [1 - 3 (l_1^2 m_1^2 + l_1^2 n_1^2 + m_1^2 n_1^2)] \tag{2-10a}$$

$$\Pi_r = \Pi_{11} [-1/2 + 3/2 (l_1^2 l_2^2 + m_1^2 m_2^2 + n_1^2 n_2^2)] \tag{2-10b}$$

p-type:

$$\Pi_t = 2\Pi_{44} [(l_1^2 m_1^2 + l_1^2 n_1^2 + m_1^2 n_1^2)] \tag{2-11a}$$

$$\Pi_r = \Pi_{44} [(l_1^2 l_2^2 + m_1^2 m_2^2 + n_1^2 n_2^2)] \tag{2-11b}$$

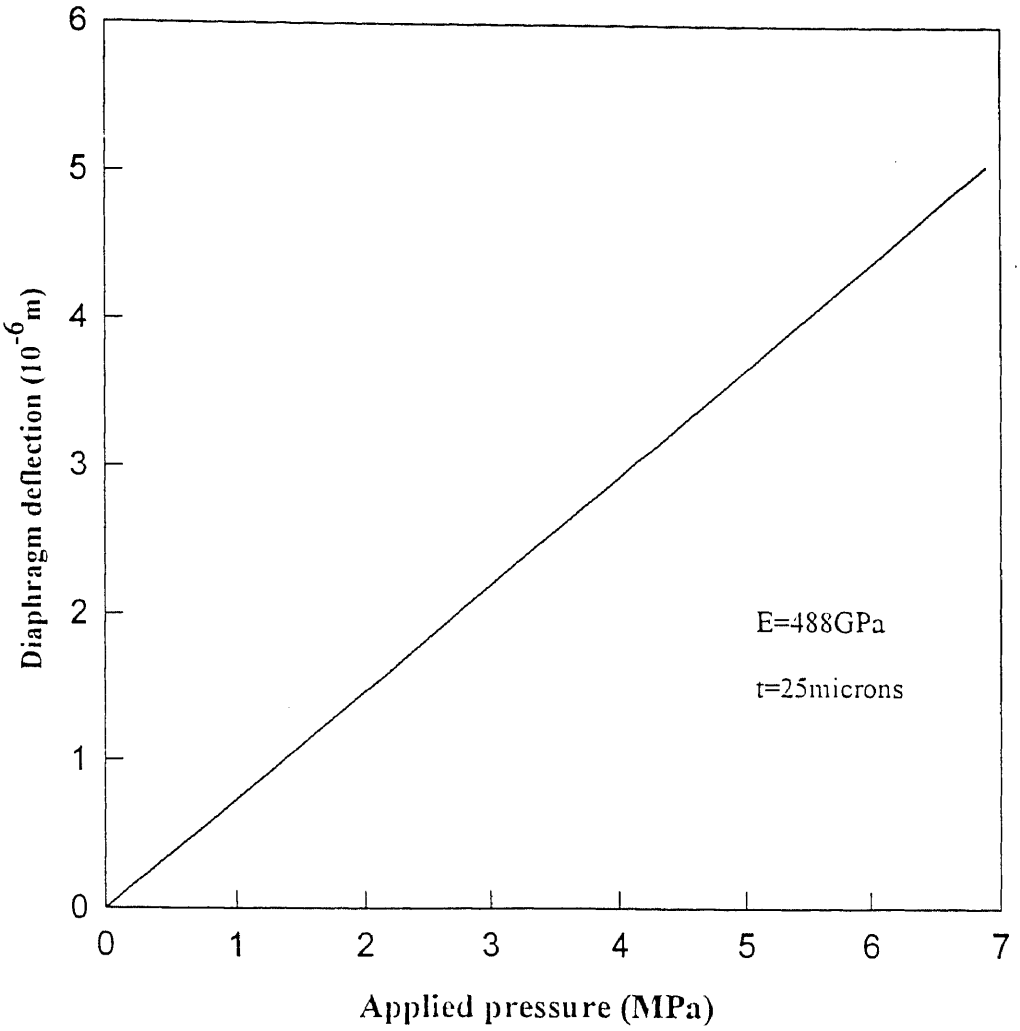

Figure 2-2
Maximum (6H)-SiC membrane deflection as function of applied pressure.

Where l, m, and n, are the directional cosines of a vector parallel to the resistors with respect to the crystallographic direction and l_2 m_2 and n_2 are the direction cosines of a

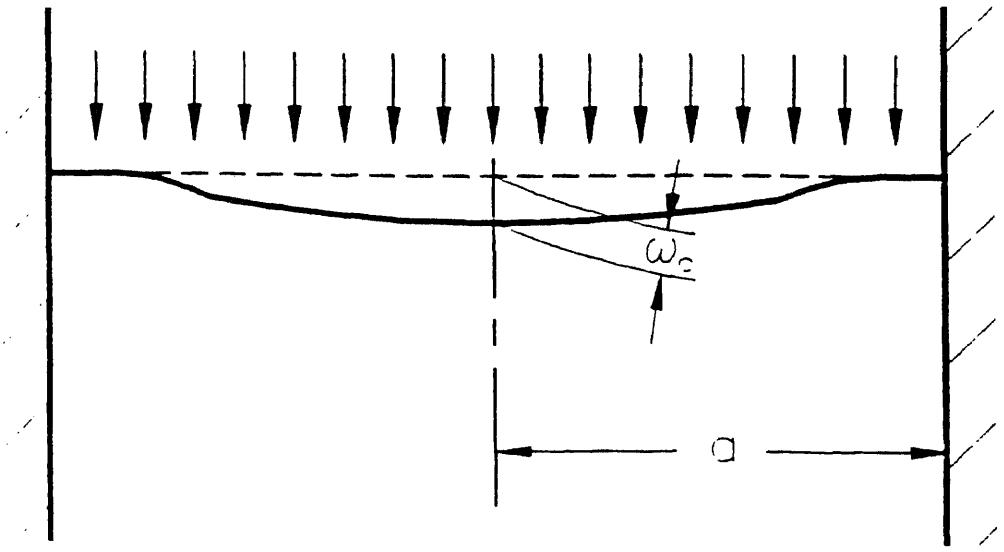

Figure 2-3
Uniformly loaded circular, edges fixed, diaphragm.

vector perpendicular to the resistors also with respect to the crystallographic direction. Usually, the subscripts 1 and 2 refer to current and stress measurement directions. In this manner the piezoresistive behavior can be predicted for any measurement direction. Further analysis shows that in a cubic structure for n-type resistors, diffused or etched from epitaxially grown layer, one of the most efficient configurations will be a bridge with four active resistors; two of which are located radially or tangentially near the center of the diaphragm in either [100] or [110] directions and two radial resistors in the [100] directions far from the center.

In the case of hexagonal structure such as 6H-SiC the problem is much more complicated in terms of resolving the piezoresistive constants in different directions.

Earlier efforts by Russian scientists[8, 9, 10, 11] to characterize the piezoresistance of 6H-SiC as function of crystallographic orientation resulted in differences in the obtained values.

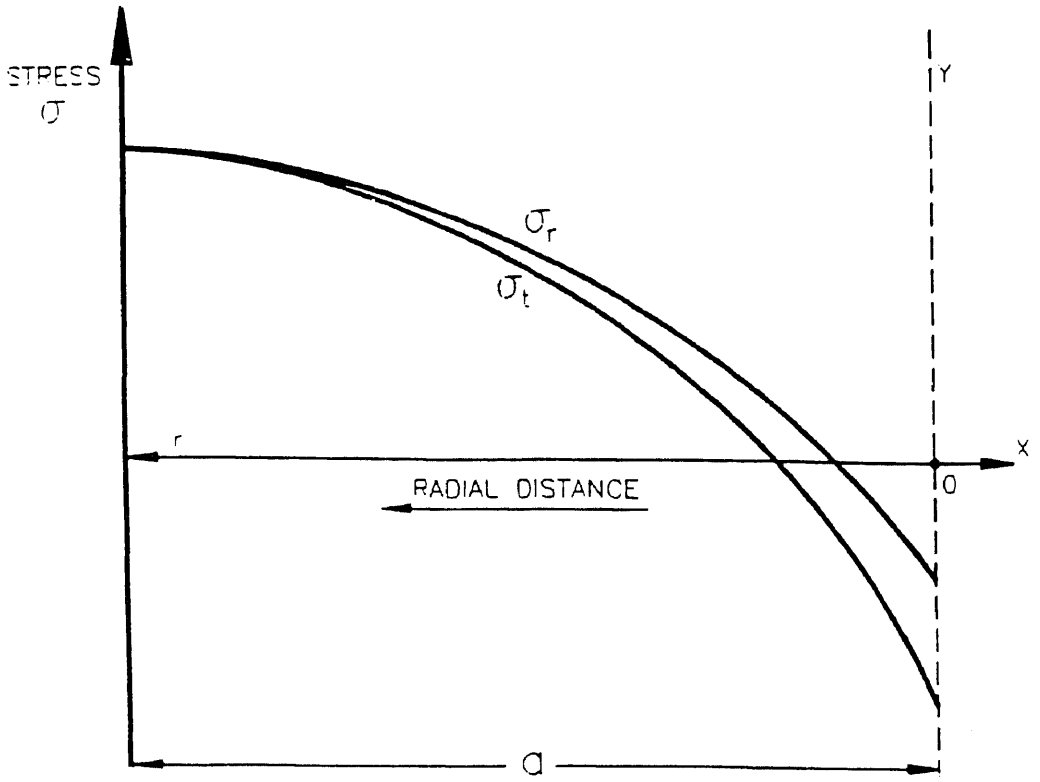

Figure 2-4
Radial and Tangential stresses on the front side of a diaphragm resulting from applied pressure from the front.

One reason was the inherent imperfections of the Lely platelets, which was the only crystal of choice then. Recent advances in SiC technology has led to the mass production of high quality SiC wafers of various polytypes by Cree Research[12], making it possible to obtain more reliable results.

2.2 Intergrated Metal Diaphragm-Piezoresistve Beam Description

In this work, the choice of the most suitable piezoresistive orientation, geared toward obtaining the highest gage factor, was based on a series of experiments. These experiments were conducted using resistors arranged in a wheatstone bridge configuration as shown in fig. 2-5. The resistors were etched in 6H-SiC epilayer (p- or n-type) by photoelectrochemical means to be described later on. The configuration of the resistors were such that two legs were oriented transversely while the other two in longitudinal orientation. The substrate was then diced into rectangular chips, each containing a pair of wheatstone bridges. The purpose was to place one bridge in tension and the other in compression in other to simultaneously compare the obtained results.

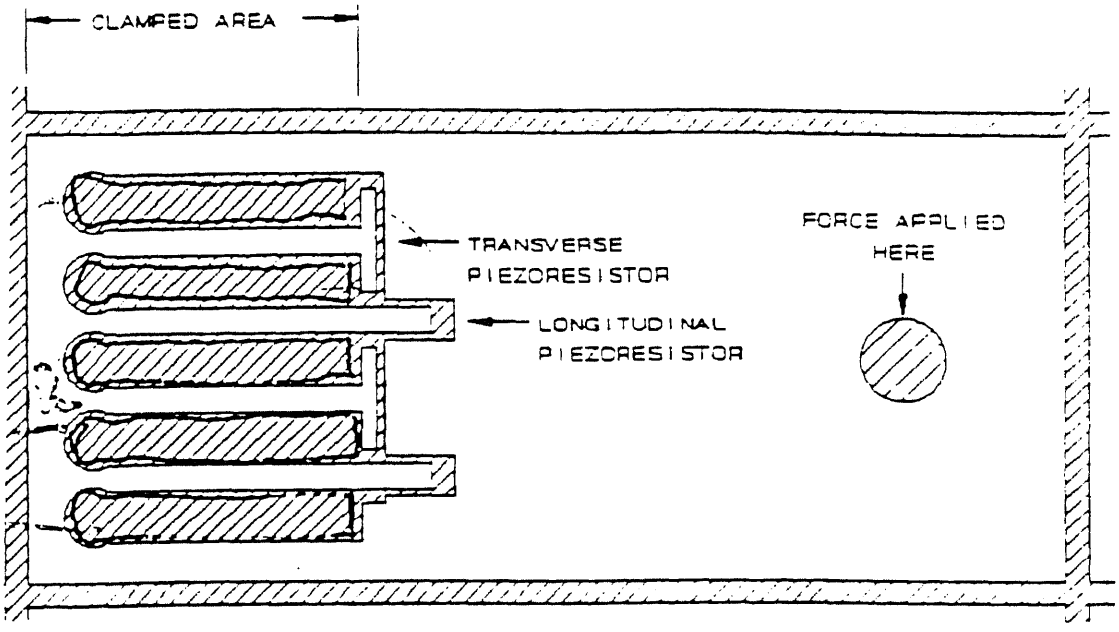

Figure 2-5
Top view schematic diagram of 6H-SiC beam with resistors in wheatstone configuration.

Figure 2-6 shows a schematic of a SiC integrated beam containing two longitudinal and two transverse piezoresistors. The actual beam used in this experiment was double the length shown, and contained two sets of sensors. The metal diaphragm, made of Incoloy[13], attached to the beam is also shown in cross section. Pressure was applied to the diaphragm through a port (not shown), which caused the diaphragm to deflect the beam. One set of piezoresistors, which is closer to the center of the metal diaphragm, was placed in tension, while the other, closer to the periphery of the diaphragm, was in compression. The ΔR of each arm of the bridge was measured in order to obtain the longitudinal and transverse gage factors(GF), which is expressed as:

$$GF = \frac{\Delta R}{R\varepsilon} \tag{2-12}$$

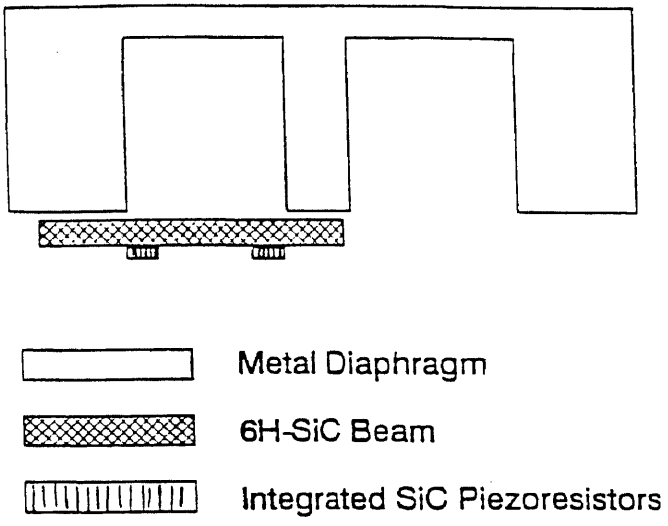

Figure 2-6
Cross section view of beam integrated with metal diaphragm

In this work, all the samples were uniaxially deformed perpendicular to the crystal's basal plane, which is the [0001] direction.

The beam transducer was been built and modeled in order to determine the gage factor of the samples. Since the beam was integrated with the metal diaphragm, it was necessary to calculate the strain and stresses on the surface of the beam and to analyze their distribution across the beam. The problem was solved as a superposition of two systems namely: a) edge fixed diaphragm and b) beam with one edge fixed (clamped) and the second edge guided. Deflection at the center resulting from uniform loading (pressure) on the front of the metal diaphragm is expressed previously (see eq.2-1) as:

$$w_c{}^P = \frac{Pa^4}{64D}$$

Deflection at the center resulting from a concentrated load at the center of the diaphragm

$$w_c{}^F = \frac{Fa^2}{16\pi D} \tag{2-13}$$

where F - concentrated load;

$$D = \frac{E_d t^3}{12\left(1-\upsilon^2\right)},$$

where E_d represents the Young' modulus of the diaphragm, and t is the metal diaphragm thickness. The net deflection resulting from combined loading, when the concentrated load acts in the opposite direction of the applied pressure is determined by:

$$w_{net.} = w_c{}^P - w_c{}^F = \frac{a^2}{16D}\left(\frac{Pa^2}{4} - \frac{F}{\pi}\right) \tag{2-14}$$

Deflection of a beam fixed (clamped) on one end, "guided" on the other (guided means that the slope at the guided point is always zero, but deflection is allowed and may change). This problem was solved by applying the Castigliano[14] method:

$$w_b = \frac{Fl^3}{12E_b I_b} \tag{2-15}$$

where w_b = beam deflection(in.); l = length of the beam(in); E_b = modulus of elasticity of the beam(psi); I_b = moment of inertia of the beam, expressed as:

$$I_b = \frac{bh^3}{12} \tag{2-16}$$

where b = beam width(in); h = beam thickness(in).

During loading, the deflection of the beam will be equal to that of the diaphragm; therefore eqs. (2-14) and (2-15) can be set equal and solved for force F (which is contact force between the diaphragm and the beam). Since the radius of the diaphragm and the length of the beam are for all intent and purposes equal, the equation for F simplifies to:

$$F = \frac{3}{4}\left(\frac{Pa^2\pi E_b I}{4aD\pi - 3E_b I}\right) \tag{2-17}$$

The maximum strains occur at either end of the beam and are of opposite sign:

$$\varepsilon_{\max} = \frac{Fal}{4E_b I} \tag{2-18}$$

The stress at the edge of the beam can be calculated from Hook's Law:

$$\sigma_{\max} = \varepsilon_{\max} E_b \tag{2-19}$$

The dimensions of the bossed metal diaphragm are:

diaphragm thickness, t = 0.008in; Young's modulus, E_d = 30Mpsi; diaphragm radius, a = 0.16in., while that of the beam used throughout this program are:

beam thickness, h = 0.012in; beam length, l = 0.16in, beam width, b = 0.06in; beam Young's modulus. E_b = 60Mpsi. Based on these values, the strain in the SiC beam, calculated from the dimensions of the metal diaphragm, was roughly 7μstrain/psi.

Using the above modeling, it became possible to characterize calculate the gage factor of the (6H)-SiC material, since there is a direct relationship between the applied strain an gage factor.

CHAPTER 3

MECHANICAL AND ELECTRICAL CHARACTERIZATION

3.1 Measurement of Gage Factor(GF) and Temperature Coefficient of Resistivity(TCR)

The principle of piezoresistive effect is associated with changes in resistance as a result of applied mechanical signal. Based on this effect, strain gages were subsequently developed. When an object is mechanically strained, the bonded strain gage changes its resistance. The latter can be measured by incorporating the gage within a wheatstone bridge configuration and the resultant output voltage is related to the applied force. The piezoresistive effect is rather small in metals but in semiconductors it is much more pronounced. The explanation can be found in eq. (3-1) for the gage factor,

$$GF = \frac{dR}{R\varepsilon} = 1 + 2\upsilon + \frac{d\rho}{\rho}\varepsilon \tag{3-1}$$

where GF = gage factor; R = electrical resistance(Ω); ρ = electrical resistivity(Ω-cm) of the gage material, and ε= applied strain. As shown by eq. (3-1) the change of the resistance is dependent on two terms: one, which is associated with the geometrical piezoresistive effect, and second originating from the strain dependency of the resistivity. In metals this latter term is zero. In semiconductors, however, the contribution of the geometrical term to the gage factor is of the same order as in metals. Therefore, the size of the gage factor in semiconductors is related to the high strain sensitivity of the resistivity. This can be explained on the basis of the energy-band structure of semiconductors. Briefly, in multivalley n-type semiconductors such as 6H-SiC, the piezoresistive effect is associated with a change in the relative positions of the multivalley

minima under applied stress. This effect causes the electrons to transfer between the valleys, causing a net change in the mobility which in turn has a dominant effect on the strain (stress) dependency of the resistivity[15].

An important consideration in the selection of a resistor for high or low temperature applications is the way its electrical resistance changes with the temperature. Resistance variation with temperature is usually expressed as a temperature coefficient of resistivity(TCR), which is defined as:

$$TCR = \frac{1}{R_o}\frac{R_f - R_o}{T_f - T_o} \tag{3-2}$$

Where R_o = resistance at room or reference temperature; R_f = resistance at operating temperature T_o = room or reference temperature (usually given as 25°C or 80°F), and T_f = operating temperature. The TCR may be positive or negative and is usually given either in (ppm/°C) or in (%/°C). Practically it can be, to a certain degree, influenced by geometry as well as by processing variations. Earlier studies, reported in scientific and technical literature [10, 11], with regard to piezoresistive properties of SiC were carried out on highly irregular Lely crystals [16]. It was, therefore, decided to repeat some of the measurements on more perfect crystals grown by the modified sublimation method [17, 18, 19].

In the first stage the gage factor and TCR of n-type 6H-SiC were analyzed in the basal (0001) plane. Strain gages were produced from n-type SiC wafers with two doping levels namely: $2 \times 10^{17}cm^{-3}$ and $3 \times 10^{18}cm^{-3}$. It should be noted that in hexagonal crystals the piezoresistance tensor is isotropic in the basal (0001) plane, which permits the gage to

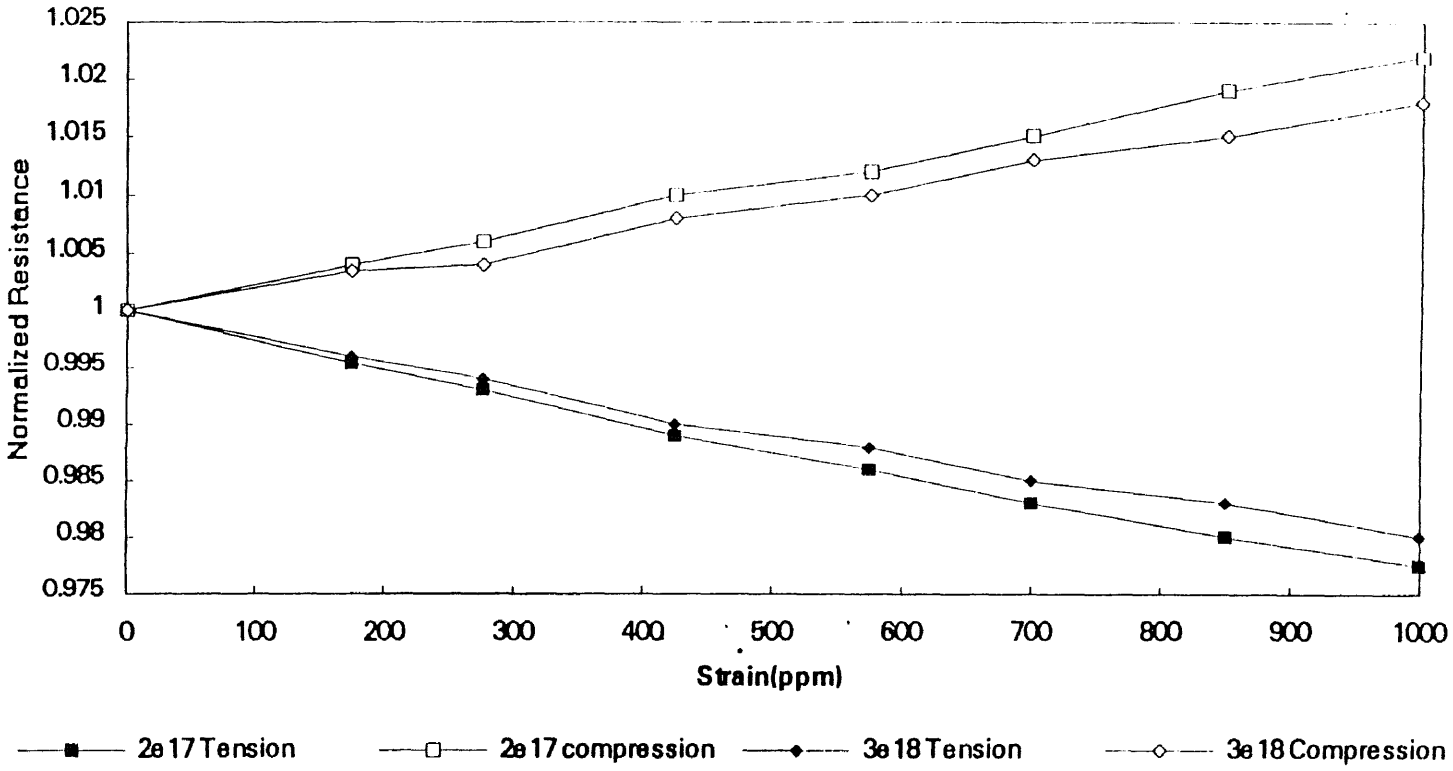

Figure 3-1:
Changes in resistivity vs. applied strain in longitudinal n-type 6H-SiC gages with two doping levels.

be rotated normal to the *c* axis without effecting the piezoresistivity [18]. Longitudinal and transverse gages were examined, corresponding to the piezoresistive coefficients Π_{11} and Π_{12}, respectively. Figure 3-1 shows change in the resistance vs. applied strain in longitudinal n-type gages for the two doping levels mentioned above. The established gage factors were approximately -25 for the lower doping level and -20 for the higher doping level. Measurements conducted on the transverse gage ($N_d = 3 \times 10^{18} cm^{-3}$) lead to a gage factor of approximately 11.

Initial experiments carried out at elevated temperatures <325°C lacked accuracy because of technical difficulties and therefore, the results should be considered as approximates only. However, it could be said with high probability that the gage factor decreases with an increase in temperature. Some initial conclusions could be drawn from the first experimental results. Increase in doping level results in a decrease of the gage factor. Similarly, an increase in temperature reduces the gage factor. Since the piezoresistive effect is an energy band transport phenomenon, factors such as impurities, donor level, mobility, defect density and overall quality of the crystal may influence the effect substantially. The piezoresistance coefficient Π_{11} was calculated from the relationship[8]:

$$\frac{dR}{R} = \Pi\sigma \tag{3-3}$$

and was found to be about -5.12×10^{-12} cm^2/dyne for the gage with the lower doping level and -4.3×10^{-12} cm^2/dyne for gage with the higher doping level.

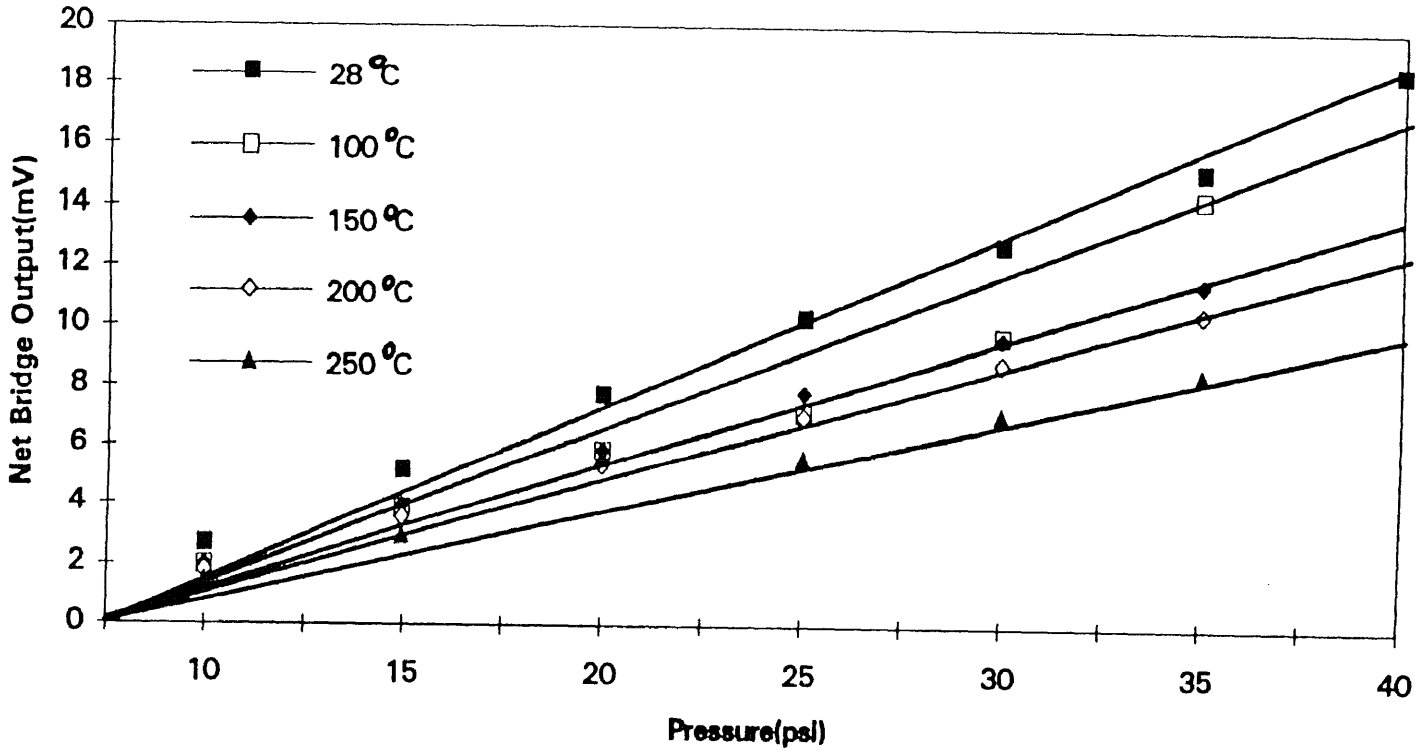

Figure 3-2

Net bridge output as a function of pressure at five different temperatures(n^+ 6H-SiC, $N_d=2x10^{19}/cm^3$)

The initial TCR measurements were carried out with a similar n-type 6H-SiC specimen. In the low doped material (N_d=1.8 x $10^{17}cm^{-3}$) the resistance decreased with temperature in the range between -60°C and room temperature. Above that temperature the resistance increased. The average TCR value for the range 25°C - 625°C was found to be 0.56%/°C. In the high doped samples (3 x $10^{18}cm^{-3}$) the resistance was observed to decrease up to 100°C and then increased. The average TCR value in the range 100°C - 625°C was found to be 0.28%/°C. The decrease in resistance with increase of temperature below a certain temperature limit, which typically lays between 0°C and 25°C, is associated with the process of ionization of impurities. Below this limit, the resistance is primarily controlled by extrinsic carrier generation. Once the impurities are ionized the resistance is primarily controlled by lattice scattering and increases with the temperature. Increase in the doping level results in reduction of TCR due to lattice scattering. In highly doped n-SiC the impurity ionization is completed at higher temperature possibly due to the large number of impurities and its wider bandgap.

In conclusion, it could be said, on the basis of the initial set of piezoresistivity and TCR measurements that the 6H-SiC has the potential to be applied in both high temperature and highly sensitive transducers.

3.2 Temperature Effect on Gage Factor

In the next stage of investigations, the piezoresistive properties of a SiC beam transducer were measured in the range of temperatures between 25°C and 250°C. They were carried out on a beam consisting of longitudinal and transverse 6H-SiC

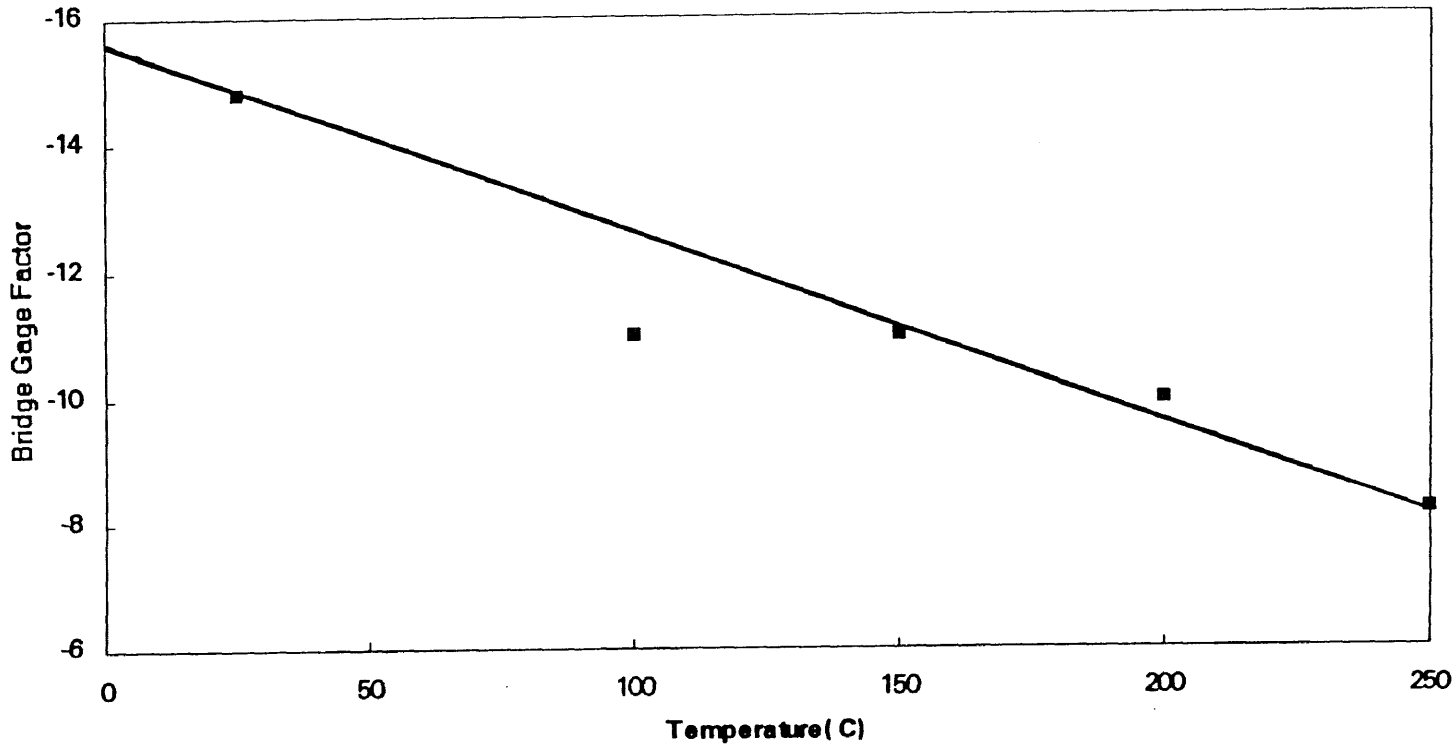

Figure 3-3

Bridge gage factor, GF, vs. temperature. It decreases linearly with temperature. (n^+ 6H-SiC, $N_d=2x10^{19}/cm^3$)

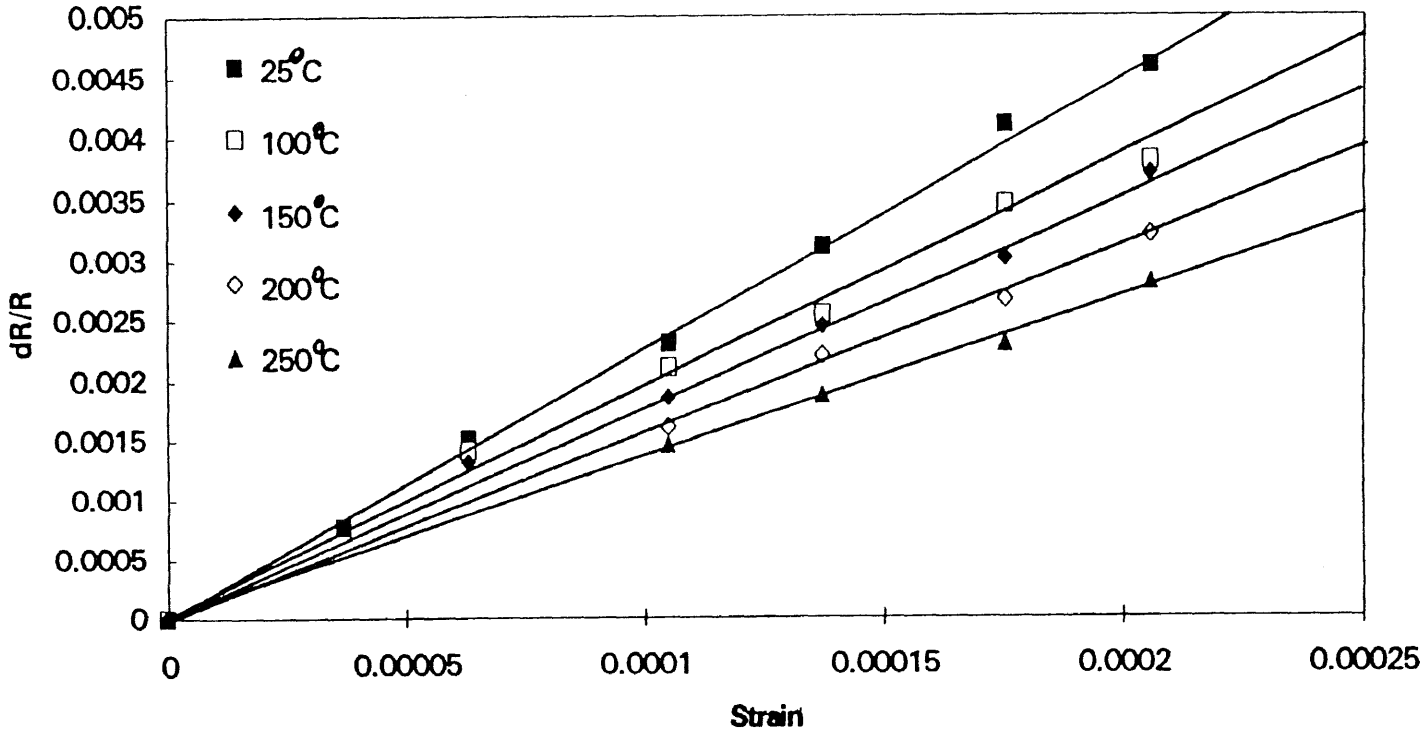

Figure 3-4
Relative change in resistance of the longitudinal piezoresistors as a function of strain at different temperatures. (n^+ 6H-SiC, $N_d=2x10^{19}/cm^3$)

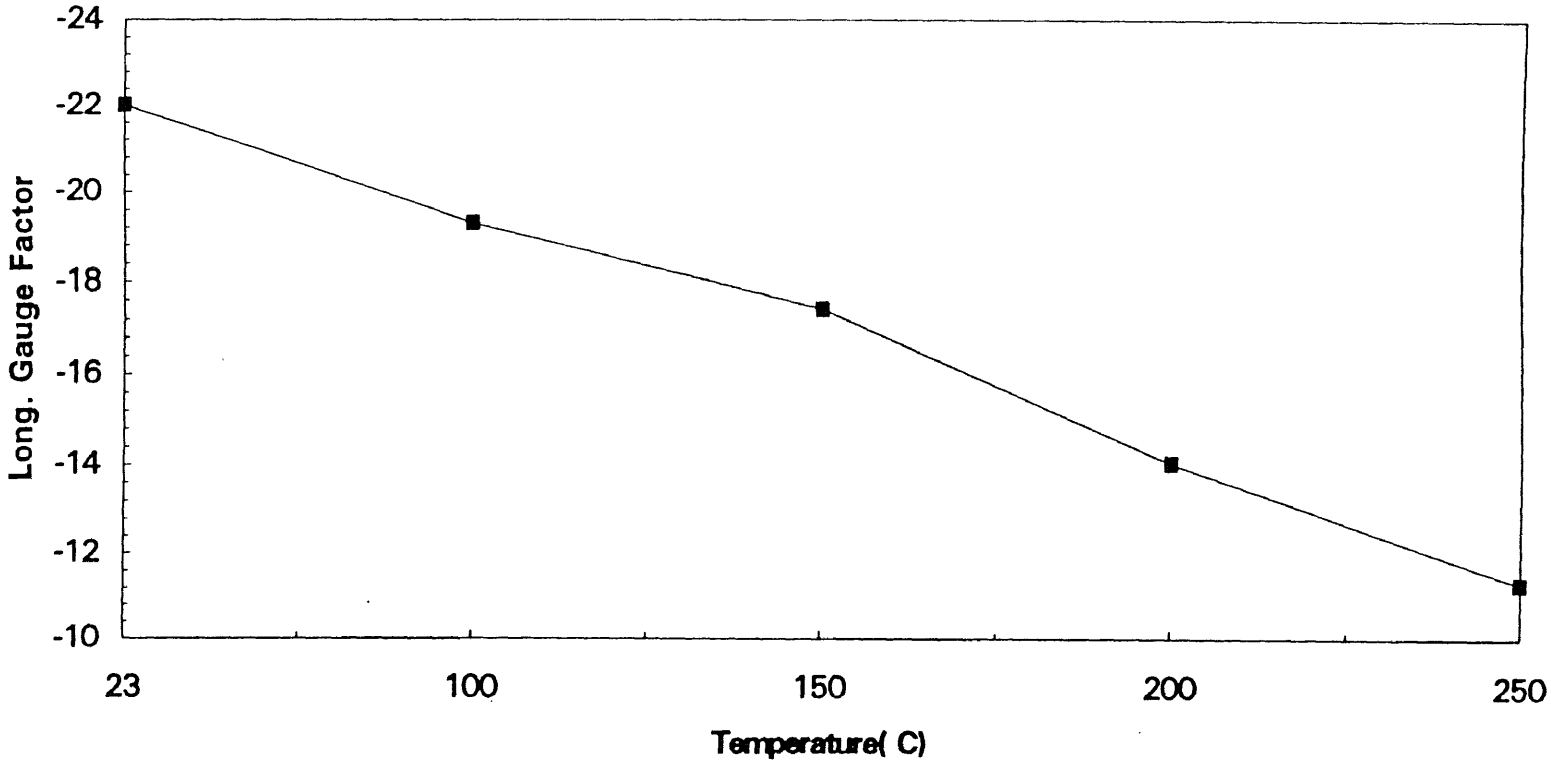

Figure 3-5

Longitudinal gauge factor as a function of temperature. At 250°C the gauge factor is approximately 60% of its room temperature value. (n^+ 6H-SiC, $N_d=2x10^{19}/cm^3$) value.

piezoresistors (N_d = 2 x $10^{19}cm^{-3}$) on a p-SiC substrate. The characteristics of these piezoresistors were established individually in a four-arm wheatstone bridge. The load on the beam was applied through pressure exerted on the metallic diaphragm previously described and transmitted by a boss acting as a push rod to the beam. The bridge output as a function of pressure and temperature is shown in fig. 3-2. It increases linearly with pressure but decreases with increasing temperature. The bridge gage factor, decreases linearly with temperature up to 250°C (see fig. 3-3). Figure 3-4 shows the relative change in resistance of the longitudinal piezoresistors as a function of strain at different temperatures. At all temperatures the linear relationship is observed between $\Delta R/R$ and strain, but the strain sensitivity decreases with increasing temperature. Figure 3-5 presents longitudinal gage factor as a function of temperature. At 250°C the gage factor is approximately 60% of its room temperature. Relative change in resistance vs. strain of the transverse piezoresistors is shown in fig. 3-6. In order to check on the consistency of the measurements, another beam transducer was built and the bridge output as a function of pressure was measured. For comparison, fig. 3-7 presents the results obtained on both beams. In both cases the dependence between the output and the pressure is linear, however one of the beams exhibited a slightly lower sensitivity. This, most probably, was a result of either a geometrical factor (the metal diaphragm in both cases did not have exactly the same dimensions) and/or the mounting procedure. It should be noted, that the random temperature fluctuations made it difficult to measure the gage factor of an individual element, especially the transverse resistors, which exhibit a very small change of resistance with pressure (load).

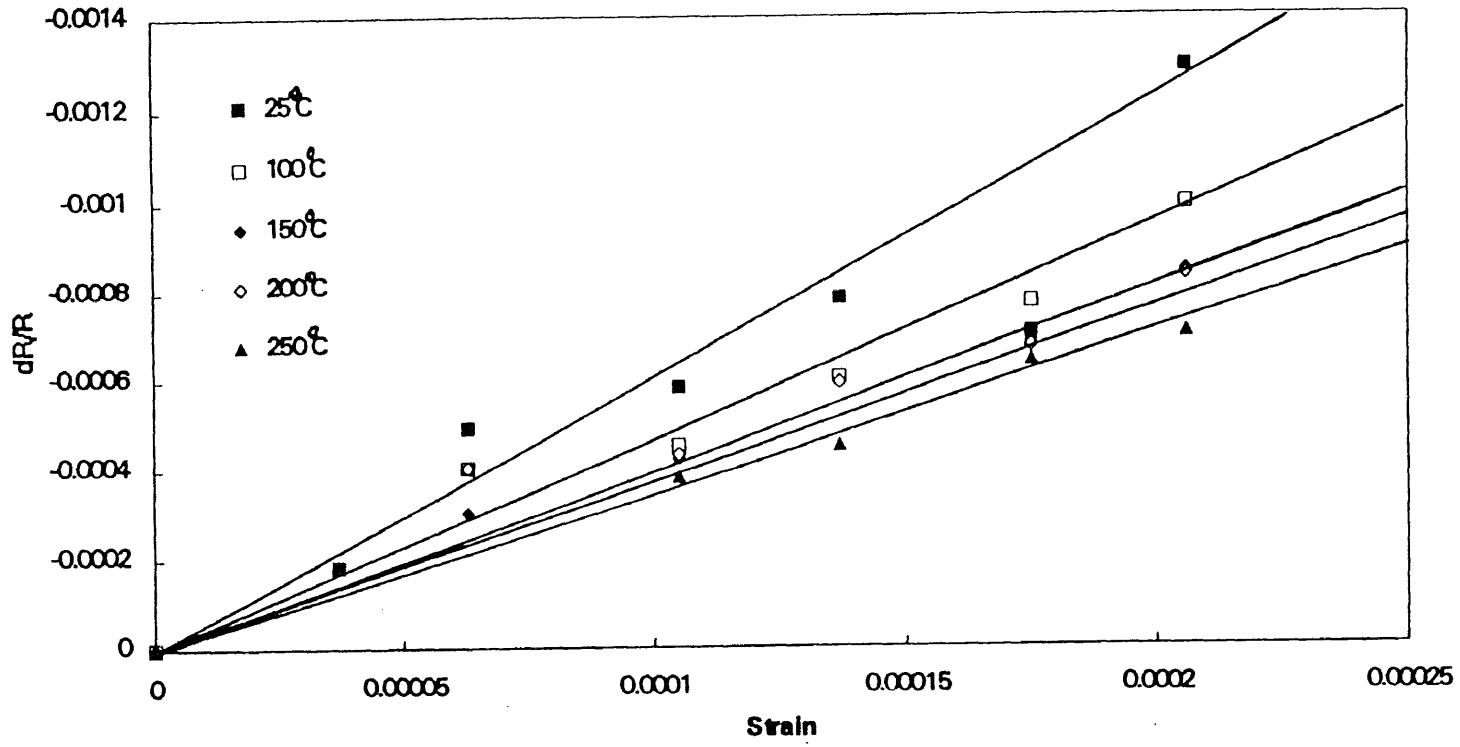

Figure 3-6

Relative change in resistance of the transverse piezoresistors as a function of strain at different temperatures. (n^+ 6H-SiC, $N_d=2x10^{19}/cm^3$)

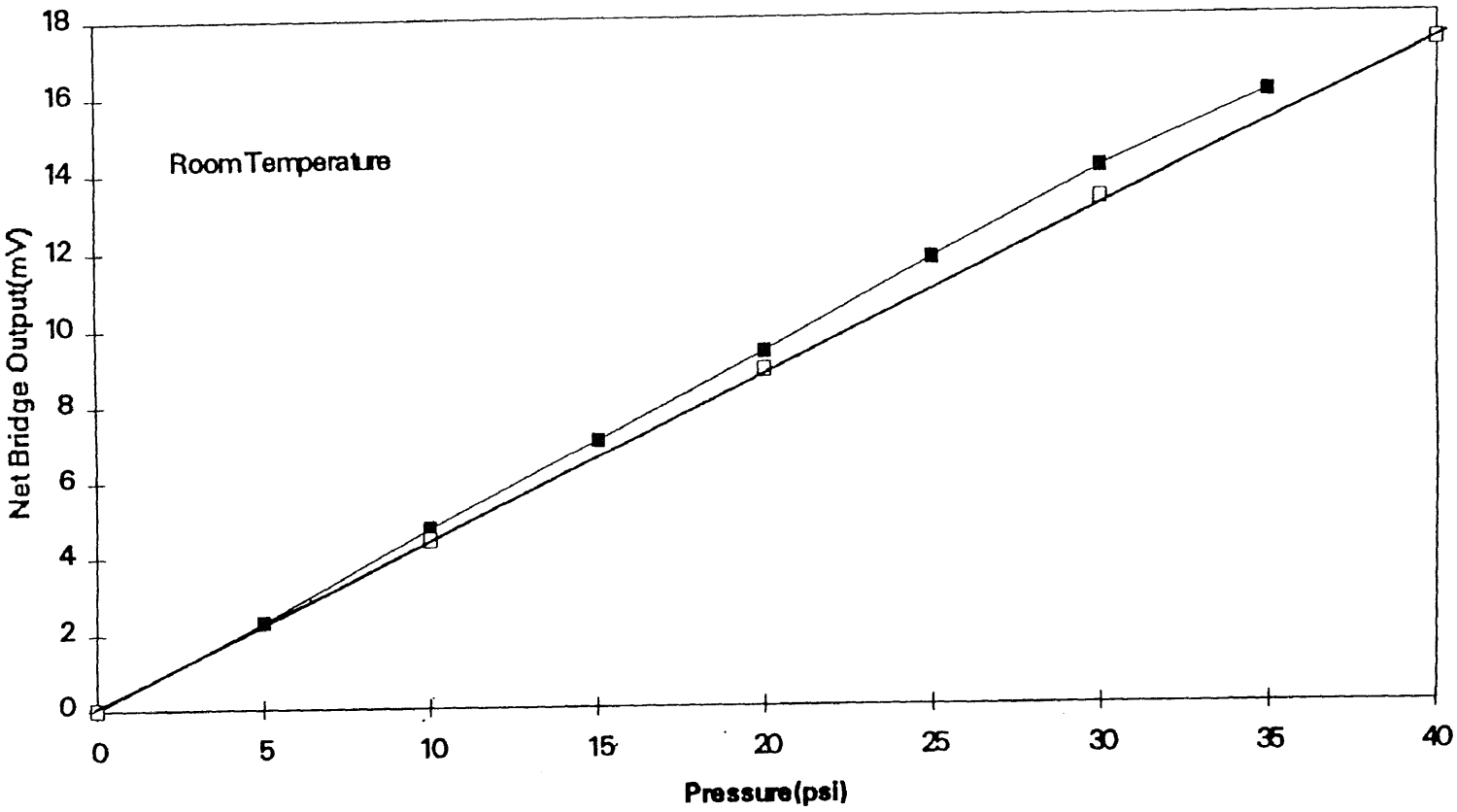

Figure 3-7

Net bridge output as function of pressure of two different beam sensors. In both cases the dependence is linear. (n^+ 6H-SiC, $N_d=2x10^{19}/cm^3$)

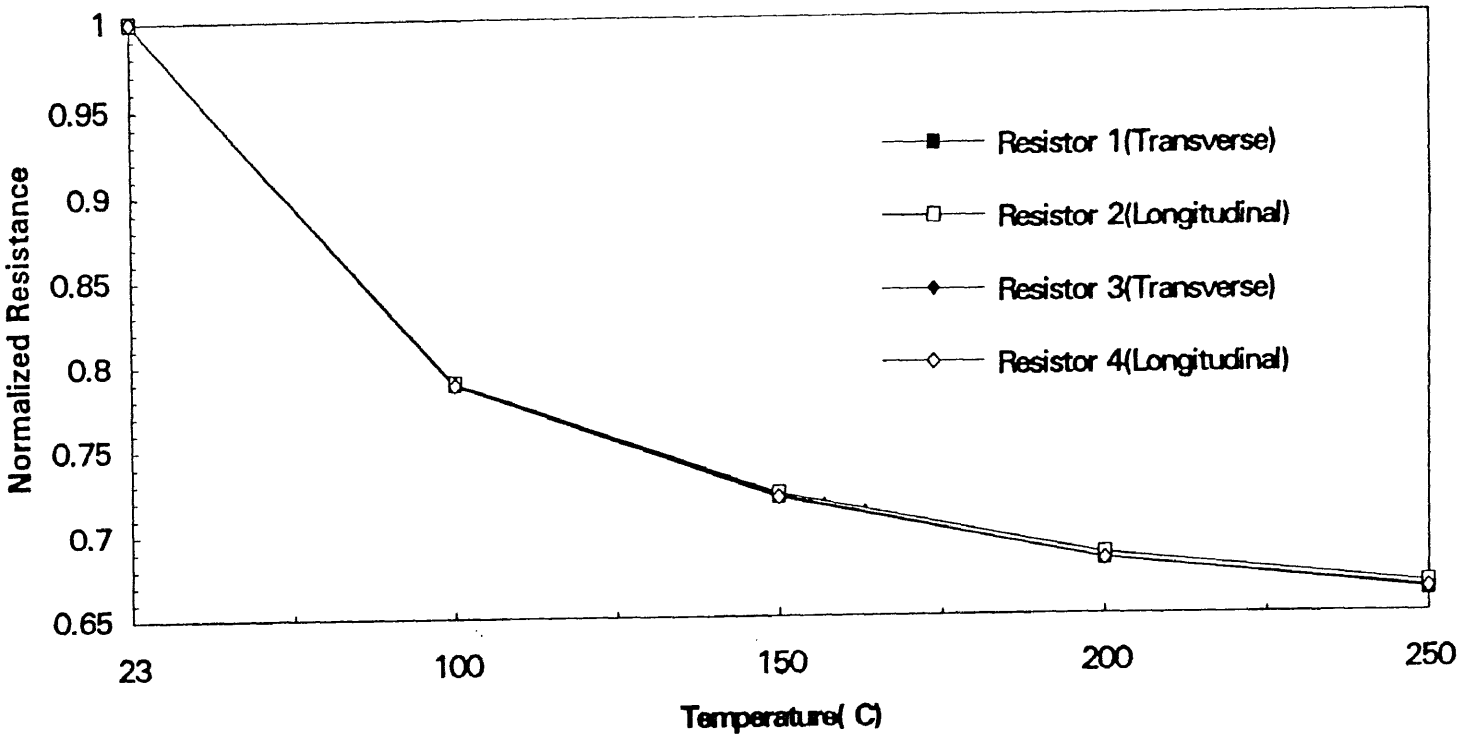

Figure 3-8

Change in normalized resistance of four individual gages in a transducer as function of temperature. All measured resistances decrease as the temperature increases. (n^+ 6H-SiC, $N_d=2x10^{19}/cm^3$).

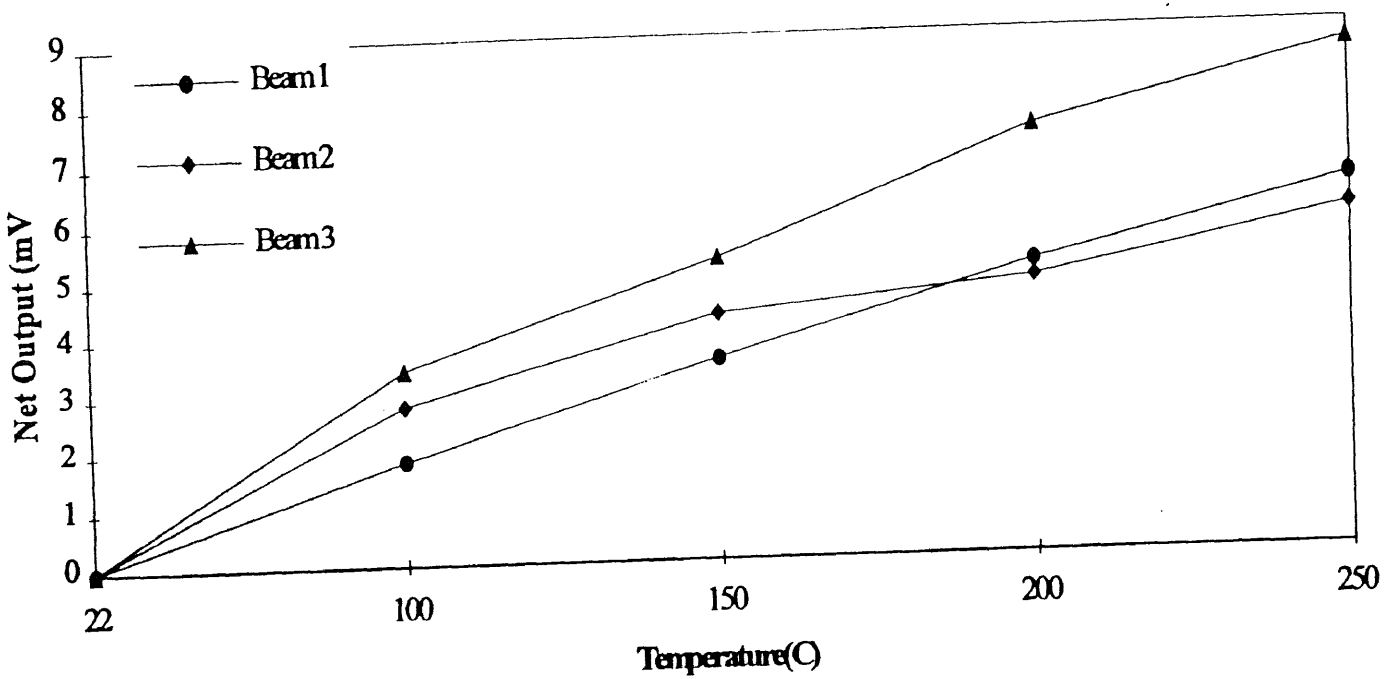

Figure 3-9

Null output of three n' 6H-SiC(N_d=2x10^{19}/cm^3) unmounted piezoresistive beams as function of temperature.

Therefore, the bridge GF data should be considered as the most valid, since the bridge compensates for any changes in temperature.

3.3 Temperature Effect on Resistance

To evaluate the TCR's, resistances of four individual gages ($N_d = 2 \times 10^{19} cm^{-3}$) in a transducer were measured and plotted against temperature (see fig. 3-8). All measured resistance decreased up to 250°C. This indicates that donors in the SiC were not fully ionized at these temperatures. At higher temperatures, after full ionization is achieved, an increase in resistance with temperature should be observed. This means that in spite of the high doping level the resistors were not degenerate. The latter are characterized by Fermi levels in the conduction band and, therefore, the resistance will always increase with an increase in temperature, as a result of the scattering effect. In order to utilize circuit temperature compensation methods, using fixed external resistors, it is necessary for the material to exhibit a positive TCR in the temperature range of the measurements. Such a behavior, at room temperature, is exhibited by 6H-SiC with doping levels $N_d < 1 \times 10^{18}/cm^{-3}$ or $N_a < 5 \times 10^{15} cm^{-3}$. Only these doping levels can be used when utilizing circuit temperature compensation method for room temperature applications of a transducer. The piezoresistors with doping levels used in the present research can be temperature compensated with analytical microprocessor technique. However, resistor circuit temperature compensation methods can be applied for high temperature measurements (>300°C), where the TCR's values are positive.

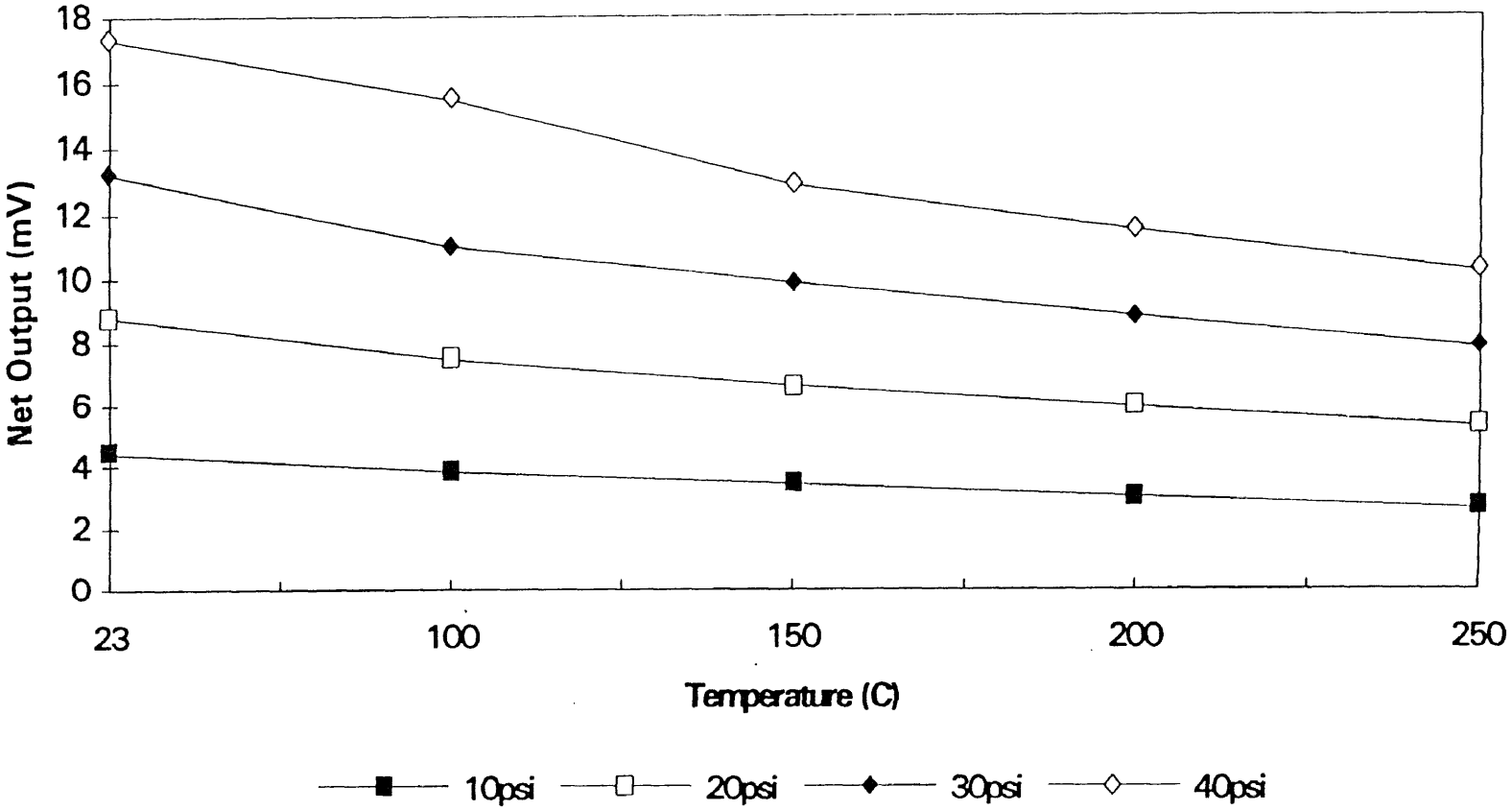

Figure 3-1

Net voltage output vs. temperature of a typical beam at different levels of pressure.

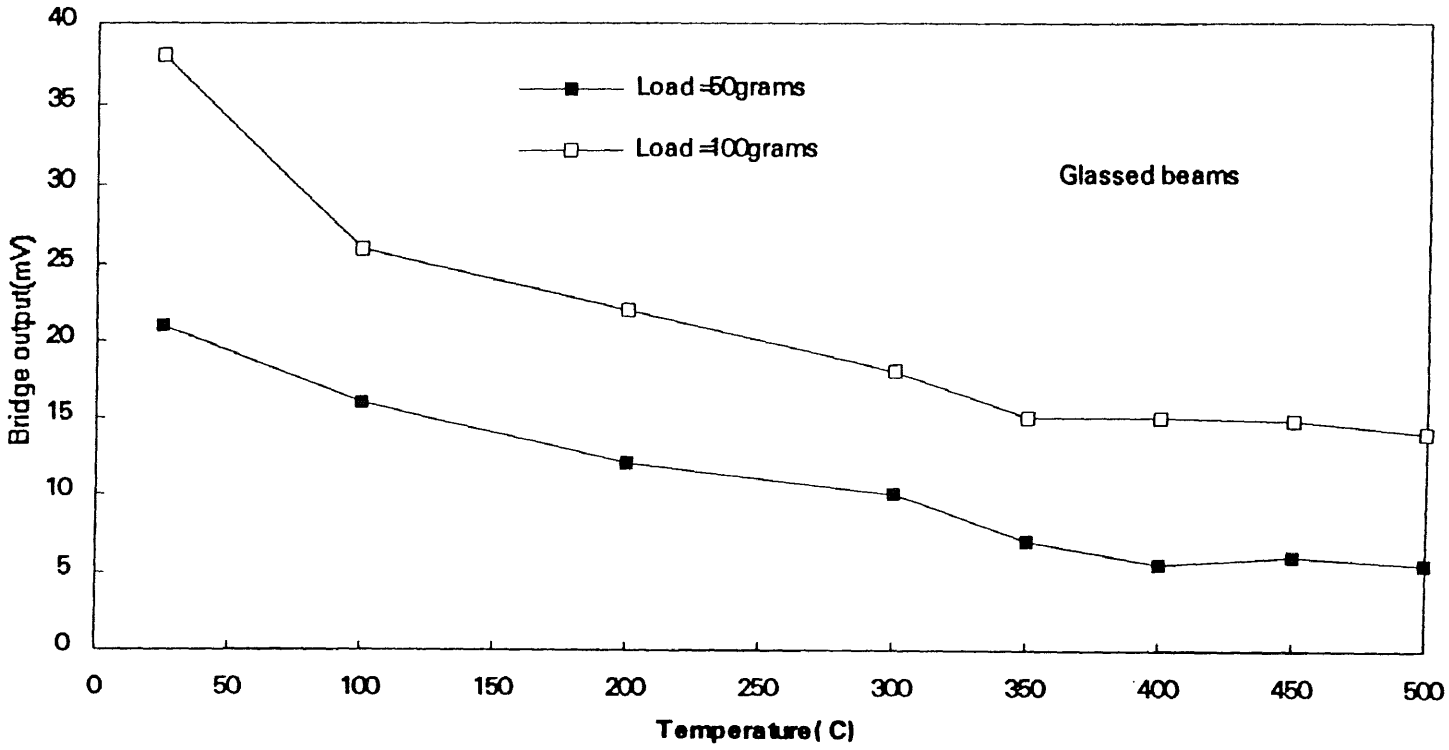

Figure 3-11
Bridge output vs. temperature for two loads applied in bending.

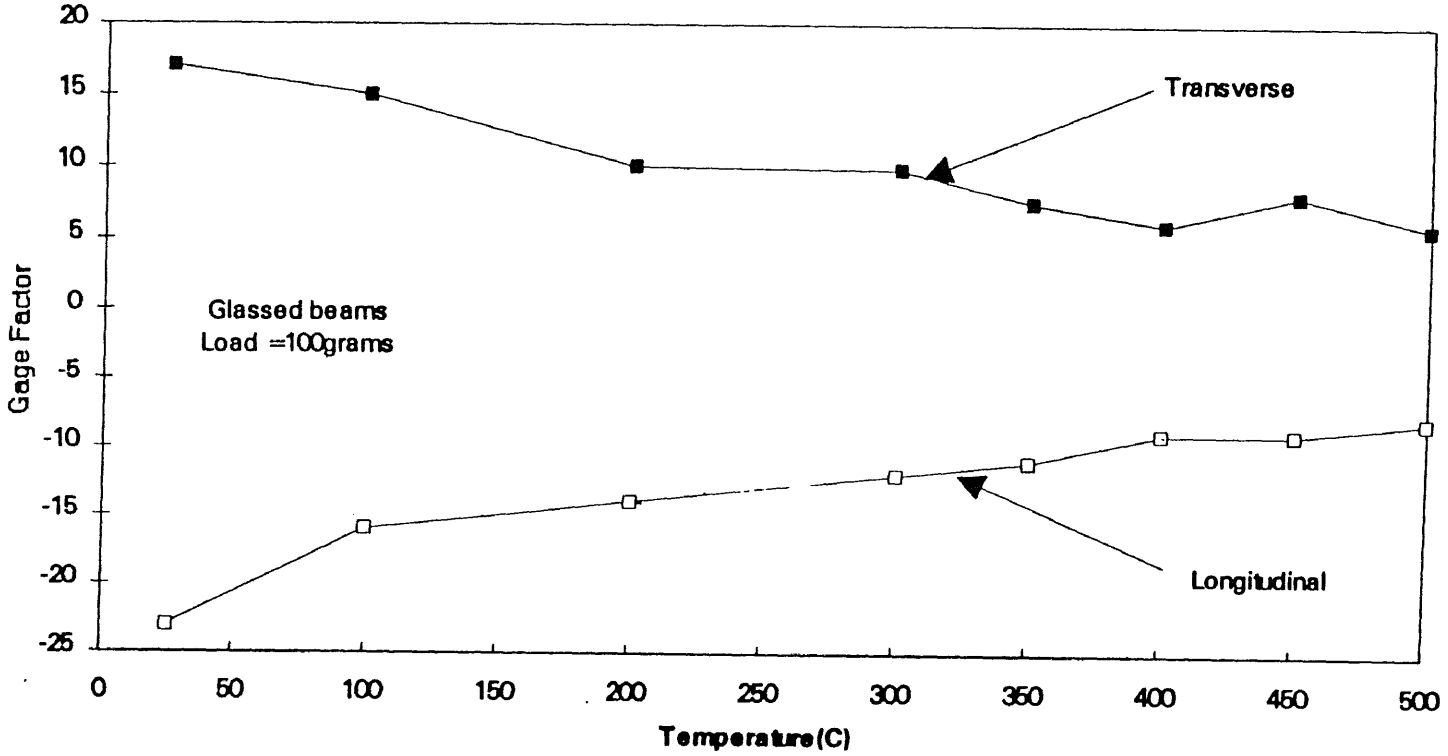

Figure 3-12a

Longitudinal and transverse gage factors as a function of temperature in beam mounted to a metal slab with glass frits, and loaded in bending. Applied load 100grams.

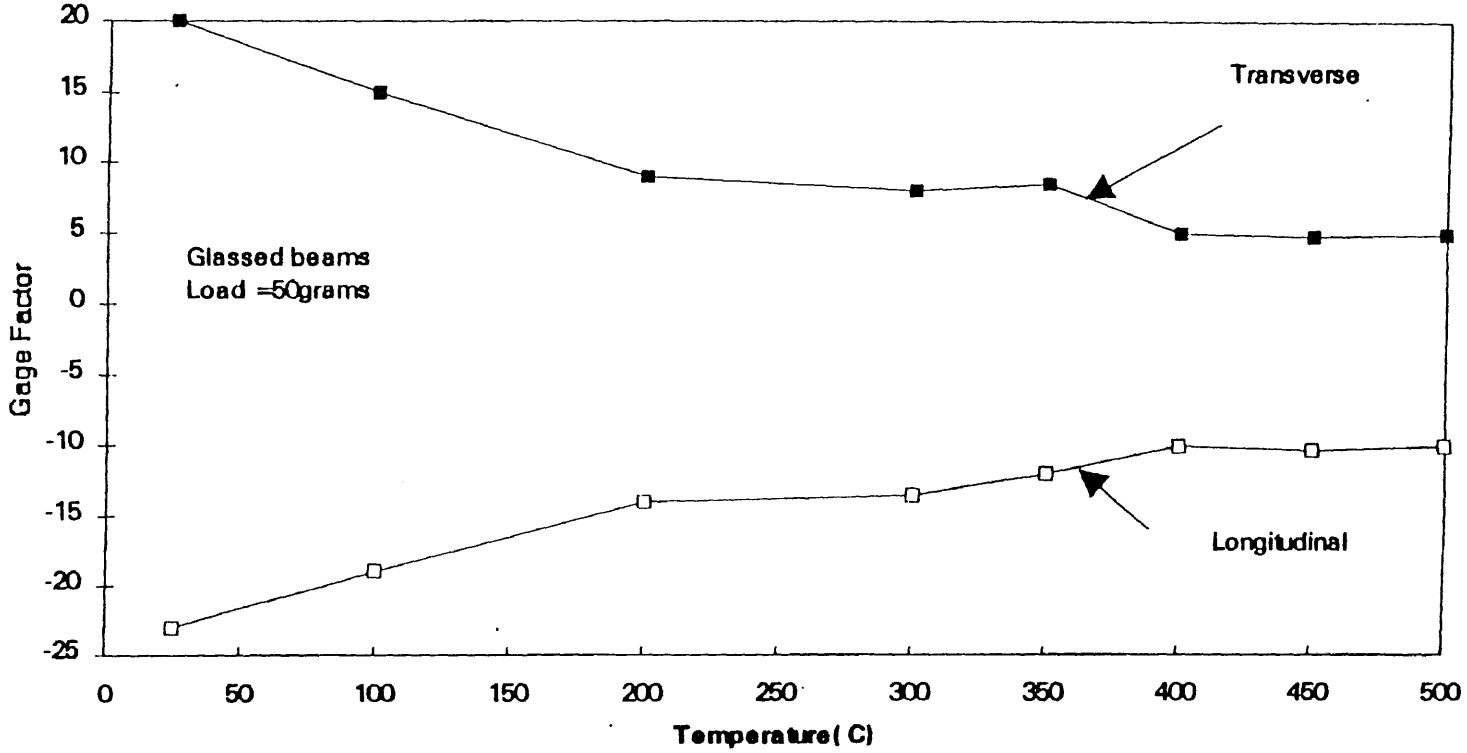

Figure 3-12b

Longitudinal and transverse gage factors as a function of temperature in beam mounted to a metal slab with glass frits, and loaded in bending. Applied load 50grams.

3.4 Temperature Effect on Bridge Output Voltage

One of the important parameters for sensors is the nullshift, (usually expressed as a percentage) which is defined as:

$$Null - Shift = \frac{V_o(T) - Vo(T_{ref})}{FSO} \tag{3-4}$$

where: $V_o(T)$ = null output at any given temperature, T; V_o (T_{ref}) = null output at reference temperature, T_{ref}; FSO = full scale output. The null shift determines a portion of the error signal in the transducer. The null output of three SiC beams were measured before they were mounted in a transducer housing and the results are shown in fig. 3-9 while the output vs. temperature at different levels of pressure, for one of the beams, is shown in fig. 3-10. The null output increases non-linearly with temperature up to 250°C. It was unclear why the SiC beams exhibited such a non-linear increase in null shift. It was possible that the individual resistors in the bridge exhibited different TCR properties, resulting in output shift with increasing temperature. The null shift may be also affected by non-uniformities in the doping level of the SiC wafers. It was also likely, that it was process induced. The problem must be addressed in the future.

In the next stage, piezoresistance measurements up to 500°C were carried out on an integral SiC beam with longitudinal and transverse n-type SiC (N_d = 3 x $10^{18}cm^{-3}$) elements. The beam (wheatstone bridge with 5V input) was mounted to a metal slab with glass frits. A load was applied to the beam by hanging a weight from the edge (bending). The bridge output vs. temperature, for two different stress levels, is shown in fig. 3-11. Initially, up to approximately 400°C, the output decreased and then assumed a constant value, which was roughly one third of the output at room temperature. In fig. 3-12a, b

longitudinal and transverse gage factors as a function of temperature are shown for the same stress levels, applied previously. The longitudinal GF's were negative, while the transverse GF's were positive. Since both gage factors had not been corrected for parasitic resistances, it could be assumed that their real values were higher. The negative longitudinal gage factors increased gradually up to 400°C and at that temperature assumed a constant value of approximately -11. The positive transverse gage factors decreased gradually up to 400°C and then assumed a constant value of approximately +9. It was expected that both gage factors would remain constant up to 700°C. Similar behavior was observed in other semiconductors such as Si and 3C-SiC, however, at different ranges of temperatures.

The following step in the project was associated with fabrication of beams from the p-type SiC (N_a = 2 x $10^{19}cm^{-3}$), which were tested at room temperature. The normalized output voltage for the compressive and tensile beams as a function of applied pressure is shown in fig. 3-13 a, b. Although, the measurements lacked high accuracy due to problems associated the quality of the sample, nevertheless, they allowed to estimate the gage factor of the longitudinal resistors to be -27. From this preliminary data it appeared that p-type SiC does not have a higher gage factor than comparable n-type SiC. However, because of the high activation energy of the acceptor (Al) in p-type SiC it seemed that the TCR's of this material will be negative up to much higher temperature

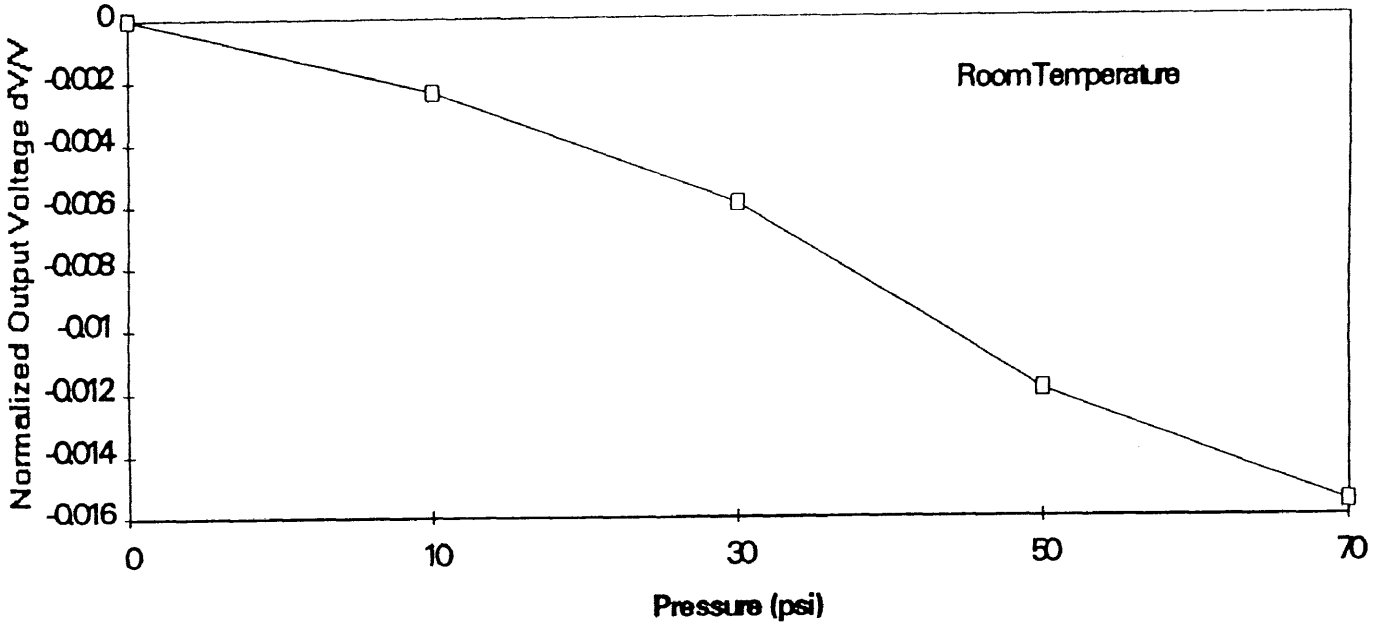

Figure 3-13a
Normalized Output Voltage as a function of applied pressure of p-type 6H-SiC beam under compressive stress.

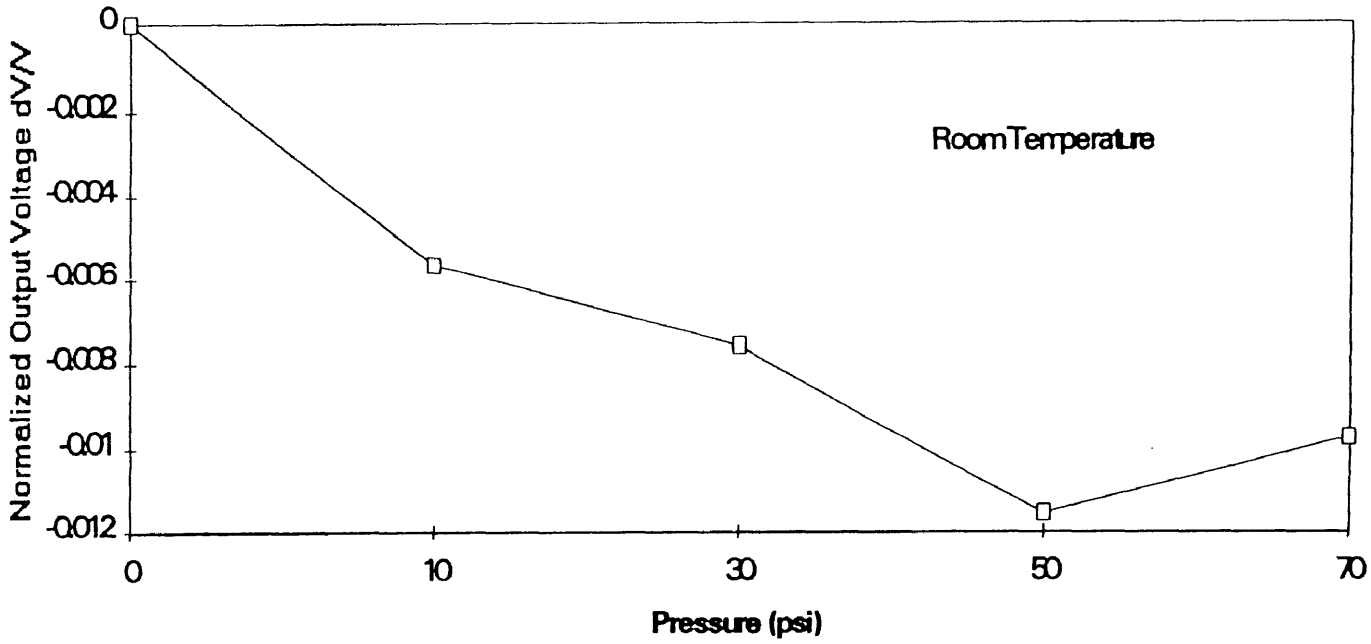

Figure 3-13b

Normalized Output Voltage as a function of applied pressure of p-type 6H-SiC beam under tensile stress.

(~700°C). This will make compensation of p-type piezoresistors difficult. They can be, still, fabricated off the diaphragm area and be placed in series with the bridge to function as thermistors to provide higher voltage to the bridge at high temperatures. This might compensate for the drop in the gage factor of the n-type sensing element.

CHAPTER 4

HIGH TEMPERATURE METALLIZATION

4.1 Overview

In order to build any high temperature electronic device it is essential to fabricate ohmic contacts which are capable of withstanding the device operation temperatures. At high temperatures the metallized contacts can undergo degradation as a result of enhanced microstructural processes, which occur at high temperature. These include inter-diffusion between different layers, oxidation, compositional and microstructural changes which may result in instability at the metal/semiconductor interface. Any of these processes may lead to contact failure and, therefore, they must be analyzed and studied when considering the development of metallization for high temperature application.

4.2 Selection of High Temperature Metallization Scheme

In the first stage of the research program it was necessary to identify a few metals and alloys which form ohmic contact on 6H-SiC. The first metals chosen were titanium, nickel-titanium and titanium-tungsten. It had been shown previously[20] that titanium contact deposited on 3C-SiC withstood 20 hours at 650°C. Nickel is known to be a good ohmic contact on SiC but exhibits severe adhesion problems[21]. Nickel-Titanium alloys may combine the favorable electrical properties of nickel with high reactivity and adhesion of titanium. Titanium-Tungsten exhibit good diffusion barrier properties and may also be ohmic. Several research groups have demonstrated the effectiveness of TiN as a diffusion barrier[22,23]. On the basis of these experimental results titanium nitride was initially

chosen as the diffusion barrier for the scheme. A process to sputter titanium nitride was developed. The compound was reactively sputtered from a titanium target in a mixture of nitrogen (20%) and argon ambient.

4.3 General Experimental Procedure

Several (0001), S-face 6H-SiC substrates having n-type 1μm thick epilayer of different doping levels were supplied by Cree Research. The wafers were initially cleaned by modified RCA method and dipped in 49%HF for five seconds, after which they were rinsed and blow dried. They were then oxidized in dry oxygen ambient at 1150°C for sixteen hours to yield oxide thickness of about 1100Å. Negative photoresist was spun on the oxide at 5krpm for thirty seconds. Photolithography was used to define circular patterns on the wafers. Circular contact holes were then etched through the oxide with buffered HF(BHF) to expose the epilayer surface. The contact holes consisted of twelve rows. Each row was made up of four circular contact holes of the same diameter, *d*, with 225μm equidistant separation between them as shown in fig. 4-1. The diameter of the contacts ranged from 6μm to 28μm. The samples were RCA cleaned again, but with no HF dip. This process assured a very clean epilayer surface. It was followed by a dehydration process in nitrogen ambient at 200°C for twenty minutes to remove any water trapped within the micropipes in the wafers. The samples were immediately transferred into the sputtering chamber for metal depositions.

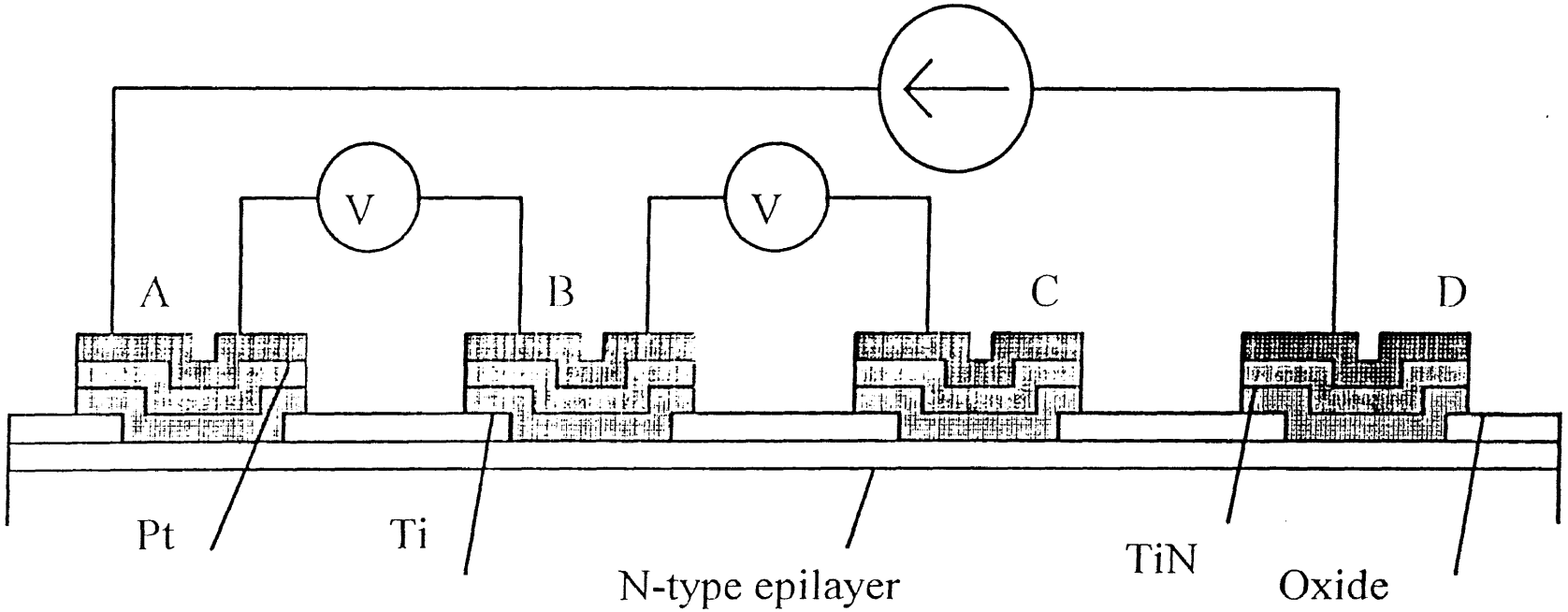

Figure 4-1
Cross-sectional view of multilayer metallization contact on n-type 6H-SiC epilayer for contact resistivity measurements.

4.4 General Electrical Characterization

The I-V characteristic measurements of epilayer contacts were conducted by probing two adjacent contacts from the same row. The contact resistivity was measured using the four-point method. Current I_{AD} was passed through the circular contact as shown in fig. 4-1 overlapped by Schockley pad A and out through pad D. The series resistance of the epilayer, denoted R_m, was measured between contacts B and C by measuring the voltage V_{BC} between the pads and divided by the applied current. The spreading and contact resistance, denoted R_s and R_c, respectively, can be expressed as

$$R_S + R_C = \frac{V_{AB} - V_{BC}}{I_{AD}} \tag{4-1}$$

The resistance of the probes was considered negligible. The four-point probe method used was based on that that established by *Kuphal et al*[24], in which the specific contact resistivity was explicitly obtained. In these experiments, however, since the main issue of interest was the overall change in resistance under the contact, R_c and R_s were lumped together in determining the contact resistivity. Thus, Kuphal's contact resistivity equation was modified and expressed as

$$r_{cs} = \frac{A}{I_{AD}}\left[V_{AB} - V_{BC}\cdot\frac{\ln\left(\left(3\frac{s}{d}\right)-\left(\frac{1}{2}\right)\right)}{2\ln 2}\right] [\Omega\text{-cm}^2] \tag{4-2}$$

where, A = contact area(μm); s = distance between adjacent contacts(μm), and d = diameter of the contact(μm). Unless where specified, the applied current was 1mA. As a result of lumping the spreading and contact resistances, the result obtained could be considered to be on the high end.

4.5 Characterization of Ti/TiN/Pt Scheme

Titanium was deposited on highly doped ($10^{19}cm^{-3}$) n - and p -type 6H-SiC epilayers in order to fabricate an ohmic contact. To prevent oxidation, titanium was overcoated with platinum. In the as-deposited state the titanium contact on p-type SiC was found to be rectifying, while on n-type it was ohmic for this doping level. Measurements were made with four probes coming in contact with the Shockley pads that extend over the oxide. The contact resistance, using equation(4-2), was found to be approximately 1×10^{-5} cm^{-2}.

It was established that in order to obtain an ohmic contact on n-type 6H-SiC with lower doping levels (5×10^{17} - $10^{18}cm^{-3}$) a high temperature annealing was required. The process that was designed consisted of three stages a) deposition of a patterned titanium layer on the n-SiC substrate; b) annealing at 1000 C for 30 seconds to make the contact ohmic, and c) deposition and patterning of the multilayered film on the annealed titanium layer.

In order for the process to be feasible, it should not result in significant oxidation of titanium. The feasibility was checked on a Silicon control wafer. The Auger depth profile taken from the Silicon wafer which underwent the process, revealed presence of silicon in the titanium layer, as well as presence of a thin(150Å) layer of oxygen on the surface. The oxidized layer could be removed by sputter etching.

As the next step in the development of high temperature metallization a multilayer consisting of Ti/TiN/Pt was deposited. Titanium(1000Å) film was first deposited by sputtering, patterned with EDTA and then annealed to obtain an ohmic contact.

Subsequently, the sample was placed back into the chamber and layers of titanium nitride(500Å) and platinum (3500Å) were deposited. The contacts were tested at 650°C in air. Most of the contacts failed after 5 hours by peeling off the substrate. Auger depth profiles revealed the presence of 20 at % oxygen in the titanium and titanium nitride films. The trapping of oxygen within the TiN layer was also reported by Ting *et al*[25].

A few possible reasons could be responsible for the poor adhesion. Some of them were associated with the sputter system e.g. high oxygen content. Others, such as breaking of vacuum during the sputtering or insufficient thickness of the titanium nitride layer were associated with the fabrication process. All the above reasons were analyzed and proper steps were undertaken to improve the performance of the chosen deposition regime.

4.5.1 Modified Ti/TiN/Pt Deposition Process

After introducing changes and improvements in the sputter system and in the fabrication process a multilayer of Ti(1000Å)/TiN(1000Å)/Pt(1000Å) was deposited on 6H-SiC sample with patterned oxide. The 6H-SiC had a top n-type epilayer (N_d = 1.4 x $10^{18}cm^{-3}$). Photolitography was used to define the platinum pads. The platinum was etched in light aqua regia at 80°C for one minute to expose the underlying titanium nitride. Using platinum as self-aligned mask, the Ti/TiN were selectively etched in 1:1 EDTA: H_2O at 80°C for 30 seconds to expose the field oxide. This step isolated the contacts from one another (see fig. 4-1).

The process of sequential deposition, without breaking vacuum, reduced chances of any interfacial contamination and especially offered protection of the titanium surface from oxidation and practically eliminated adhesion and stability problems. On the 6H-SiC of this doping level as-deposited titanium contact was rectifying as shown in fig. 4-2a, and an ohmic contact was formed only after rapid thermal annealing for thirty seconds at 1000°C in argon, seen fig. 4-2b. The contact resistivity was measured at 650°C as a function of time by using the four point probe method earlier described. The results are presented in fig. 4-3. Some observed discrepancies in the contact resistivity were attributed either to the residues of oxide within the contact, which reduced the effective contact area, or to undercutting of the contact oxide. The titanium layer formed a strong bond with the oxide providing good adhesion. No peeling or buckling of the layers was observed. The shrinking of the top Platinum layer had abated after two hours.

Based on the obtained results, it was concluded that the established deposition regime and the subsequent rapid thermal annealing of the Ti/TiN/Pt makes that metallization scheme a good candidate for prolonged (hours) use in a high temperature (~650°C) environment. Contact resistivity measurements were intermittently made up to forty nine hours. The increase of dwelling time did not result in changes in the contact resistance and the shift remained negligible. Auger spectrum, taken from the surface of the sample after 40 hours at 650°C revealed the presence of silicon, titanium and carbon in addition to platinum shown in fig. 4-4. Auger spectrum previously taken from the same surface in the as-deposited state did not reveal the presence of silicon and titanium. Appearance of silicon and titanium at the surface indicates

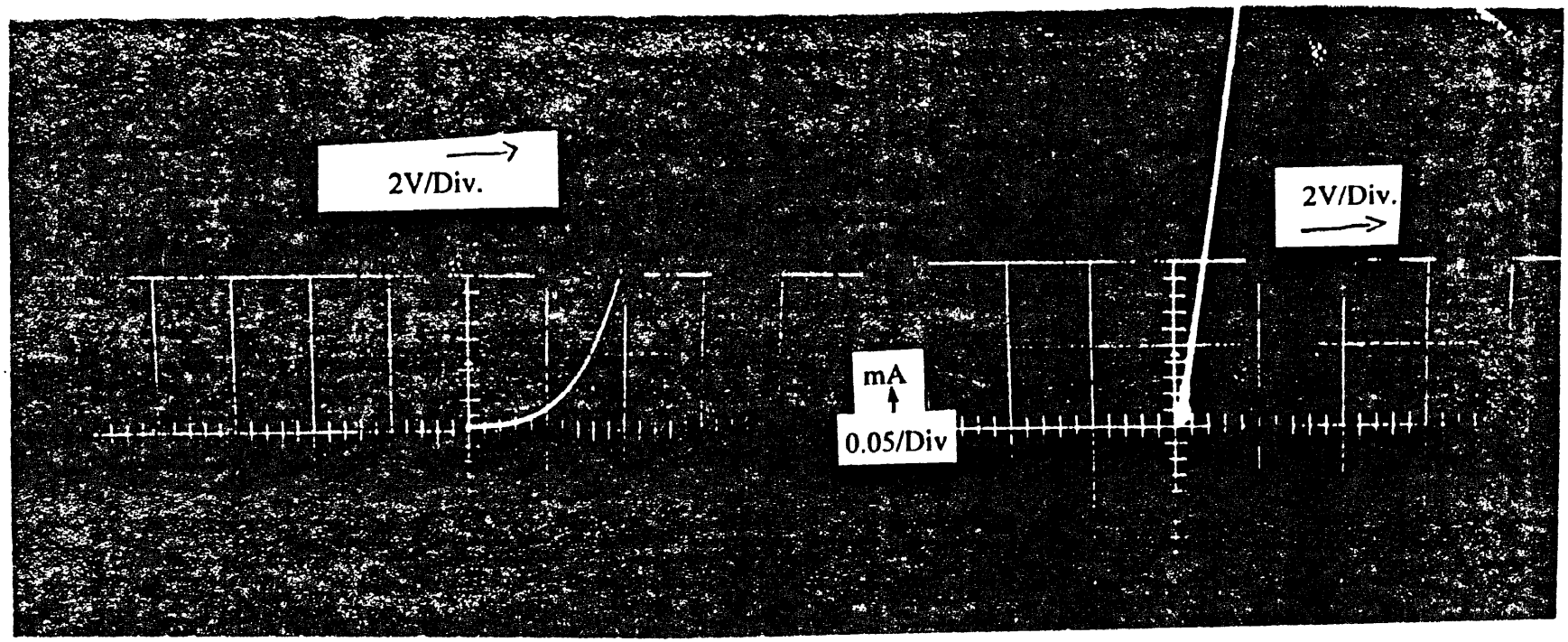

(a) (b)

Figure 4-2

a) Rectifying contact, sample in the as deposited state. Metallization scheme n-type 6H-SiC/Ti/TiN/Pt. b) Ohmic contact, sample after rapid thermal annealing at 1000°C for 30 seconds in Argon. Metallization scheme n-type 6H-SiC/Ti/TiN/Pt.

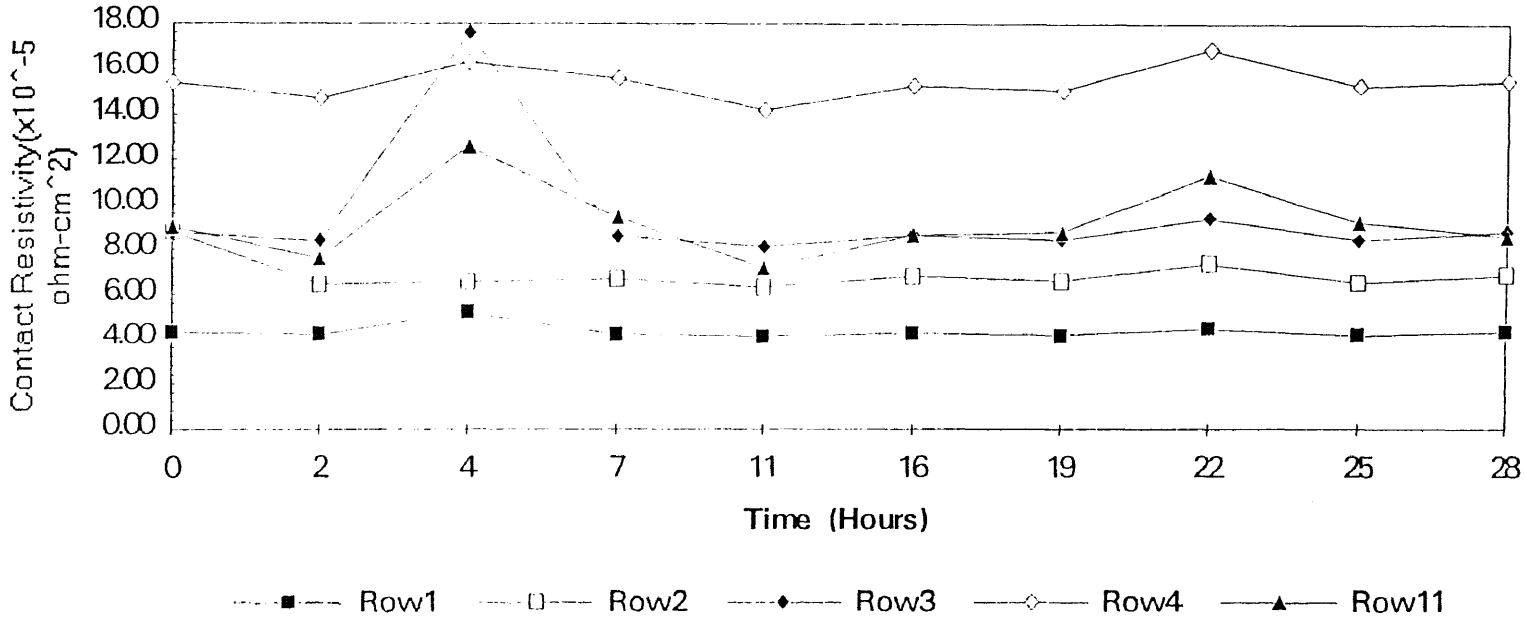

Figure 4-3

Contact resistivity vs time at 650°C in air of n-type 6H-SiC/Ti/TiN/Pt high temperature metallization scheme. Time limit twenty-eight hours.

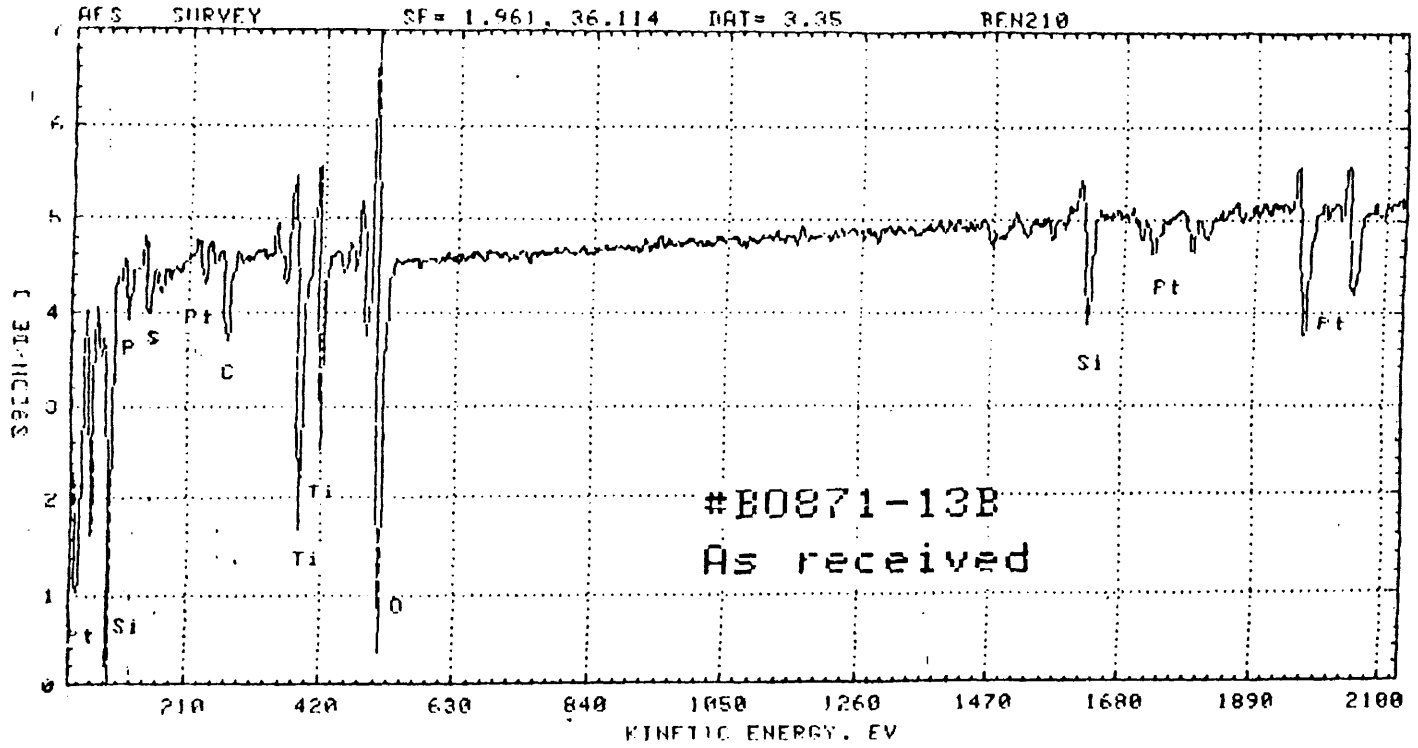

Figure 4-4

Auger spectrum, taken from the surface of the sample after 40 hours at 650°C. Presence of Pt, Si, Ti and C can be seen.

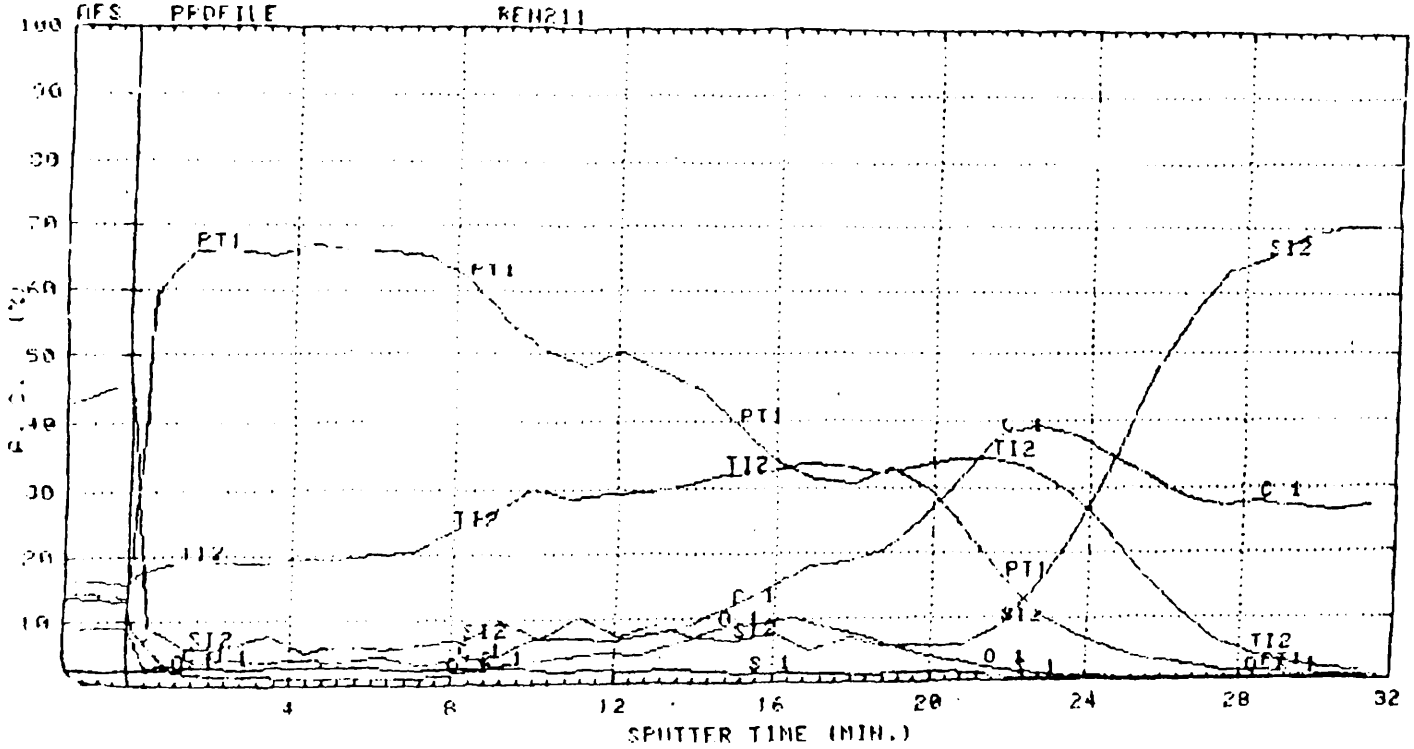

Figure 4-5

Auger depth profiles taken from the sample after 40 hours at 650°C. Presence of two reaction zones: at the 6H-SiC/Ti region and at the Ti/TiN area can be seen.

outward diffusion of these elements. The Auger depth profile carried out on the sample treated at 650°C for forty hours revealed presence of two reaction zones (see fig. 4-5). One, is the region of 6H-SiC/Ti, and the second is the TiN/Pt zone. The first is characterized by the presence of titanium and carbon, as well as small quantities of silicon (~10 at %) and platinum (~15 at %). Since carbon and titanium depth profiles follow each other it could be assumed that titanium carbide was formed. The presence of platinum in this zone indicates that the titanium nitride diffusion barrier did not prevent the inward diffusion of platinum. In the second reaction zone, the presence of silicon, carbon, titanium and platinum was observed, indicating that the barrier did not prevent outward diffusion of carbon, silicon and titanium. The presence of titanium (~19at %) was observed in the platinum outer layer. However, the interesting point is, that the above compositional variations did not result in visible changes in the electrical characteristics at the time frame investigated.

4.6 Resolution of Ti/TiN Peaks

One of the problems which exists in auger spectroscopy is the peak overlapping of different elements. This is the case in the titanium nitride compound, where the peak of nitrogen is situated very close to that of the titanium and practically can not be resolved. In this case another peak of titanium is chosen and the titanium line reflects the distribution of titanium only, while nitrogen profile usually contains signals of titanium too. That is the reason why the nitrogen profile is not shown in fig. 4-5.

Further extension of the dwelling time to 65 hours at 650°C did not result in significant changes in the contact resistivity (see fig. 4-6), and only after 65 hours a rectification effect was observed.

4.6.1 Significance of Results

The significance of this experiment is the fact that the chosen deposition regime Ti/TiN/Pt maintained an almost constant contact resistivity at 650°C during the exposure for approximately 60 hours. It should, however, be stressed that the chosen deposition scheme is exceptionally sensitive to oxygen contamination during the deposition and/or oxygen penetration during subsequent treatments. In order for this multilayer high temperature metallization to be applicable, the oxygen contamination must be kept at less than 3 at % oxygen. This was evident from a few experiments carried out in the later stages of research. High levels of oxygen contamination at the interfaces Pt/TiN or/and TiN/Ti could (at high temperature) result in full or partial disintegration of the titanium nitride layer and in replacement of this layer by a layer of titanium oxide due to the high affinity of titanium toward oxygen. Formation of titanium oxide results in two deleterious effects: a) It entirely reduces the effectiveness of the diffusion barrier and, b) Formation of dielectric layer which leads to rectification and failure of the ohmic contact. Another destructive effect is penetration of oxygen through the outer platinum layer. There are indications that the deposited platinum layer may contain high density of pinholes. At high temperature the oxygen penetrates through the pinholes inside the multilayer metallization and thereby destroys the titanium nitride diffusion barrier. It also reacts with the titanium

beneath the barrier, forming a solid titanium oxide layer with its rectifying properties, which extends to the 6H-SiC surface. For the metallization scheme to work effectively in air, the issue of oxygen contamination must be resolved. There was need, therefore, to investigate other schemes that would be applicable in air.

4.7 Alternative Ti/$TaSi_2$/Pt Scheme

Oxygen contamination, in general, poses a big problem for the above suggested metallization scheme, but the risk is minimal if the newly developed sensor for high temperature application will operate in vacuum or nitrogen ambient. The following experiment was conducted to prove the thermal stability of the discussed deposition scheme in nitrogen. A sample underwent rapid thermal annealing, to obtain ohmic contact, and subsequently was heat treated at 650°C in pure nitrogen. No signs of any deterioration were observed in the tested metallization scheme after 10 hours. In air a similar sample failed in less than two hours.

In view of the sensitivity of the Ti/TiN/Pt scheme to oxygen, it became imperative that an alternative high temperature metallization system, for use in an oxidizing ambient, had to be developed. A modified metallization scheme was introduced namely: Ti/$TaSi_2$/Pt. The choice of $TaSi_2$ as a diffusion barrier was due to its confirmed thermodynamic stability at 600°C[26]. Murarka *et al*[27] concluded that the silicide does not oxidize rapidly in dry oxygen. As a result of its stability at 600°C, reaction with the underlying titanium or titanium derivatives is minimized. Therefore, critical zonal reaction confinement of titanium derivatives to avoid species outdiffusion is achieved.

4.7.1 Deposition of Ti/$TaSi_2$/Pt Metallization

The applied deposition procedure carried out at NJIT[28] was as follows: Ti(1000Å) was initially sputtered on SiC n-epilayer through vias etched in oxide. This was followed by sputter deposition of $TaSi_2$ (2500Å) and Pt (3500Å). All depositions were done without breaking vacuum. Schockley pads arranged in four probe configuration were defined on the top of the Pt layer. The Pt layer was etched in aqua regia at 90°C for 4 minutes. The Ti/$TaSi_2$ layers were etched in buffered hydrofluoric acid (BHF) for fifteen minutes to complete the patterning of the probe pads. The samples were subsequently stripped of photoresist and cleaned.

4.7.2 Electrical Characterization of Ti/$TaSi_2$/Pt on (6H)-SiC

The I-V measurements showed a rectifying contact as shown in fig. 4-7a. The sample was then annealed for 30 minutes at 600°C in N_2 ambient. The following I-V measurements confirmed ohmic contact shown in fig. 4-7b. To prove the thermal stability of the deposition scheme in an oxidizing ambient, contact resistivity measurements were conducted at room temperature and as a function of time at 600°C. The four probes method used was described previously. The contact resistivity values obtained in all the experiments were in the 10^{-4} Ω-cm^2 range and remained stable beyond 20 hours at 600°C in air as shown in fig. 4-8.

In order to obtain information on the chemical changes, which take place in the metallization during the dwell time at 600°C, Auger electron spectroscopy (AES) analysis

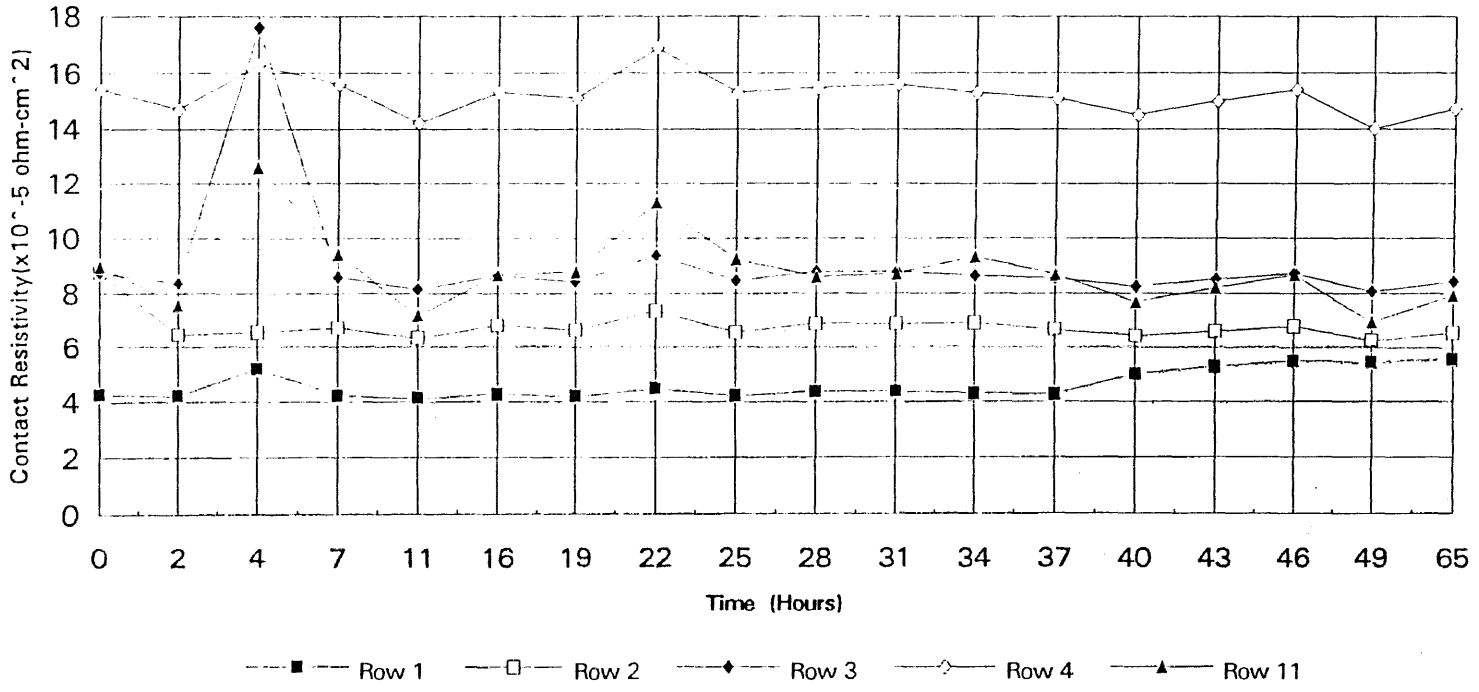

Figure 4-6
Contact resistivity vs. time at 650°C in air of n-type 6H-SiC/Ti/TiN/Pt high temperature metallization scheme. Time limit 65 hours.

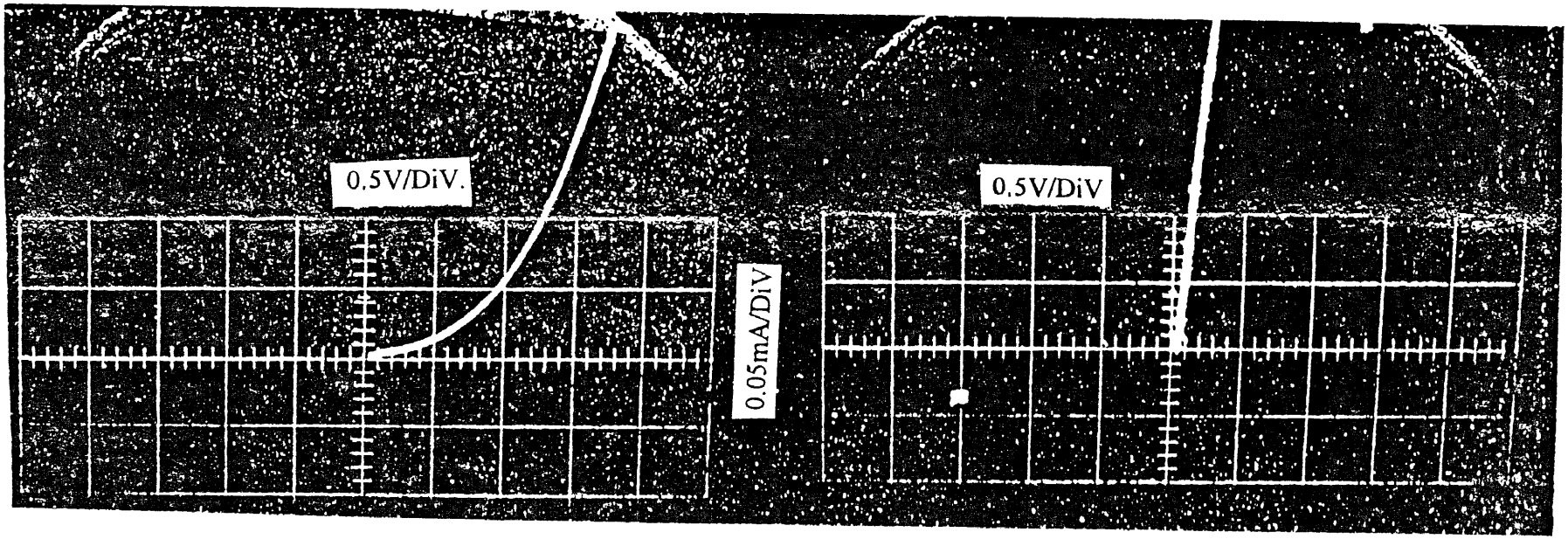

(a) (b)

Figure 4-7

a) Rectifying contact of 6H-SiC/Ti/$TaSi_2$/Pt sample in the as deposited state. b) Ohmic contact, sample after rapid thermal annealing at 600°C for 30 minutes in nitrogen.

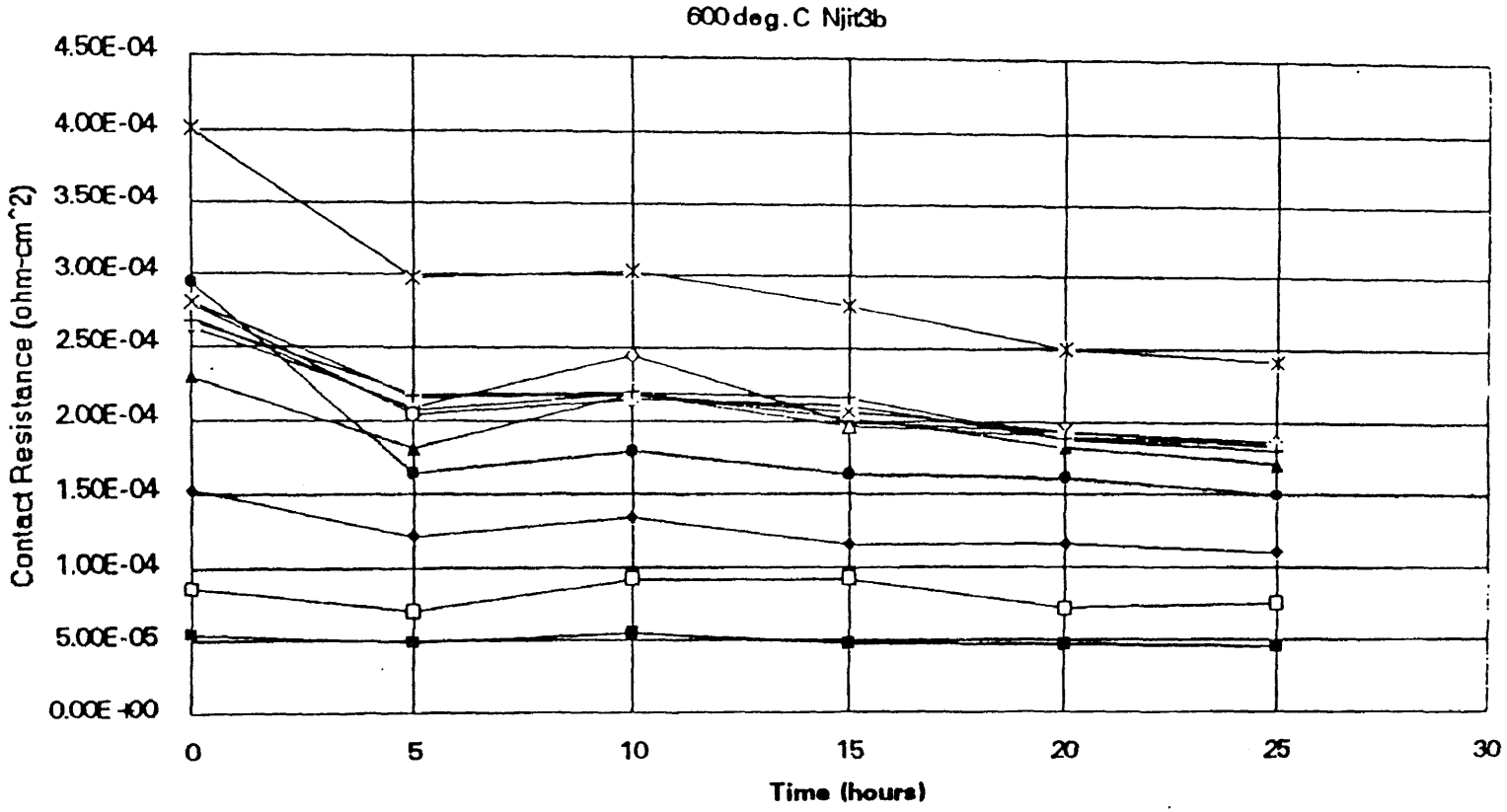

Figure 4-8

Contact resistivity of Ti/$TaSi_2$/Pt metallization scheme on n-epilayer of 6H-SiC after intermittent heat treatment at 600°C in air.

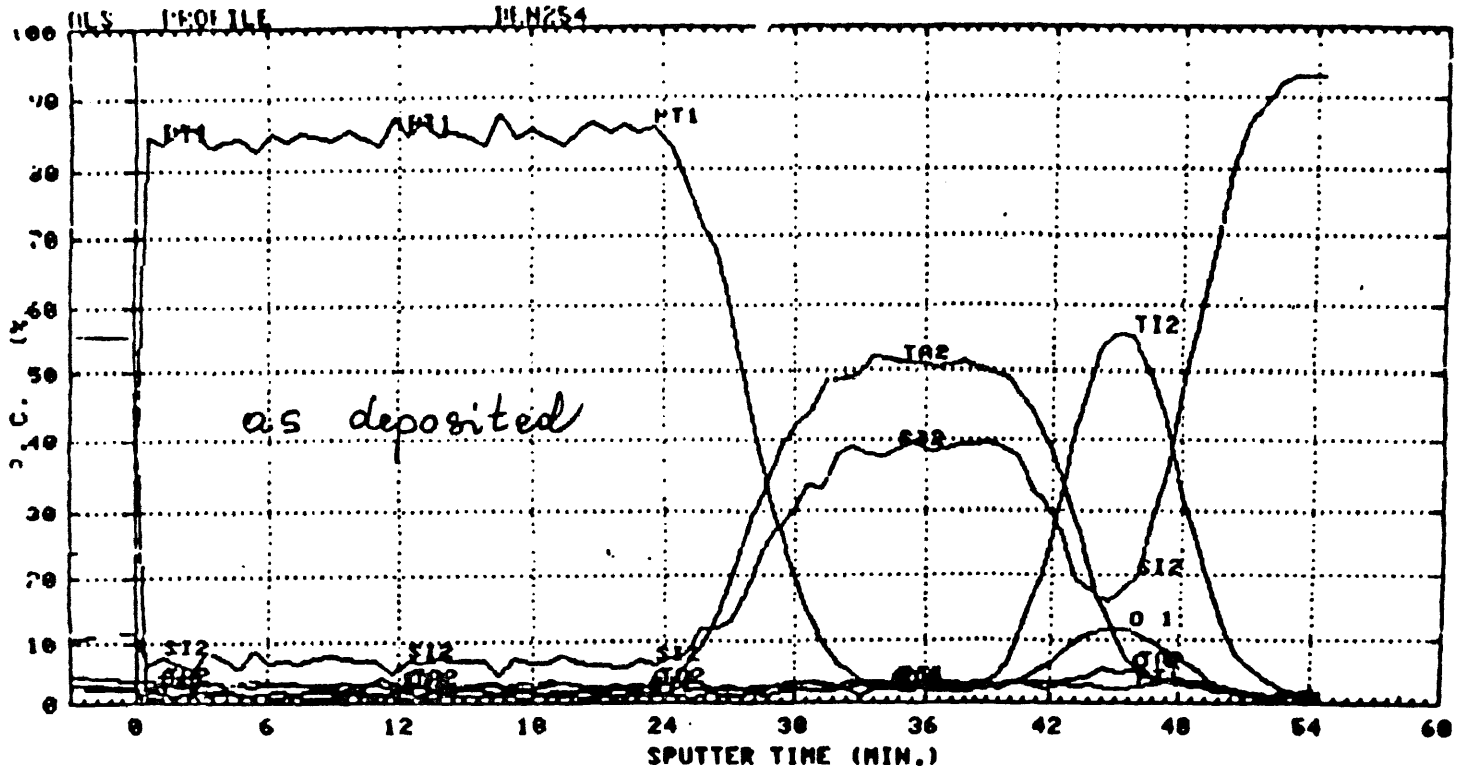

Figure 4-9a

Auger depth profiles taken from a sample in the as-deposited state. The Pt layer as well as the $TaSi_2$ are for all practical purposes free of contamination. The oxygen in the Ti layer is an artifact of he deposition process.

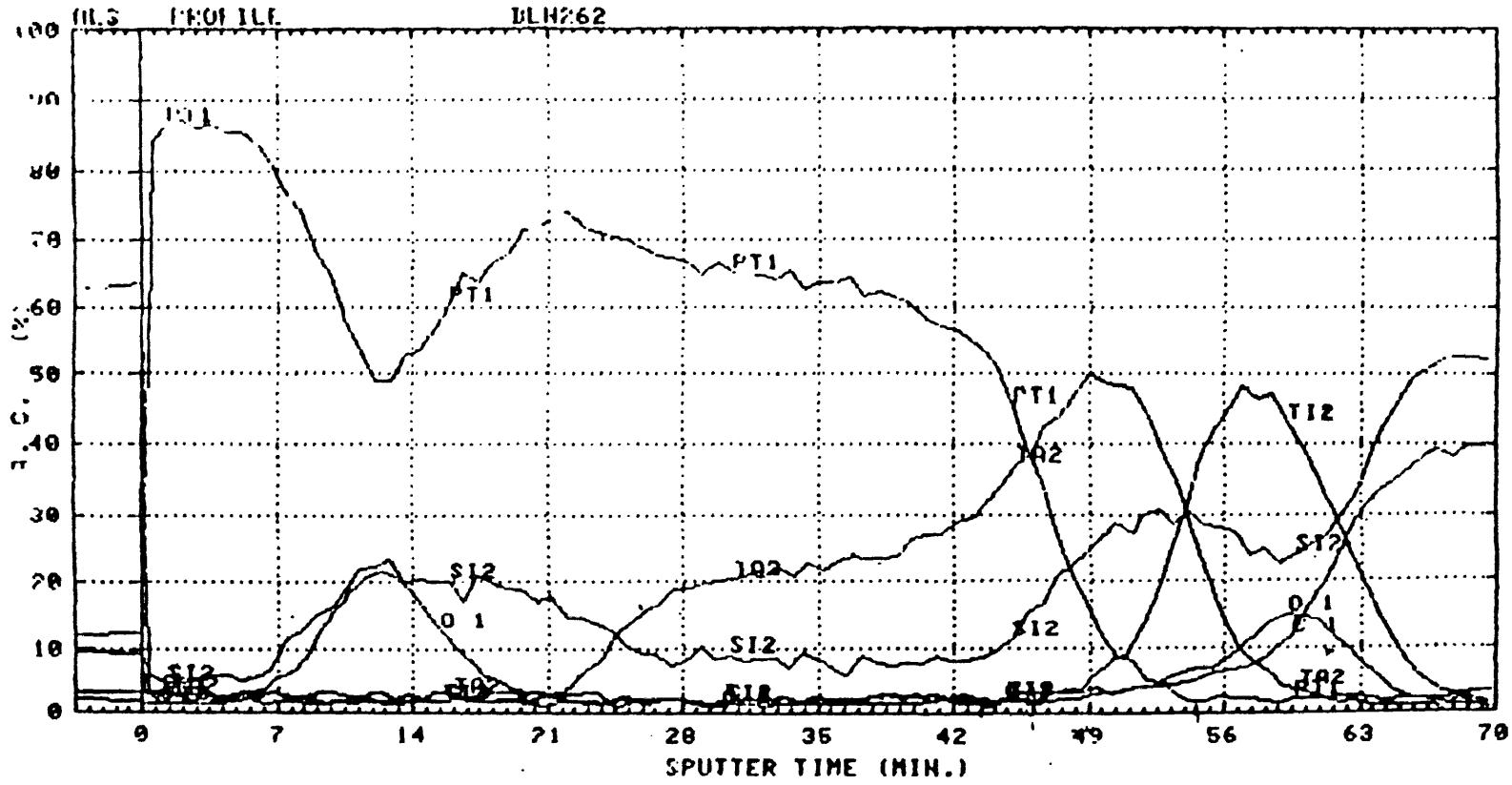

Figure 4-10b

Auger depth profiles taken from a sample heat treated at 600°C for 5 hours. Three main layers and a number of sublayers can be seen.

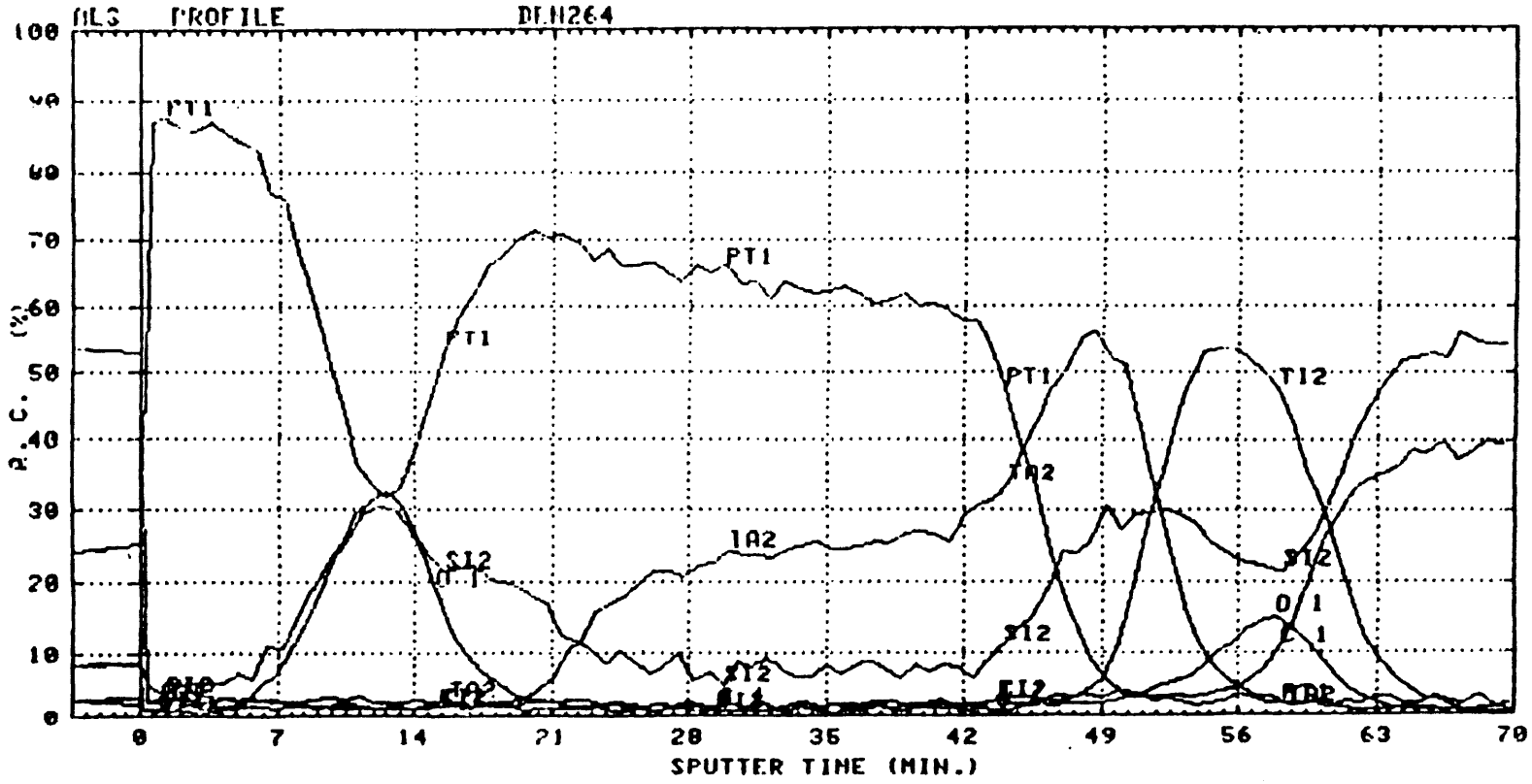

Figure 4-9c

Auger depth profiles taken from a sample heat treated at 600°C for 10 hours. The general picture is the same as in the sample treated at 600°C for 5 hours.

was carried out. Auger spectra were taken from the surface of the sample in the as deposited state, and after 5 and 10 hours at 600°C. Generally, no differences were observed in the obtained results. All spectra revealed the presence of Pt, as well as C and O_2 as surface contaminants. The Auger depth profile of the as-deposited specimen is shown in fig. 4-9a. Three layers can be distinguished. First, at the free surface in the Pt layer, it is free of contamination. The second is the $TaSi_2$ layer, which is also practically speaking free of contamination. The third layer is Ti which is contaminated by O_2(12 at %). It was suspected that this contamination was an artifact of the deposition process. Fig. 4-9b presents the Auger depth profiles in the sample after 5 hours at 600°C. Three main layers and a number of sub-layers can be seen. The first main layer is the Pt layer which can be divided into four sub-layers (1) pure Pt next to free surface (2) Pt + silicon oxide (3) Pt + Si (most probably in the form of Pt silicide) (4) inter-metallic (most probably) between Pt + Ta with some presence of Si. The second main layer is $TaSi_2$ in which presence of Pt and Ti could be observed. The third layer is Ti which contains Si, O_2 (14 at %) and C. The presence of Ta and Si in the Pt layer and the Si in the Ti layer is associated with controlled decomposition of the $TaSi_2$ diffusion barrier, which results in decreased thickness of the barrier. After 10 hours at 600°C the general picture is the same as in the previous sample. This could be seen in fig. 4-9c. However, an increase in the quantity of silicon oxide in the Pt layer, without change in position and decrease in the thickness of the $TaSi_2$ diffusion barrier, as a result of further decomposition were observed.

The most important thing to note is that no penetration of O_2 to the epilayer of SiC was seen. The penetration of O_2 from outside through the Pt layer was prevented by the formation of SiO_2 within the Pt layer. The Si was supplied by $TaSi_2$, which in essence is acting as a sacrificial barrier.

CHAPTER 5

FABRICATION OF 6H-SiC SENSORS

5.1 Overview

The processes associated with fabrication of SiC sensors for high temperature applications were basically directed toward manufacturing of a diaphragm sensor. However, in the intermediate stage, mainly for the purpose of testing and characterization, beam sensors were also designed and fabricated. In this section, both stages of development are discussed with main emphasis on the diaphragm sensor. It should be noted that part of the data associated with the characterization of these novel sensors is presented in the chapter three. Preliminary results obtained in Phase I of the present program indicated that for sensors applications the most suitable temperature dependence of the gage factor was found in the n^+-SiC. Therefore, all beams investigated in the first stage were fabricated from this material.

5.2 Fabrication of Piezoresistors on 6H-SiC Beams

After a series of studies, an initial process flow was established for sensor fabrication. The starting wafer was n-type SiC substrate with a 5.5 μm thick lightly doped p-type epilayer on top of which 2μm thick n-type epilayer is present. Aluminum ohmic contacts are deposited on the n^+ SiC epilayer for potential control in the electrochemical etching process. Platinum was sputtered on the top of the n^+ SiC and patterned. It acts as a mask for the photoelectrochemical etching of the piezoresistors. The n^- SiC epilayer is

photoelectrochemically etched to form the piezoresistors. Subsequently, the platinum mask and the aluminum ohmic contacts are removed from the n^+ epilayer resistor.

The current vs. time curves of a typical piezoresistor etching are shown in fig. 5-1. The photocurrent rises to maximum in the first 20 min, and then drops rapidly. A second maximum appears in the curve after forty minutes. After that time, the current density gradually decreased. The i-t curves were repeatable between the two etching runs as can

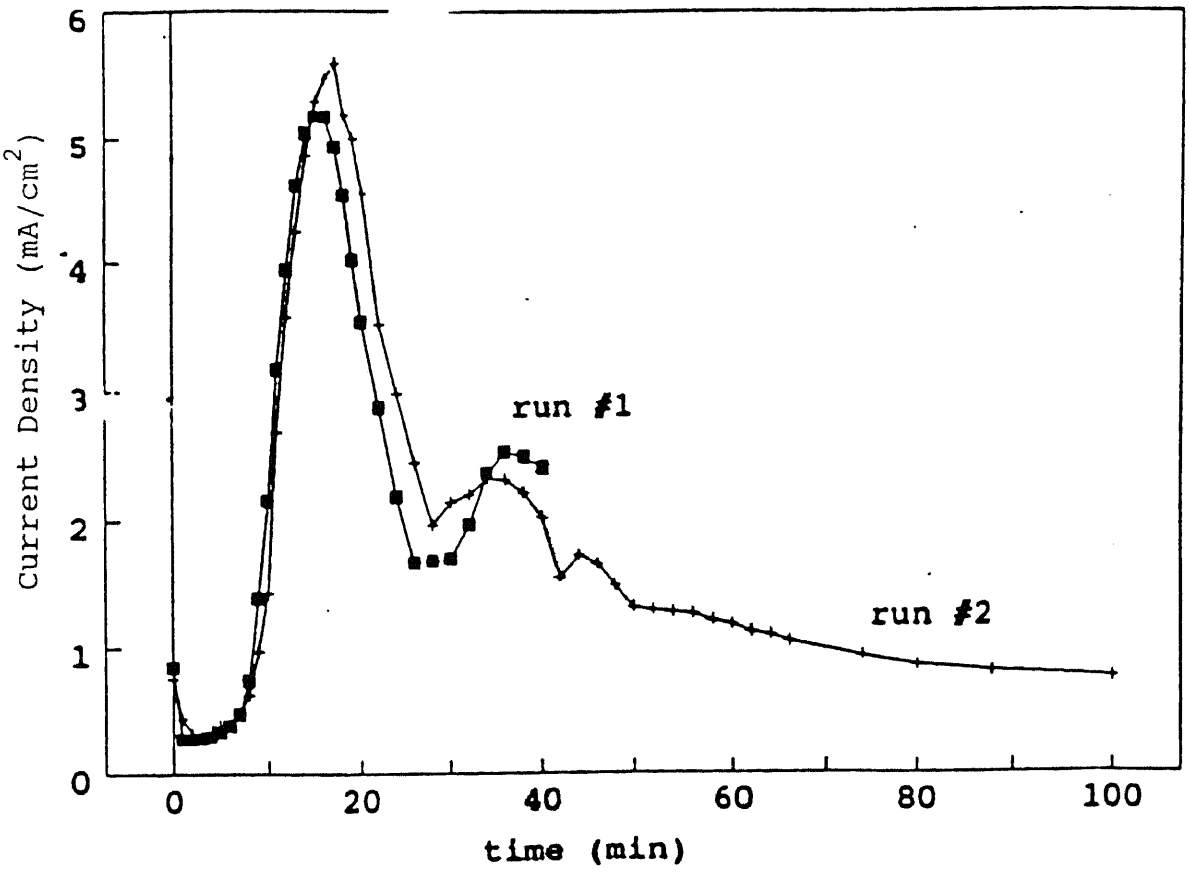

Figure 5-1
Current density vs. time during photoelectrochemical etching of n-(6H)-SiC in dilute HF electrolyte.

be seen. It should be noted that the etch rates of the n-SiC epilayer were rather slow (~ 200 Å/min), because the UV intensity was very low. By increasing the etch rates, the n-SiC epilayer can be etched more rapidly. By increasing the light intensity, it should be possible to increase the n-SiC etch-rate and thus achieve more selectivity between n-and p-type etching.

The wafer is oxidized and then dipped in 49% HF to remove the porous layer that formed during the anodization. The second oxidation is carried out to passivate the junctions and then contact windows are opened in the oxide and nickel was evaporated into the contacts. The nickel was annealed at 1025°C for thirty seconds in vacuum. This is followed by an aluminum evaporation over the nickel, which is then patterned to form the final device

The fabrication of the sensor required thorough investigation of the etching characteristics of the n^+-type SiC. It was established and reported in Phase I that n^+-SiC exhibits large dark current at low voltages. Although the etching potential of n^+-SiC in the dark is much higher than that of p-SiC, it is possible to stop the process at the pn junction if the ohmic contact (for potential control) is made only to the n^+-SiC layer. The anodic potential on the n^+-SiC layer will cause the junction to be reversed biased, preventing current flow into the p-SiC layer. In order for an etch-stop to be effective, the breakdown voltage of the pn-junction must be lower than the etching potential of the n^+-SiC layer and the p-type layer should have a doping level significantly lower than that of the n^+-type SiC.

Another process, which can be utilized to pattern n^+-SiC epilayers, is dark electrochemical etching. When the anodic potential is applied through the contacts on the

n^+-SiC (in the absence of light), current cannot flow between the n^+-SiC epilayer and the underlying p-SiC substrate. Therefore, the p-SiC epilayer should act as an etch-stop. The dark etching experiments, indeed, demonstrated that by utilizing a reverse biased pn-junction, it is possible to achieve an etch-stop on a p-SiC buried epilayer, when the n^+-SiC top layer is being etched in the dark.

One should be aware of the problems, which sometimes arise with the processes of sensors fabrication. For example, platinum is usually used as the mask to pattern the piezoresistors network. When the piezoresistors are etched photoelectrochemically at the potential of $1.7V_{SCE}$, the lightly doped n-SiC exhibits dark etching. The latter may result in undercutting of the gages as well as in etching through the pin holes in platinum, leading to non-uniformity in the resistor patterns, and appearance of pinholes in the resistors. These effects can be minimized by using n-type epilayers with lower doping levels, thereby reducing dark etching at potentials $1.7V_{SCE}$ or by substituting platinum with e.g. polyimide as a mask (no anodization reaction) or with polyimide on silicon nitride. The polyimide may prevent the pinhole formation while the silicon nitride will minimize the effect of undercutting.

The most effective procedure used to neutralize pinholes in platinum, was double deposition. After the deposition of the first platinum layer (1000Å) the film was sputter etched and subsequently the second platinum layer was deposited. Sometimes, after the process of etching the outputs of the device were not steady and the response to loading (pressure) is much lower than expected. This indicated that the resistors are not fully electrically isolated because the resistor bearing epilayer was not etched completely. In

this case, the etching time of the piezoresistor layer had to be increased. This also can be avoided if the isolation of the junction is tested immediately after photoelectrochemical etching. In many cases, the p-SiC layer is not a fully effective etch-stop. This effect was observed in the p-type SiC with low doping levels (N_a~$10^{16}cm^{-3}$). Apparently, in lightly doped material, the electric field in the space-charge region is not high enough to confine all the photocarriers in the bulk and some photocarriers drift to the surface causing etching. In addition, the UV light incident on the pn-junction allowed leakage currents across the junction. Although the anodic voltage was applied through the ohmic contact on the top n-SiC epilayer, the light induced leakage allowed the current to flow through the junction, resulting in etching of the p-SiC. In order to avoid the etching of the p-SiC epilayer the reference voltage (V_{SCE}) must be reduced to a level, which curtails photocarrier injection.

It should be noted that this fabrication procedure described above can be adopted to produce resistors in n-type epilayers with any doping level. A generic fabrication process flow is presented in appendix A.

5.3 Fabrication of Daphragms

The characteristics of a diaphragm sensor device, with resistors either diffused or etched from epitaxially grown layer, is determined by the piezoresistors and by the dimensions of the diaphragm. The dimensions, which characterize any circular diaphragm are thickness and radius. Since the radius is generally a fixed value it leaves thickness as the main controlling variable. Therefore, the process of etching of the diaphragm to achieve the

desired thickness and shape is of primary importance in diaphragm sensor technology. The SiC technology has advanced significantly over the last decade. However, the application of SiC diaphragms in sensing devices was, in the past, almost nil basically because of its inert chemistry. There are a number of molten metals and molten salts that react with SiC[29], but these are impractical etchants for device fabrication. Some structures have been selectively etched in SiC using reactive ion etching (RIE), however, the etch rates reported[30] were very low for wafer thinning and shaping. Carrabba[31] used photoelectrochemical etching, but the visible light source used in his study resulted in very slow etch rates. Shor *et. al*[32] utilized UV laser radiation and achieved very high rates of etching, though, the morphology of the etched features, as observed previously [29, 30] was very rough. An important contribution to the etching technology was the effect of dopant-selective etch stops demonstrated by Shor *et. al*[33].

In order to fabricate a SiC diaphragm transducer, a fully controllable etching process for thinning and forming of deep cavities must be developed. The desirable etch rates should be in the range of 1μm/min. and require dopant selective etch stops. It has been shown[1], that by utilizing dark electrochemical etching in dilute HF, cavities with depth greater than 100 μm in both p- and n-types 6H-SiC could be fabricated. In many cases it was observed, that a porous layer had been formed as a result of the etching. The appearance of this layer depended on the concentration of HF in water. At low concentrations (0.6% HF) the etching occurs with a resultant soft highly porous layer, while at higher concentrations (2.5% HF) a layer of low porosity was formed. Both layers can be removed by oxidation. Since, the commercially available wafers are of thickness

150 μm after being lapped and polished, the etching process described above can be in principle utilized to form a sensor diaphragm.

In n-SiC, dark anodic etching is possible only when the voltage is sufficiently high to cause the semiconductor space charge layer to break down. Under these conditions, electrons are injected from the SiC/HF interface into the bulk of the semiconductor resulting in dissolution reactions at the surface. The voltage required for the breakdown depends on the doping level of the semiconductor and the concentration of the electrolyte. In the early stages of this work two dark etching experiments were conducted with n-SiC: a) anodization in a dilute HF in a two electrode cell (SiC -anode platinum counterelectrode) and subsequent thermal oxidation to remove the porous layer and, b) anodization in a dilute HF in a three electrode configuration (SiC-anode, Platinum-counterelectrode, reference calomel electrode) and oxidation to remove the porous layer. Both experiments demonstrated rapid etching of n-SiC. In the first the average etch rate was 0.3μm /min. while in the second the etch rate was 0.8 μm /min. At current densities used in both experiments one would expect higher etch-rates, assuming etching is the only process occurring. It seems, however, that other parallel processes occur e.g. water decomposition, which uses up part of the current. Two important observations were made in the course of studies of the etching process: a) rapid etch undercutting of the black wax encapsulant, which occurs at higher rates than the vertical etching, b) high impedance associated with the conductivity of the electrolyte which limited the etching at high current densities. Undercutting results in erroneous current density measurements, since the area of the specimen is not well controlled.

Materials must possess certain properties to be used as a mask. In a dilute HF the mask ought to be inert in the concentrations used and no electrolytic reaction should occur during anodization which might interfere with the etching process. Two masking materials were considered. Platinum, which is very resistant in HF, but at anodic potentials higher than $2V_{SCE}$ gas bubbles form on the surface, resulting in non-uniform etching. Silicon nitride is an insulator and, therefore, bubbles do not form on the surface. However, it is not completely resistant in HF. The process of etching of diaphragm is time limited, therefore, an absolute resistance of SiN in diluted HF is not required. It would be satisfactory if the CVD grown SiN layer withstands the dilute HF for the time the diaphragm is etched. In order to test the resistance of SiN, layers 1200Å thick were deposited by low Pressure chemical vapor deposition (LPCVD) and subsequently patterned using a platinum mask and phosphoric acid etching. The films were then kept in 2.5% HF and 0.625% HF until the SiN layers were dissolved. Using the time required for the dissolution the average etch rates were calculated. They were found to be 8Å/min. in 2.5% HF and 1Å/min. in 0.625% HF. The results indicated that in both solutions the SiN film lasts long enough to complete an etching of a n-type SiC diaphragm. Consequently, SiN was selected as a masking material to etch deep patterns in the n-type SiC. The initial results were negative. Inspection of the specimens after thirty minutes of etching revealed the presence of high density of etch pits in the masked areas (~5000/cm^2). Longer etching times (~100 minutes) resulted in coalescence of the etch pits and subsequently delamination of the SiN mask. Figure 5-2 presents SEM micrographs of an etched sample anodized in 2.5% HF at a potential $9.45V_{SCE}$ for 70 minutes. The current density was

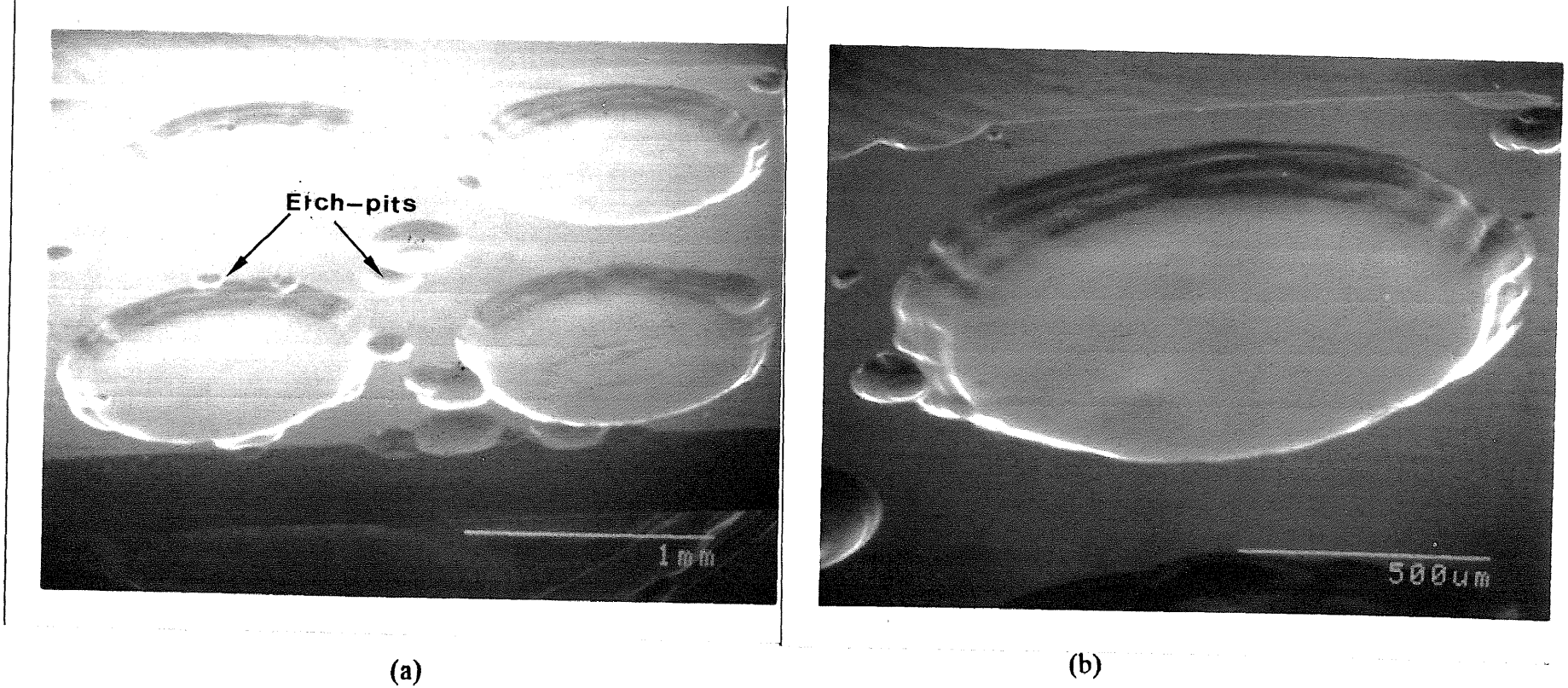

Figure 5-2
SEM micrographs of etched cavities in n-type 6H-SiC. a) At low magnification. b) At higher magnification. Etch-pits are marked by arrows.

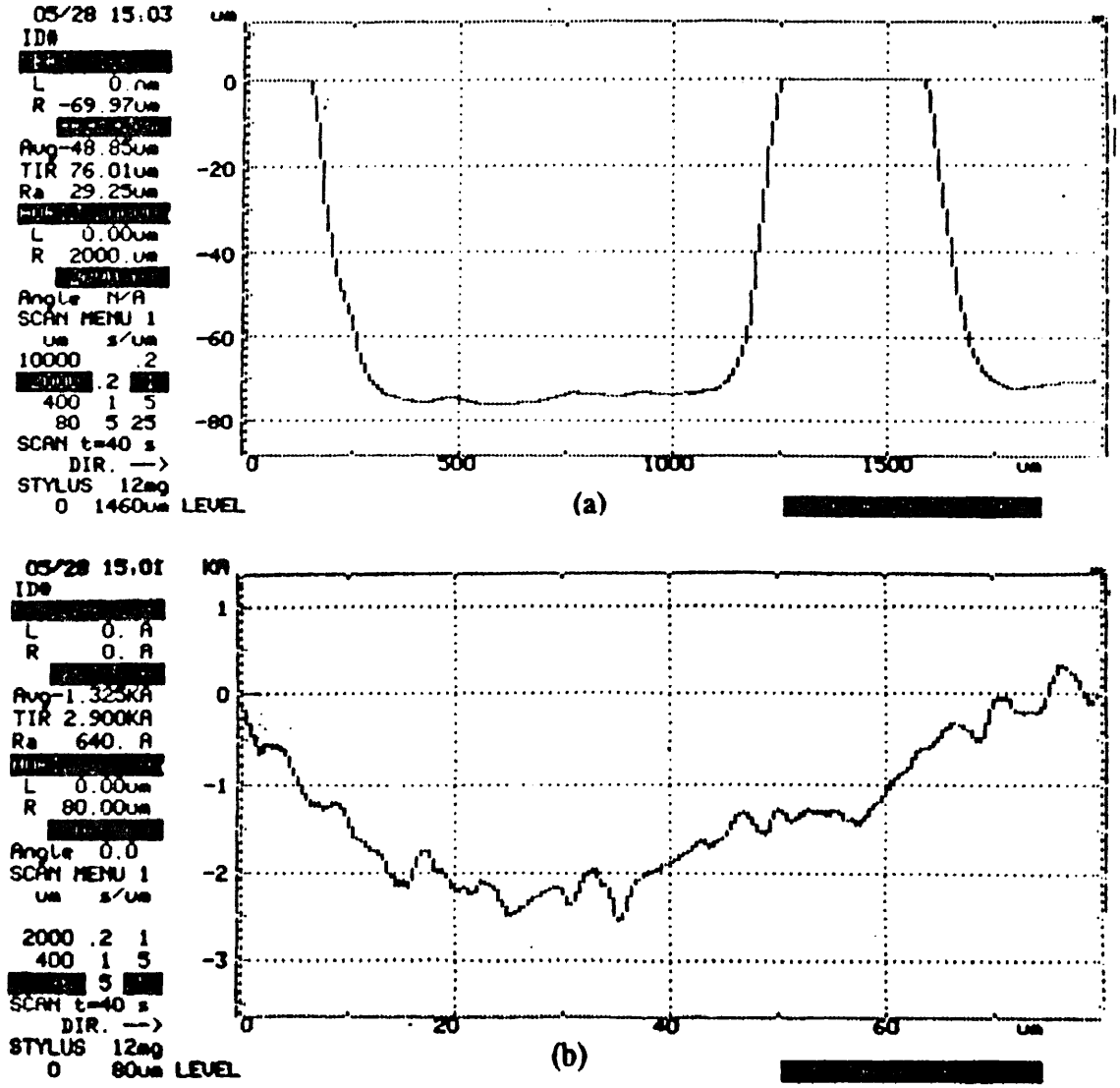

Figure 5-3

Profiles of a) etched cavity, and b) bottom surface of the cavity. The cavity is shown in figure 5-2.

roughly 100mA/cm^2. After anodization the sample was oxidized and dipped in 49% HF to remove the porous layer formed during the process. Depth and the surface roughness of the bottom of the etched cavity (profiles) are shown in fig. 5-3. The depth of the cavity was measured to be 70μm and the surface roughness was approximately 500Å. The variation of the depth across the cavity was 2-3%. Presence of pits observed in the previously masked areas was attributed to the pinholes in SiN. Another sample was etched under conditions similar to previous runs, but for a longer time (120 min.) and shown in the SEM micrograph of fig. 5-4. Profilometry measurements (see fig. 5-5) indicated a uniform depth of 100μm and surface roughness of 500Å. The etch pits present on the etched surfaces (see fig's 5-2 and 5-4) are associated with presence of micropipes in SiC. The porous layer, formed during the anodic etching, could be removed by oxidation followed by a 49% HF dip, or by mechanical means.

The above, briefly described, series of investigations lead to a few important experimental conclusions: at a fixed voltage a) etching in 2.5% HF occurs at higher rates than in 0.625% HF, b) etching in 2.5% HF results in deep etch pits on the surface of SiC, while no etch pits were observed on surfaces etched in 0.625% HF. This can be explained by electrochemical interactions between the electrolyte and the micro-piped substrate, c) the surface of the etched feature was smoother and the depth more uniform when etched in 2.5% HF. In an attempt to optimize further the etching process for forming n-SiC diaphragms, an additional series of experiments were carried out with different etching parameters and concentrations of HF. A new deficiency was observed to emerge during etching at concentrations 1.5 HF, namely formation of hillocks. These features, ranging in

size between 10 to 50μm, seem to form randomly on the diaphragm surface. Figure 5-6 shows an example of a cavity which exhibits hillocks on the surface. Figure 5-7 presents a contour of a bottom surface of a cavity displaying an etch pit and a hillock. The presence of non-controllable discontinuities of this size results in non-uniformed stress distribution with all the consequences with regard to the operation of a sensor. Figure 5-8 presents plane-view optical photo of a finished sensor, using backside illumination. This method enables a qualitative image analysis of the non-uniformities in the diaphragm. The black spots, seen on the diaphragm indicate the presence of the hillocks (see fig. 5-8). The bright white spot represents either an original micropipe in the SiC substrate, or micropipe enlarged by the etching process.

Although, the cause of the hillocks formation has not been determined conclusively, there are indications that the formation is associated with bubbles generated during the high-rate etching. However, it should be stated, that process conditions have been established experimentally to obtain hillock-free diaphragms. Knowledge acquired from all the experimental studies and theoretical evaluations, finally, lead to a process which resulted in etch-pits-free and hillocks-free diaphragms. The pinholes present in the SiN mask were also neutralized. The complete process for diaphragm fabrication is presented in appendix A.

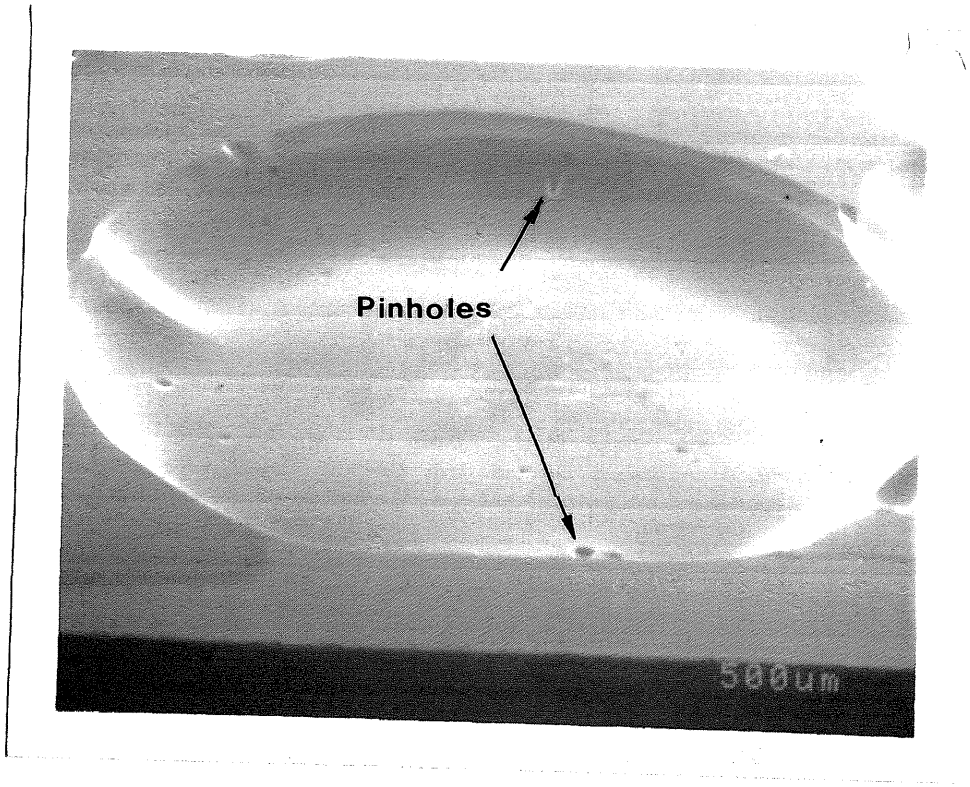

Figure 5-4
Cavity etched for 120 minutes. Pin-holes are marked by arrows.

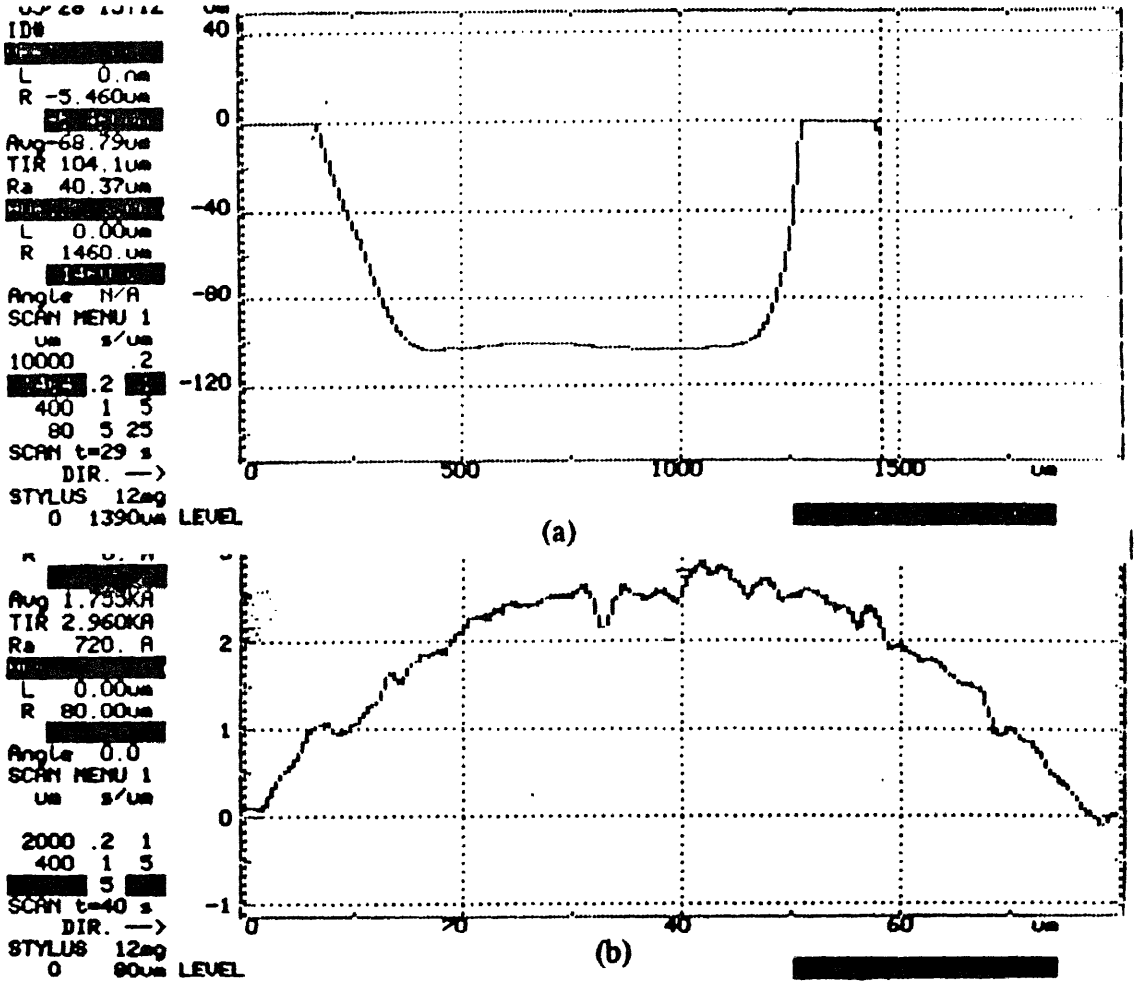

Figure 5-5:

Depth profilometry of the cavity shown in fig. 5-4 indicates a uniform depth of 100μm(a), roughness of the bottom surface is ~500Å (b).

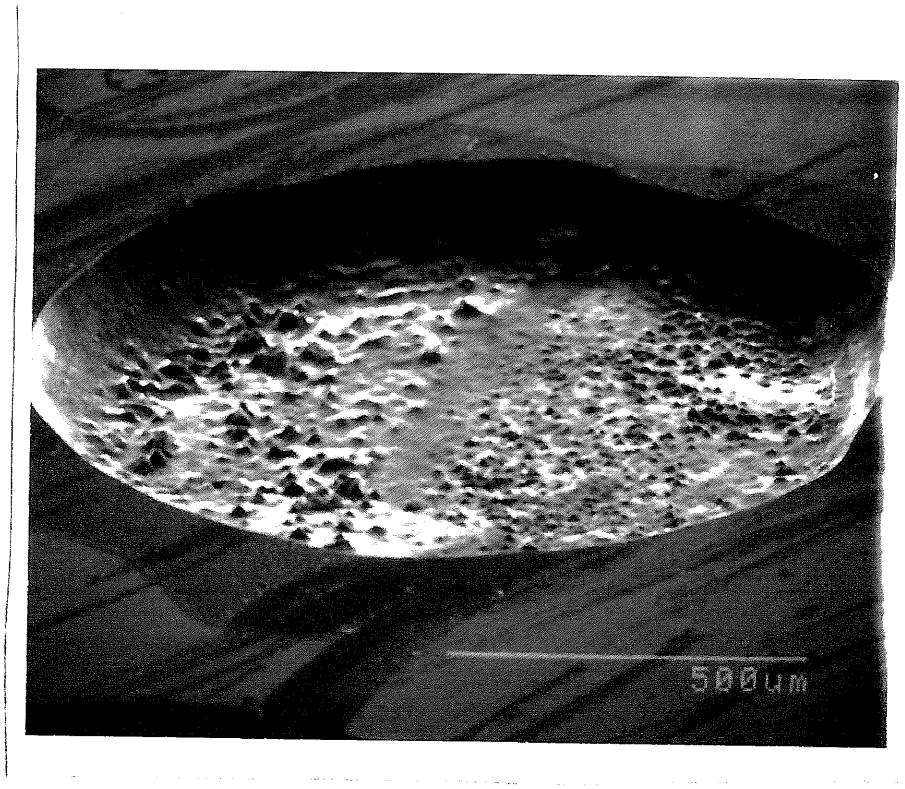

Figure 5-6:
SEM photo micrograph of an etched cavity with hillocks on the bottom surface.

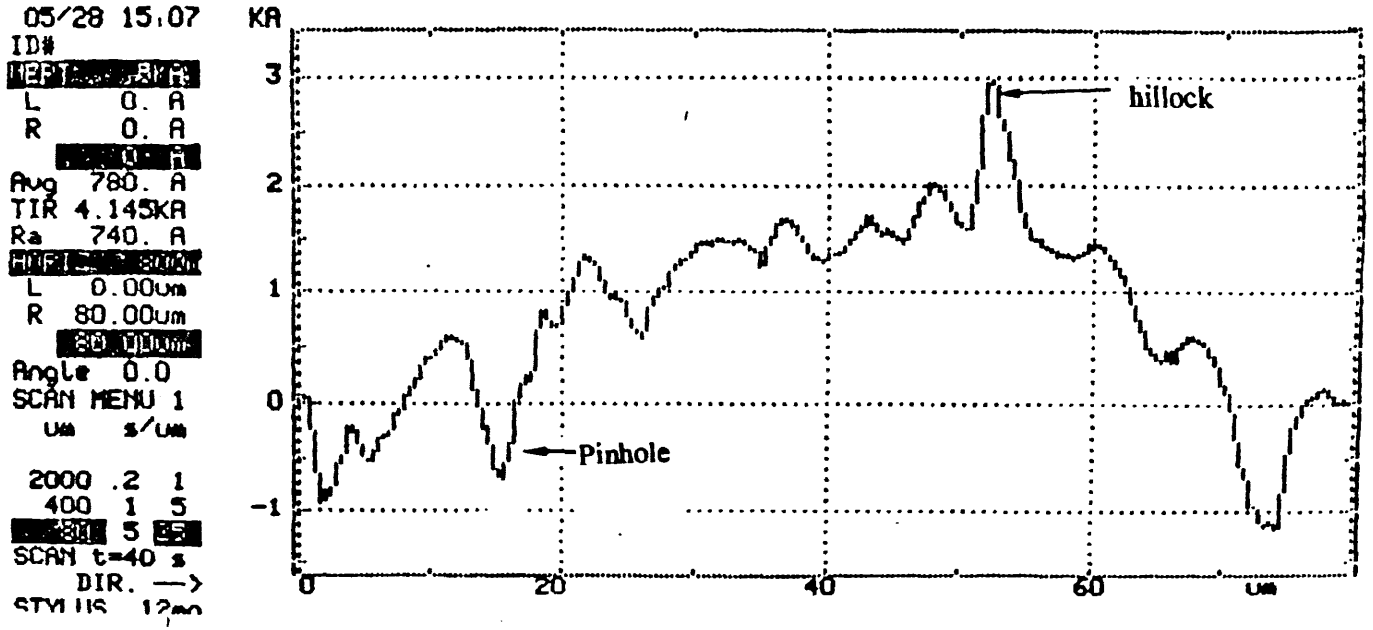

Figure 5-7:
Depth profilometry of the bottom of an etched cavity. Presence of an pinhole as well as hillock can be observed.

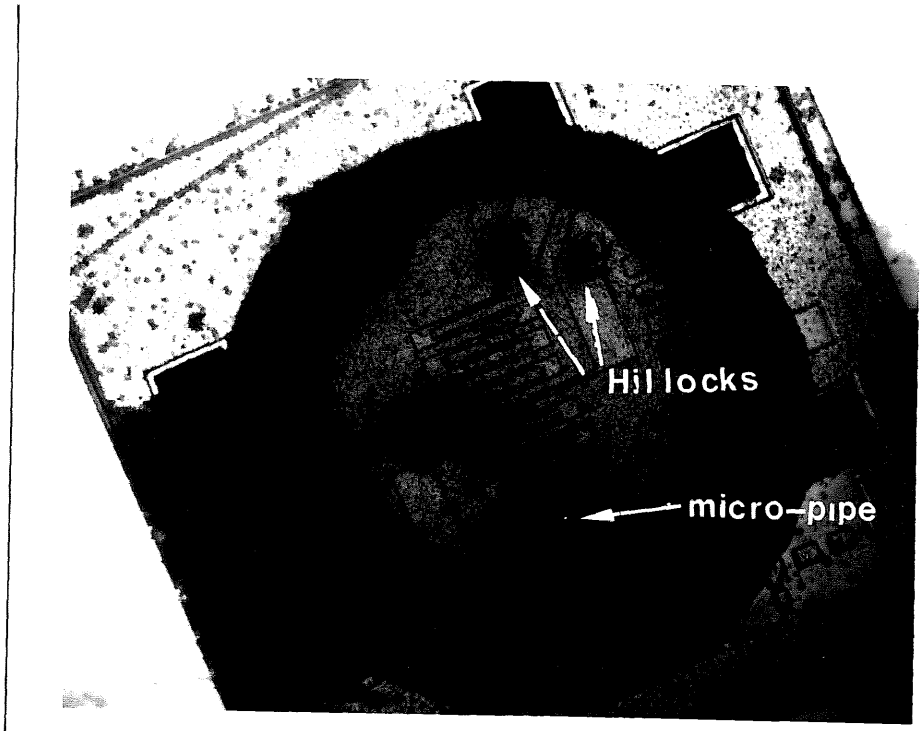

Figure 5-8:
Plan-view optical photograph of fabricated 6H-SiC sensor using backside illumination. The marked black spots indicate presence of hillocks, while the bright spot is a micropipe in the SiC substrate.

CHAPTER 6

TESTING OF SENSORS

6.1 Sensor Performance Characteristics (n-type epilayer doping level $2x10^{19}cm^{-3}$)

The initial testing of sensors with epilayer doping level of $2x10^{19}cm^{-3}$, mounted on headers and packaged in a screw housing was carried out at room temperature. The pressure transducer was of gage type i.e. referenced to atmosphere through a tube in the back of the diaphragm. Pressure was applied through a dead-weight tester apparatus. The output characteristic of the sensor is shown in fig. 6-1. The unit exhibited a linear output over the entire range of pressures applied (1000psi). The sensitivity of the transducer was found to be 0.035 mV/psi for a 5V excitation. The hysteresis, defined as maximum deviation in the output after a single pressure cycle at room temperature, was 0.06%/FSO. Only one cycle of testing was carried out. The voltage can be increased in SiC, since it is a high power semiconductor, and it will result in a higher output, but the null shift will also increase proportionally to the excitation. The same sensor was tested at pressures up to 1000 psi in two subsequent thermal cycles: the first from room temperature to 280°F and the second from room temperature to 450°F. Incidentally, temperature and pressure cycling of sensors often causes changes in gross output, which limits the accuracy of the transducer. In the first cycle, the maximum hysteresis was found to be 1.7%/FSO and the maximum null shift was 2.2%/100°F. In the second cycle the characteristic of the device was even worse: hysteresis was 2.6%/FSO and the null shift was -2.8%/100°F. However, it should be stressed that both the sensitivity and the linearity were closely replicated in both cycles. The temperature coefficient of resistivity (TCR) showed a positive shift from -

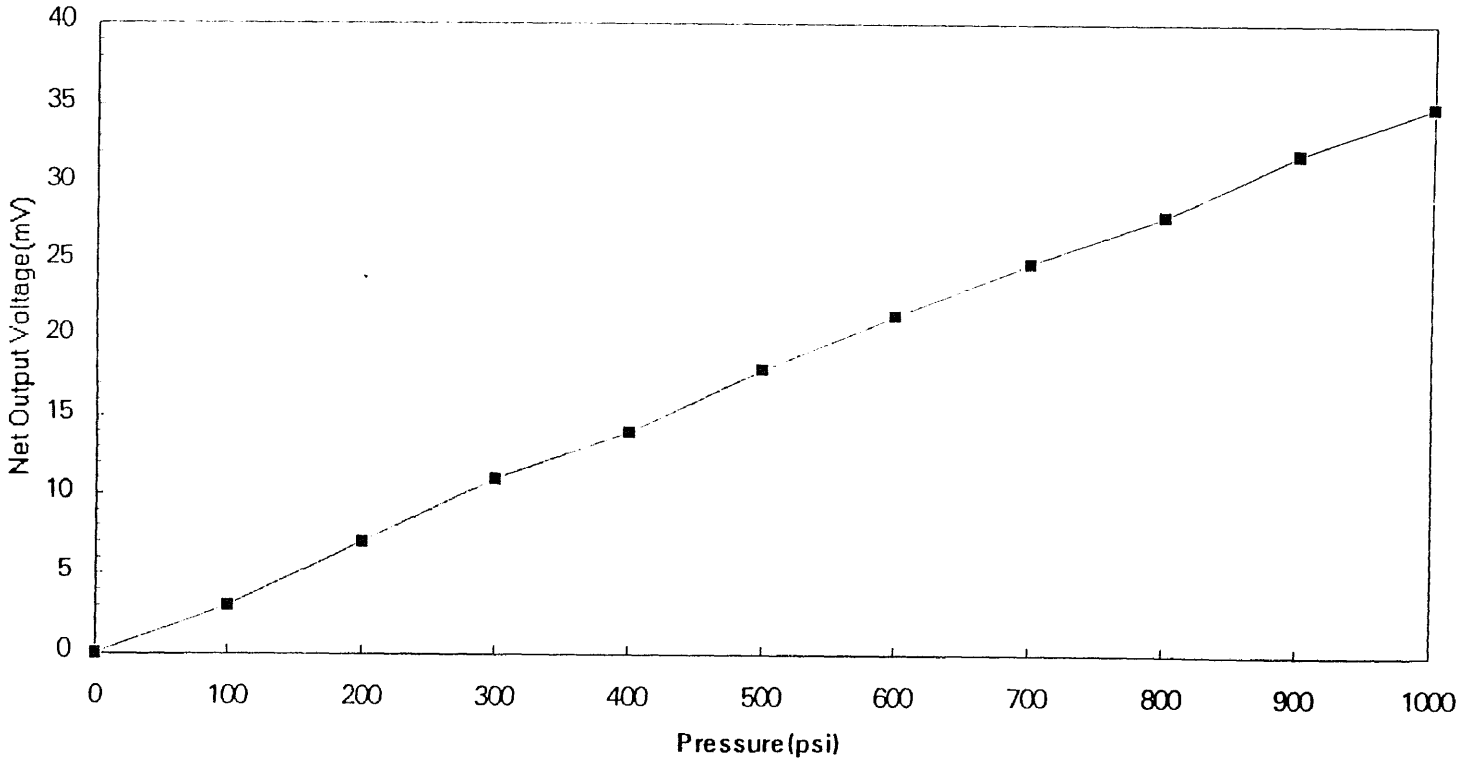

Figure 6-1
Output characteristic of n^+6H-SiC sensor mounted on header in a screw housing.

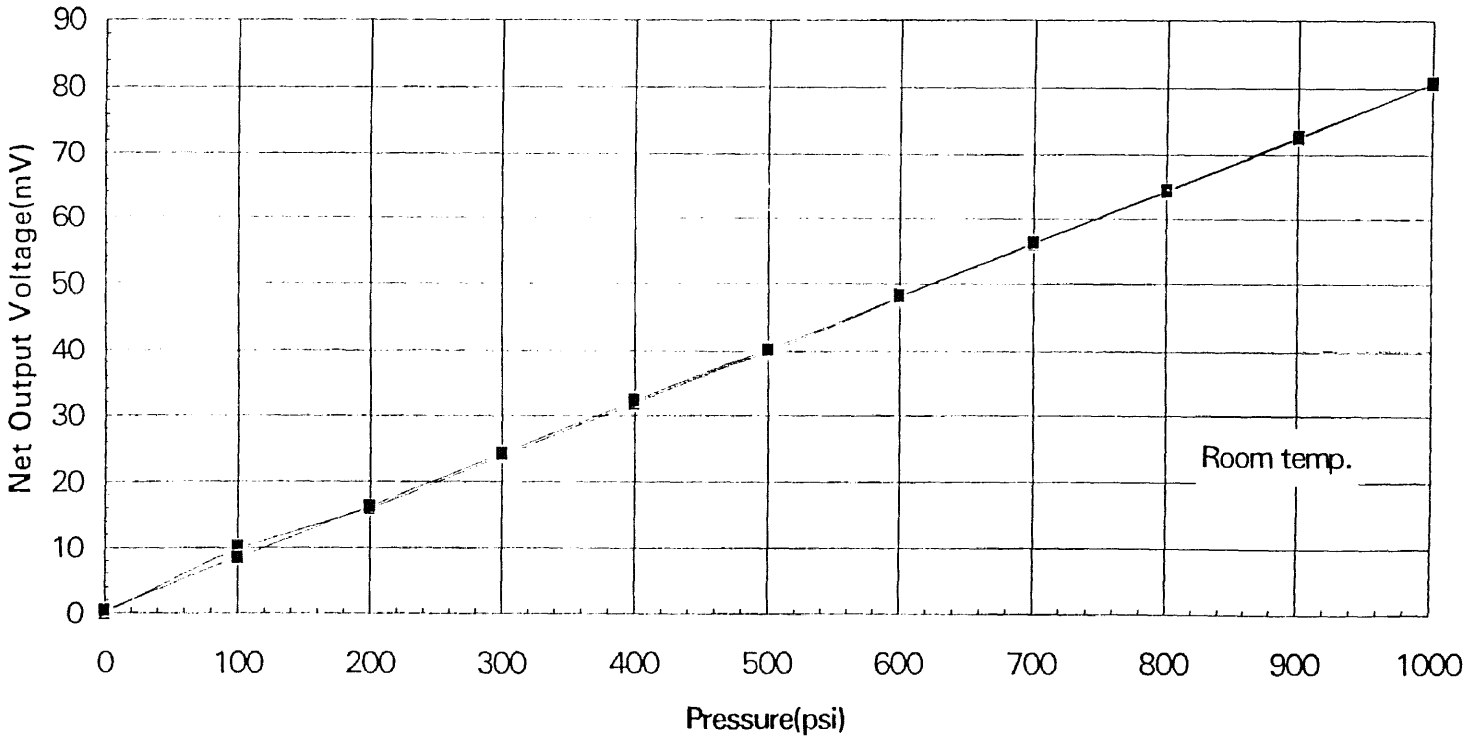

Figure 6-2
Net output vs. applied pressure at room temperature(sensor 1).

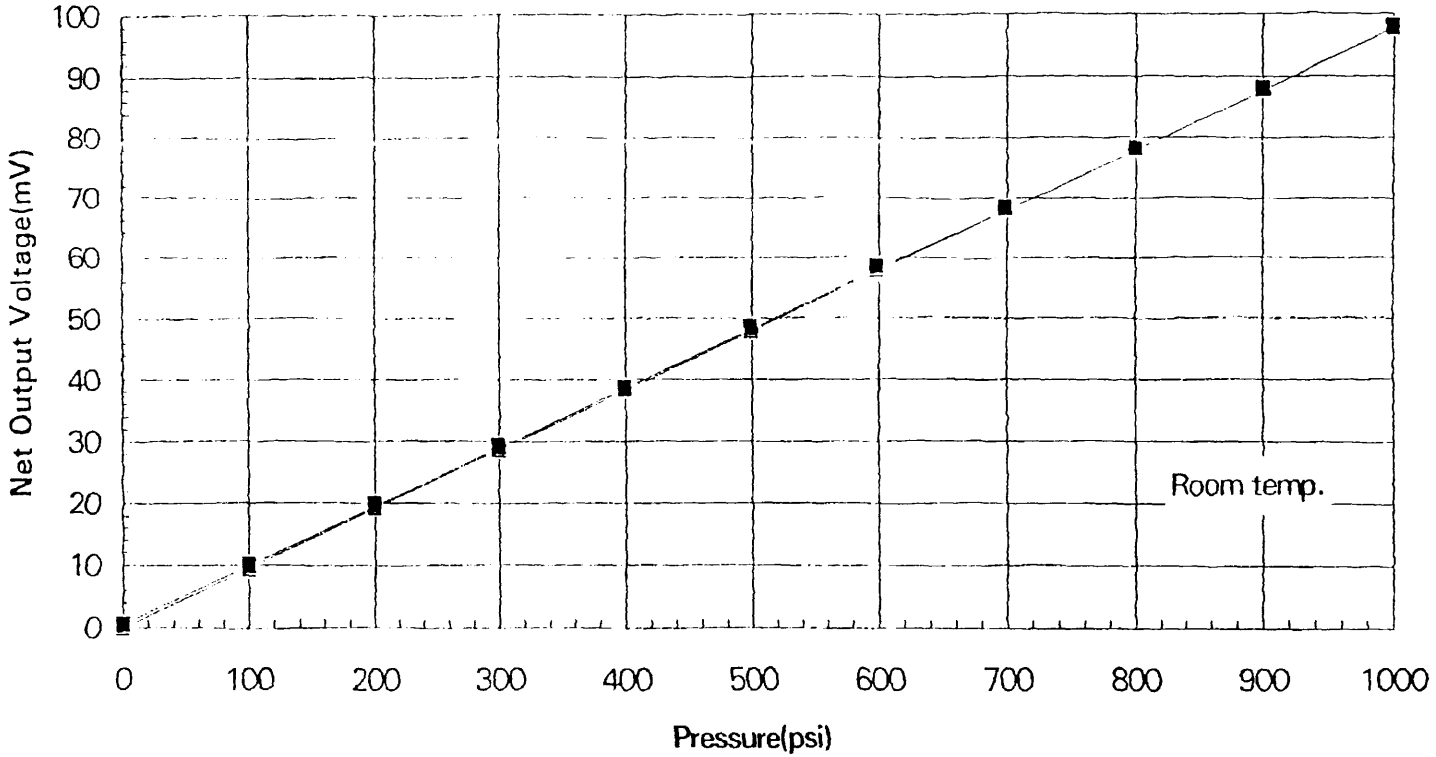

Figure 6-3
Net output vs. applied pressure at room temperature(sensor 2).

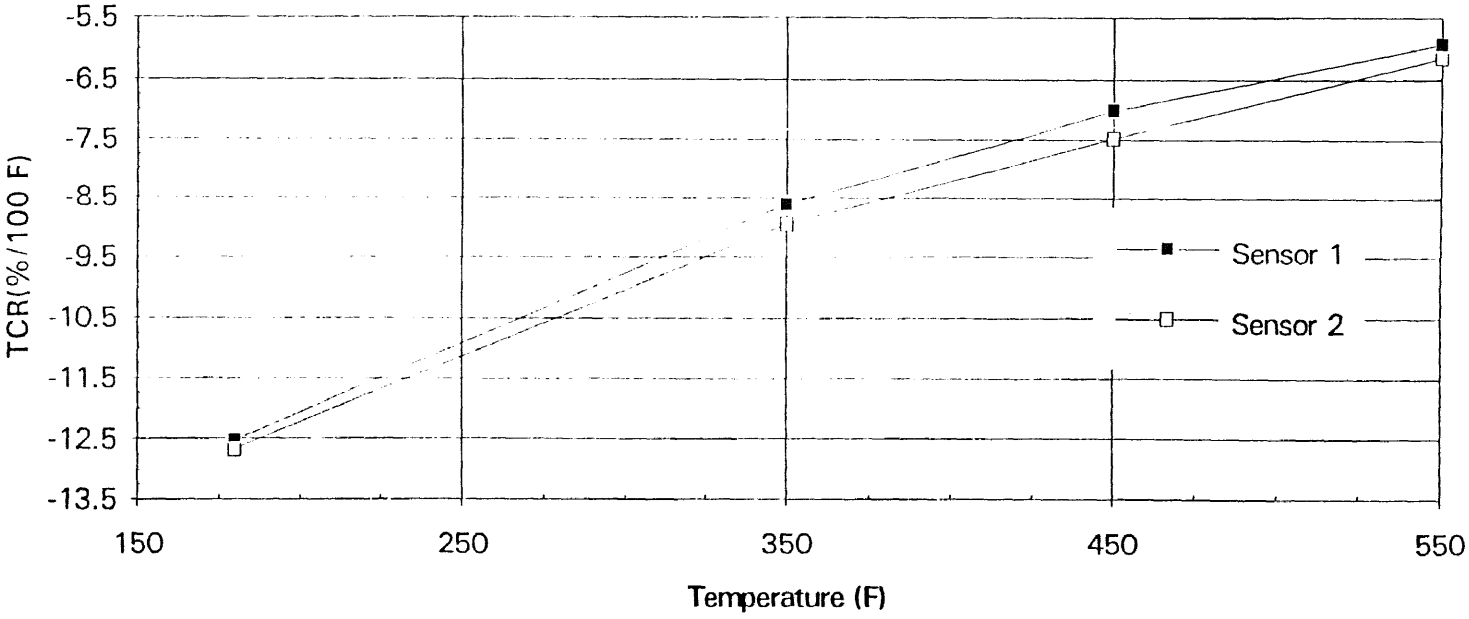

Figure 6-4
Temperature coefficient of resistance(TCR) as function of temperature(sensors 1 and 2).

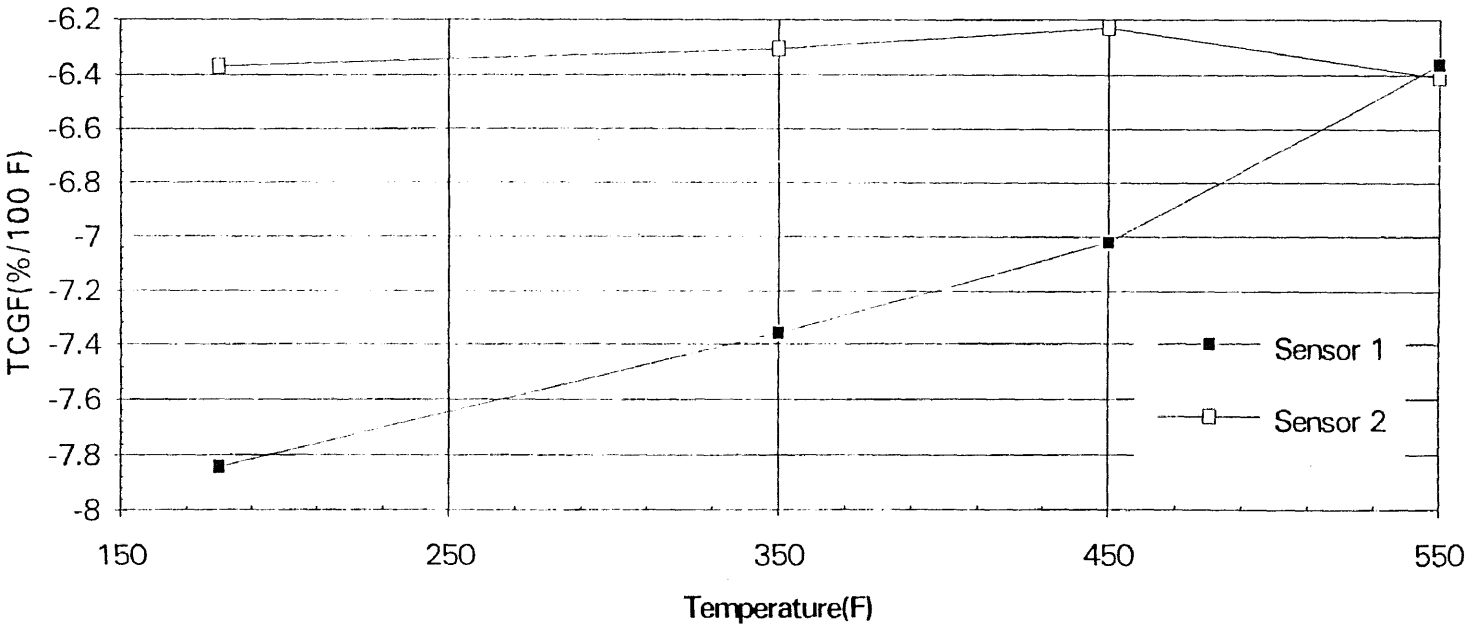

Figure 6-5
Temperature Coefficient of Gage Factor(TCGF) as function of temperature(sensors 1 and 2).

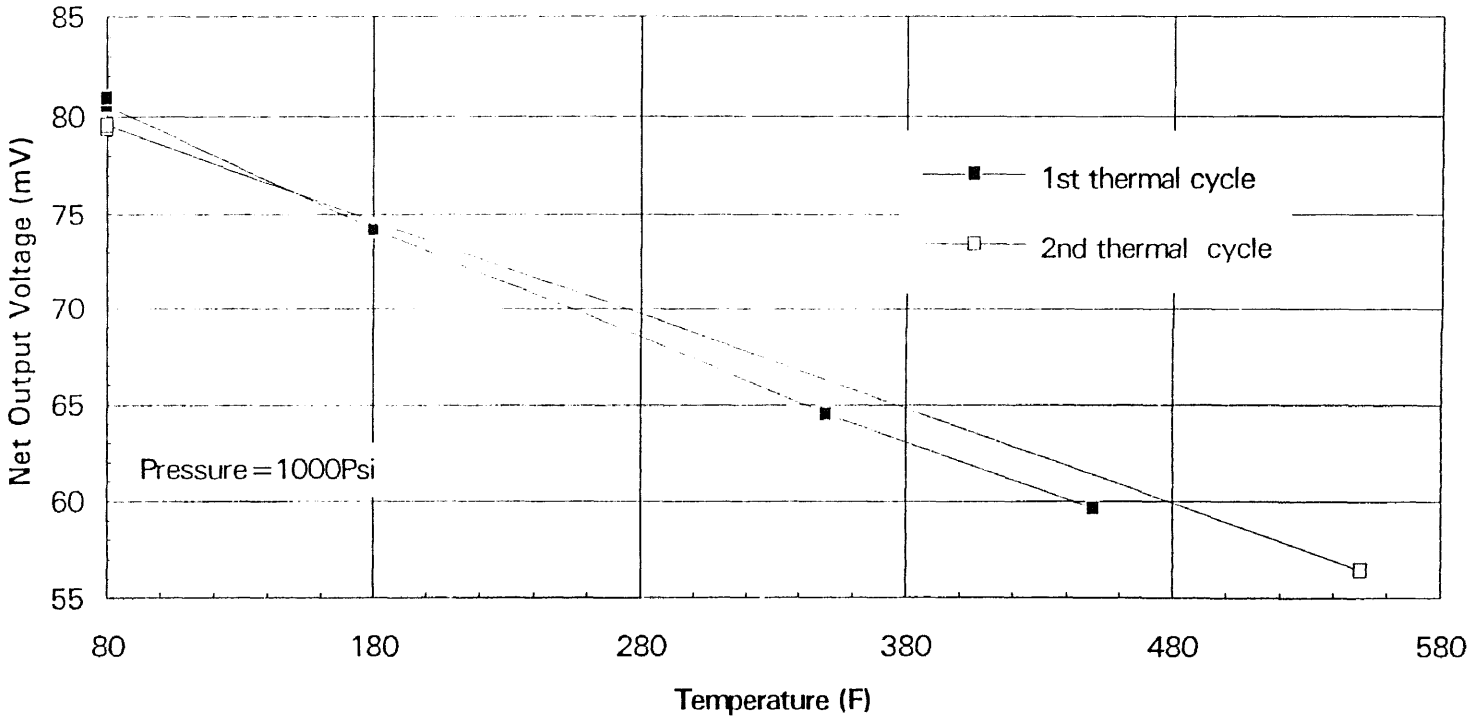

Figure 6-6
Temperature effect on Full-Scale Output(FSO) during two thermal cycles(sensor 1).

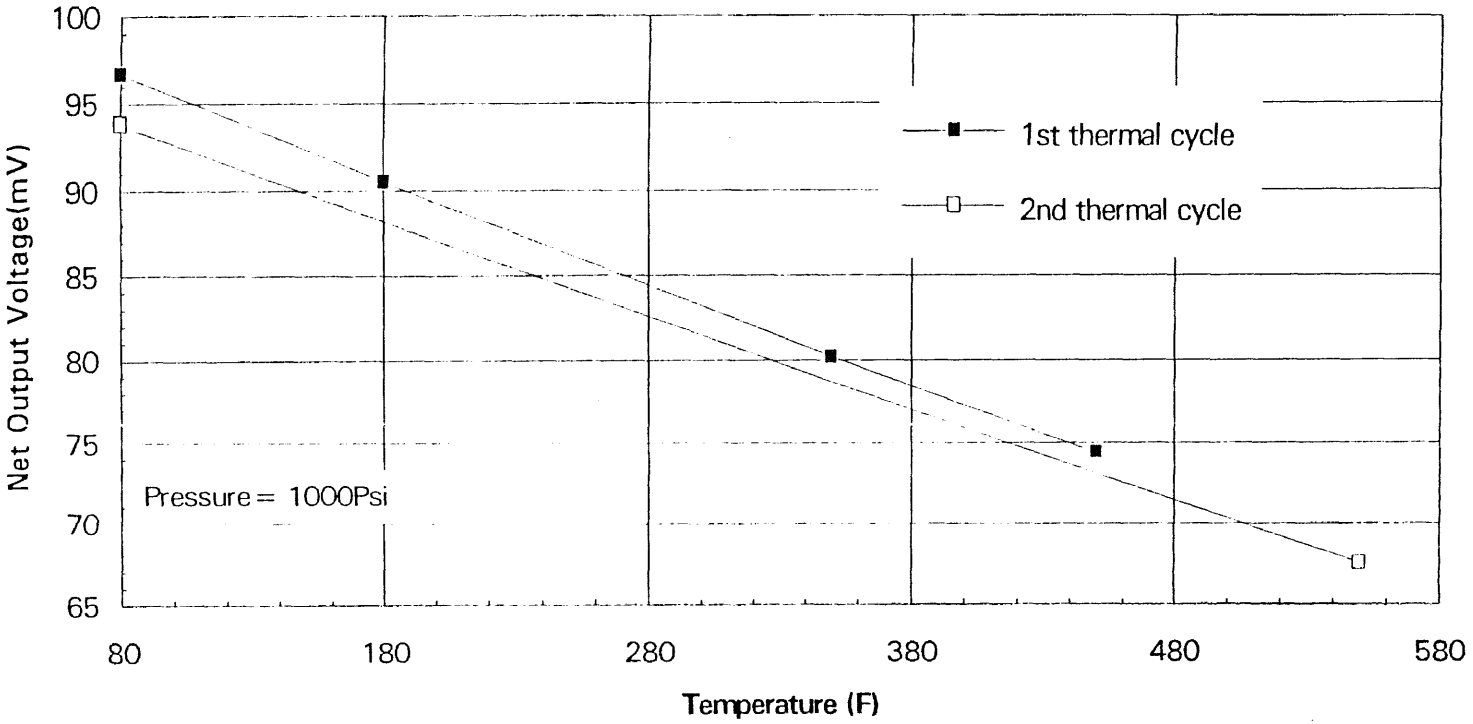

Figure 6-7
Temperature effect on full-scale output(FSO) during two thermal cycles(sensor 2).

12.9/100°F(80°F-180°F) to -10.1%/100°F(80°F-280°F). At the same temperature ranges the temperature coefficient of gage factor(TCGF) changes from -7.6%/100°F to -8.6%/100°F.

In another set of experiments, two packaged sensors, randomly chosen from a big batch, were tested in temperature ranges between 80°F and 550°F. The room temperature net output voltage as a function of applied pressure in the range up to 1000 psi is shown in fig. 6-2 (sensor 1) and fig. 6-3(sensor 2). The tabulated characteristics of both sensors, obtained in two thermal cycles (80°F--->450°F--->80°F and 80°F---> 550°F--->80°F) are very similar and are presented in appendix B. The difference in the full scale outputs 80.56mV vs. 96.68 mV can be attributed to the difference in the diaphragm thickness. Both sensors exhibited negative TCR's (see fig. 6-4), and the results were comparable. However, TCGF results shown in fig. 6-5 are not fully in agreement. The temperature effect on the full scale output (FSO) during the two thermal cycles for both devices is presented in figs. 6-6 and 6-7. The experimental data obtained on the second set of packaged sensors was substantially better, as compared to the data obtained on the first set of sensors built. It demonstrated for the first time a working device fabricated of 6H-SiC capable of operating up to 550°F.

6.1 Sensor Performance Characteristics (n-type epilayer doping level $1x10^{18}cm^{-3}$)

The next series of transducers was fabricated, but the upper n-SiC epilayer had a doping level of $1 \times 10^{18}cm^{-3}$. The characterization measurements were carried out on a randomly chosen sensor. It had a diaphragm thickness of approximately 25μm and was glass

mounted to a header. The experiments were performed in the range of temperatures between 80°F and 500°F. Figure 6-8 presents the effect of temperature on the functional dependence between the net output voltage and applied pressure. At room temperature at the full scale pressure (1000 psi), the observed output voltage was 131.59mV but it decreased with increasing temperature. At 500°F it was 77.23 mV. The hysteresis and the linearity (see appendix C) were calculated to be 0.43%/FSO and 0.004%/FSO respectively. The room temperature null shift (the difference between initial zero pressure output and the value upon return to zero from maximum pressure), was found to be 0.17%/FSO. The effect of temperature on the net output voltage at constant pressure (1000psi) is shown in fig. 6-9. It permits to calculate the average temperature sensitivity at any range of temperatures. The output sensitivity at full scale pressure of 1000psi, in the range 80°F -500°F, was calculated to be 0.26%/100°F. The temperature coefficient of resistance (TCR) vs. temperature is shown in fig. 6-10. At first it exhibited negative values, e.g. at 180 °F the TCR was -3.07/100°F, but at 280°F it assumed positive values and at 500°F the TCR was 4.24/100°F. At higher doping levels (2 x $10^{19}cm^{-3}$) TCR remains negative even above 500°F. This TCR characteristic is consistent with the brief explanation given in chapter three. However, the TCGF, shown as a function of temperature in fig. 6-11, exhibited more negative values than those found in n^+-type SiC. Appendix 3 presents a complete thermal cycle performance characteristics of the tested sensor.

In conclusion, it can be stated that the presented testing results indicate the start of a new generation of sensors fabricated from 6H-SiC.

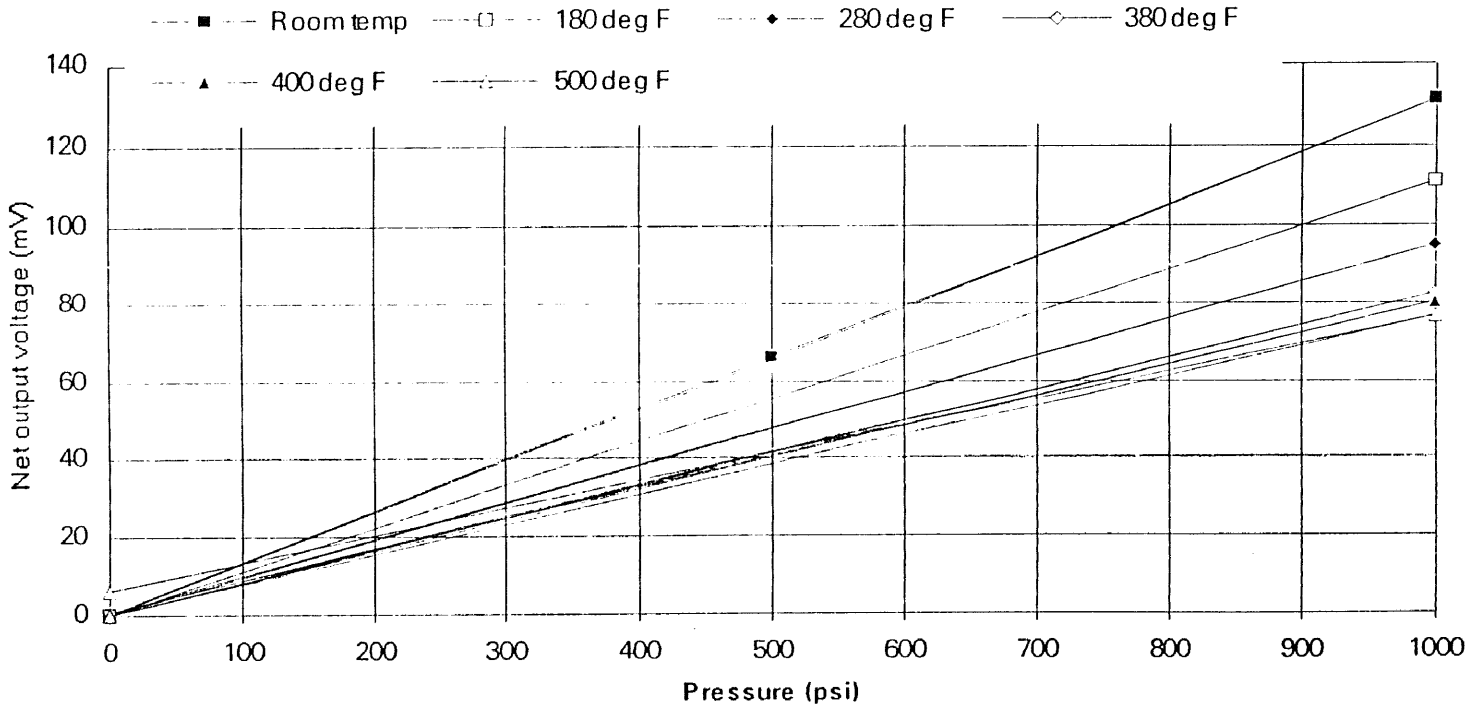

Figure 6-8

The effect of temperature on the functional dependence between the net output voltage and the applied pressure(n-type 6H-SiC, $N_d=1x10^{18}/cm^3$).

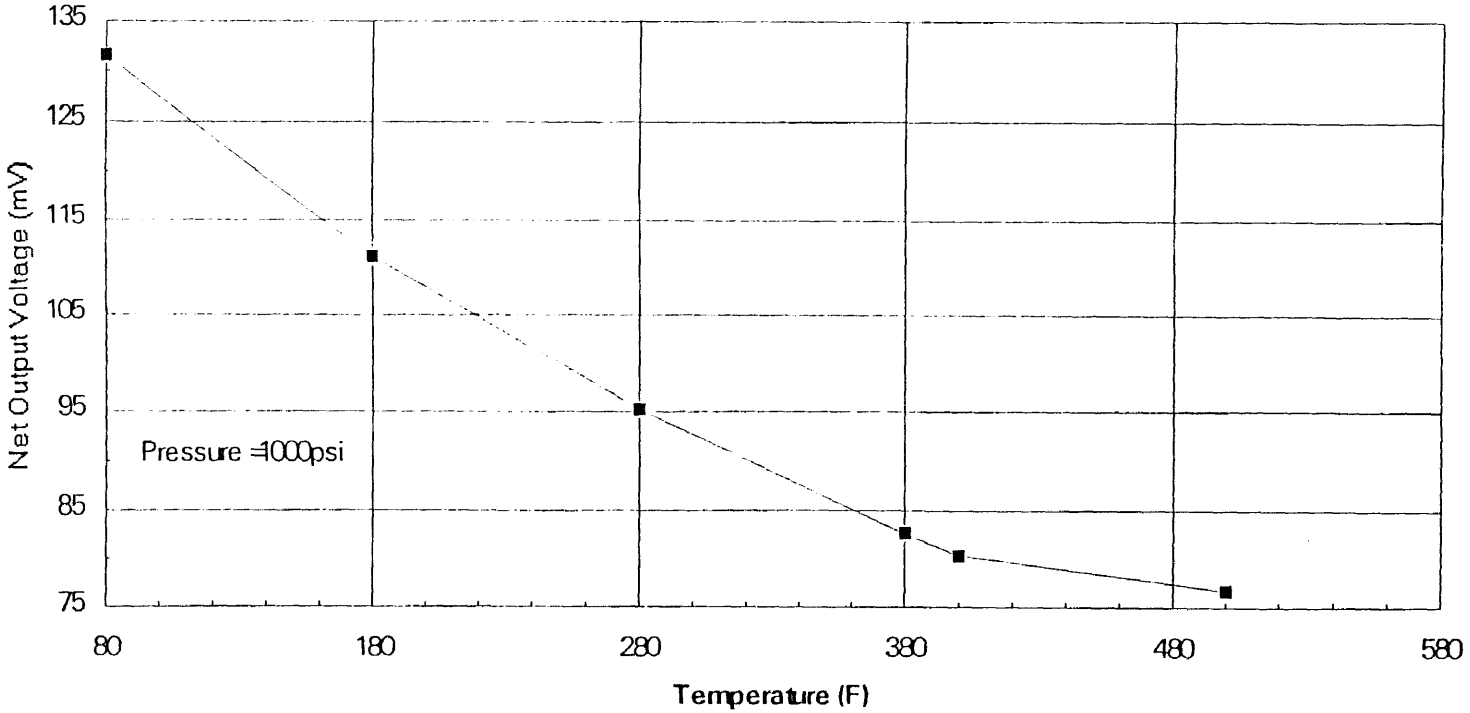

Figure 6-9
The effect of temperature on the net output voltage at constant pressure. (n-type 6H-SiC, $N_d=1x10^{18}/cm^3$)

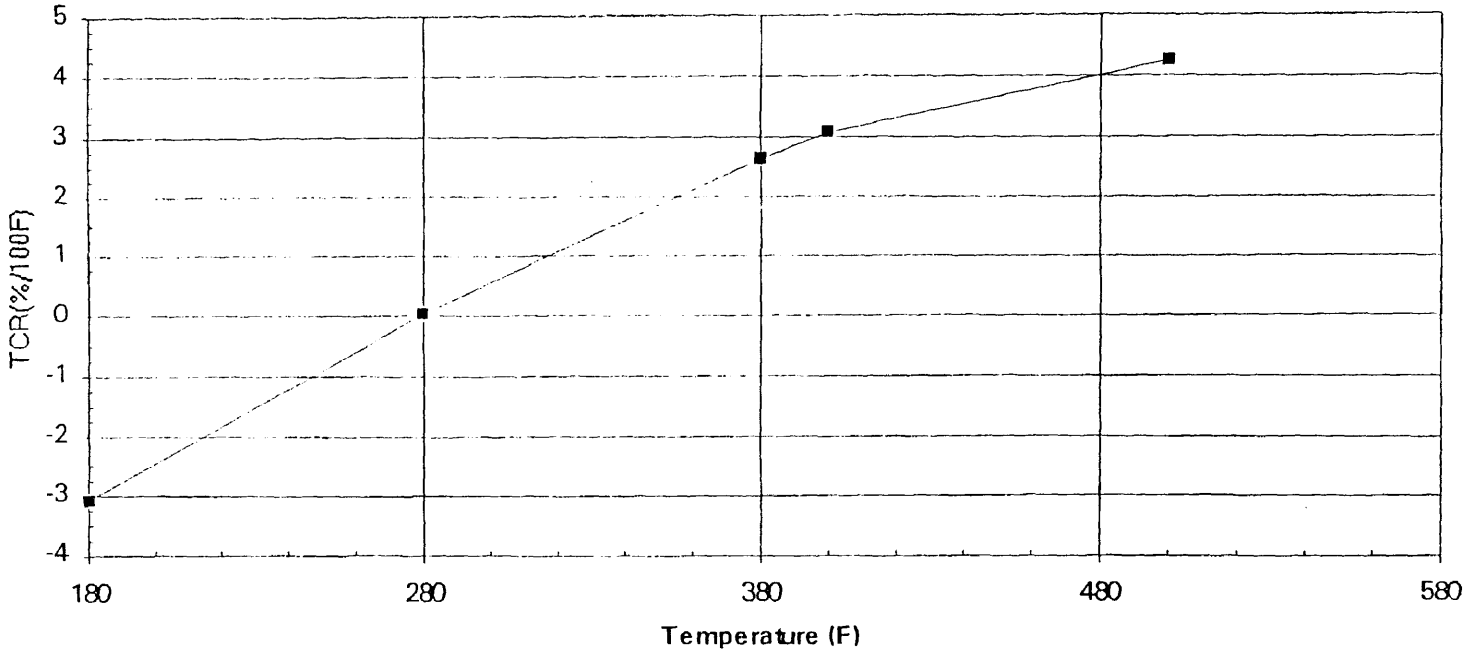

Figure 6-10

Dependence of the Temperature Coefficient of Resistance(TCR) on temperature(n-type 6H-SiC, N_d=1x10^{18}/cm^3).

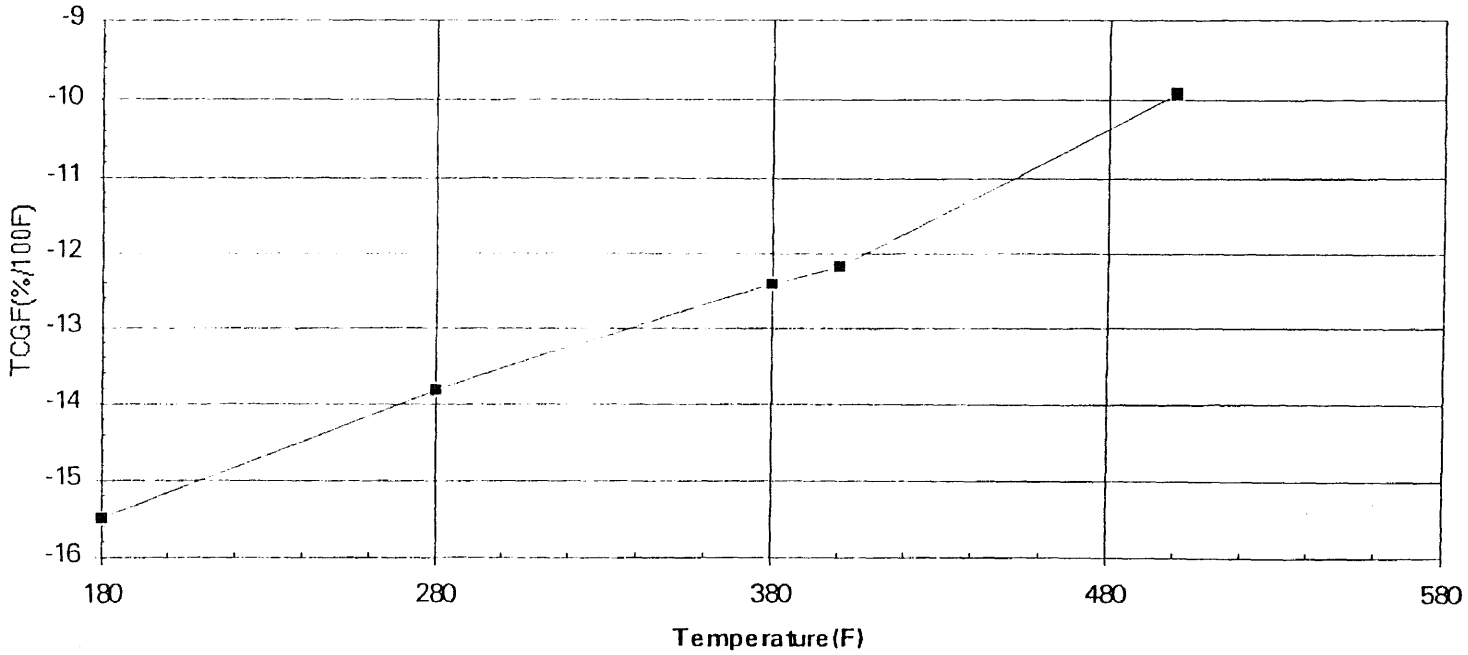

Figure 6-11

Changes in the Temperature Coefficient of Gage Factor(TCGF) with increasing temperature(n-type 6H-SiC, $N_d=1x10^{18}/cm^3$)

CHAPTER 7

CONCLUSIONS

A batch-microfabricated 6H-SiC diaphragm-based piezoresistive pressure sensors with working temperature range between 80°F to 580°F had been produced. The net output voltage shows an output voltage of 131.59mV at full-scale pressure of 1000psi. The net output voltage response to temperature up to 500°F was also presented. The temperature coefficient of resistance(TCR) of the device exhibited a TCR of -3.07%/100°F at 180°F and eventually becomes a positive value of 4.24%/100°F at 500°F. The temperature coefficient of gage factor(TCGF) exhibited negative values of -15%/100°F and -10%/100°F at 180°F and 500°F, respectively. The problem of micropipes in 6H-SiC was effectively resolved, making it possible to fabricate thin diaphragms of about 25 μm. Another prototype novel silicon carbide (6H-SiC) monolithic pressure sensor functional up to 580°F (305°C) was also developed and characterized.

This work demonstrated that two metallization schemes of Ti/TiN/Pt and Ti/$TaSi_2$/Pt had stable contact resistivity after treatment in air at 600°C for greater than twenty hours.

Longitudinal and transverse gage factors of n-type SiC, measured as a function of temperature and doping level, were found to be opposite in sign. The negative longitudinal gage factor (-25 at room temperature) increases with temperature and at 400°C assumes a constant value of -11. The positive transverse gage factor (+17 at room temperature) decreases gradually with temperature and at 400°C assumes constant value of +9. In absolute values, increase in the doping level results in decrease of the gage

factor. No substantial differences with regard to gage factors were found between n-type and p-type material.

The temperature coefficient of resistance (TCR) was found to be very much doping dependent. For each doping level it changes from negative at low temperature to positive at higher temperature, e.g. in low doped material ($1.8 \times 10^{17} cm^{-3}$) the resistance decreases up to room temperature and then increases. The higher the doping level the higher the temperature at which the change from negative to positive values occurs. The bridge gage factor increases linearly with pressure but decreases with rising temperature. The strain sensitivity was also found to be dependent on temperature. The higher the temperature the lower the strain sensitivity.

Photoconductive selectivity as method to fabricate structures on either n or p SiC was demonstrated. This principle was then utilized to fabricate piezoresistors in n-type epilayer were fabricated by applying photoelectrochemical etching. The p-type epilayer beneath the n-type epilayer served as an etch-stop. The newly developed process for resistors fabrication can be applied with minor adjustments to fabricate resistors in only n-type epilayer with any doping level.

This work also demonstrated preferential oxidation of porous SiC to facilitate good pattern definition and fast removal of residues. The thinning and the cavity etching to form the diaphragm was carried out by applying dark etching on the back side of the n-SiC wafer. The resulting cavities are etch-pits and hillocks free. The average etch-rates were found to be 0.6-0.8μm/min.

In closing, it should be said that this work represents a major progress in pressure sensor technology. It establishes the foundation for the application of SiC piezoresistive pressure sensors at high temperatures, beyond silicon technology. Research efforts toward this objective is continuing at Kulite.

7.1 Future Work

6H-SiC is known to be a material for use in high temperature environment. This research has demonstrated the capability of the high temperature metallization scheme to support sensor operation at 600°C. There is an on-going effort to resolve minor logistical issues before the device is tested up to 600°C. The surface morphology of the cavity reported in this work indicated the existence of some degree of roughness. Further research geared toward improving the morphology and pattern definition continues.

APPENDIX A

FABRICATION PROCESS FLOW

Step 1

Pre-oxidize the wafer in dry oxygen for five hours at 1150°C. Strip the oxide in BHF (Buffered Hydrofluoric Acid). Apply RCA cleaning procedure and subsequently dehydrate in Nitrogen ambient for twenty minutes at 225°C(fig. A-1).

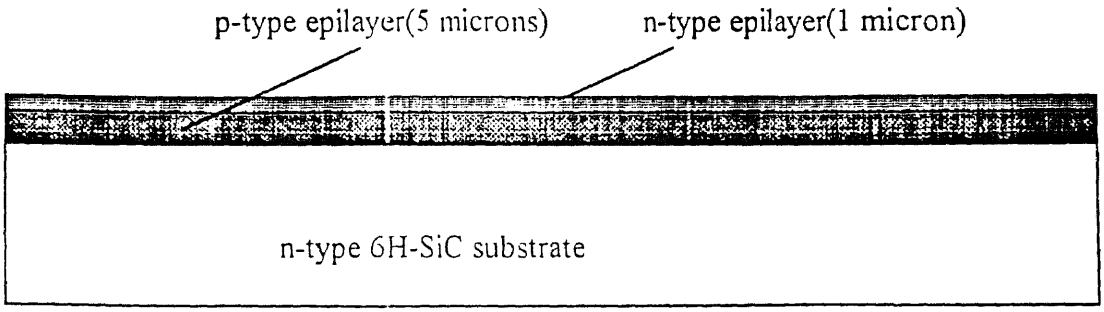

Figure A-1

Step 2

Use Aluminum to shadow mask the sample exposing only a small area in the corner of the sample (fig. A-2).

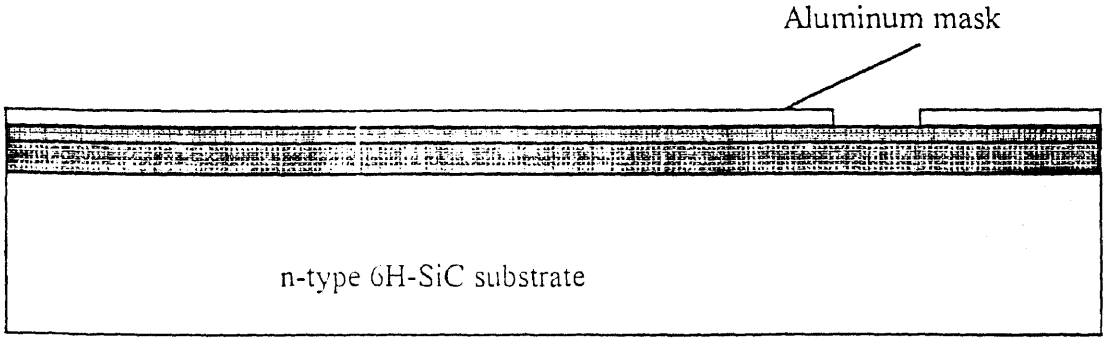

Figure A-2

Step 3

Deposit Titanium (1000Å) on the front side of the exposed area in the corner and subsequently remove the aluminum shadow mask (fig. A1-3). RTP anneal at 1000 C for 30 seconds.

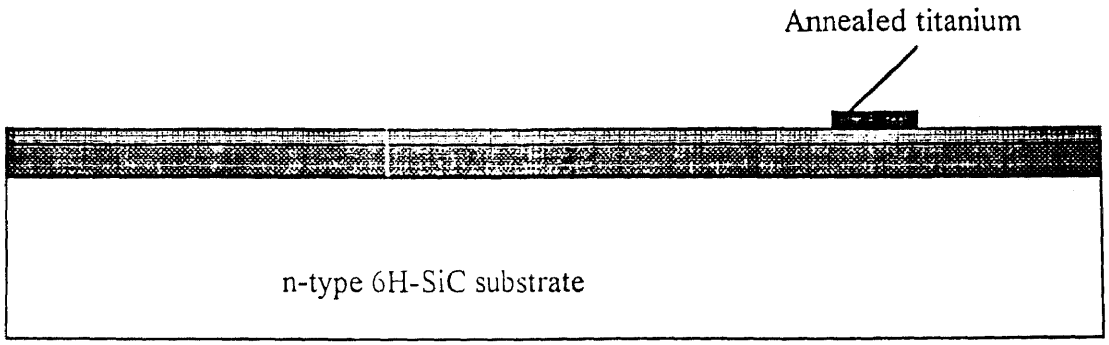

Figure A-3

Step 4

Deposit platinum layer (2000Å) on the front side. Coat with photoresist to define the resistors patterns on the platinum film. Etch the platinum layer in light aqua regia to create resistor mask patterns (fig. A-4). Strip photoresist and clean. Prepare the sample electrodes for anodization.

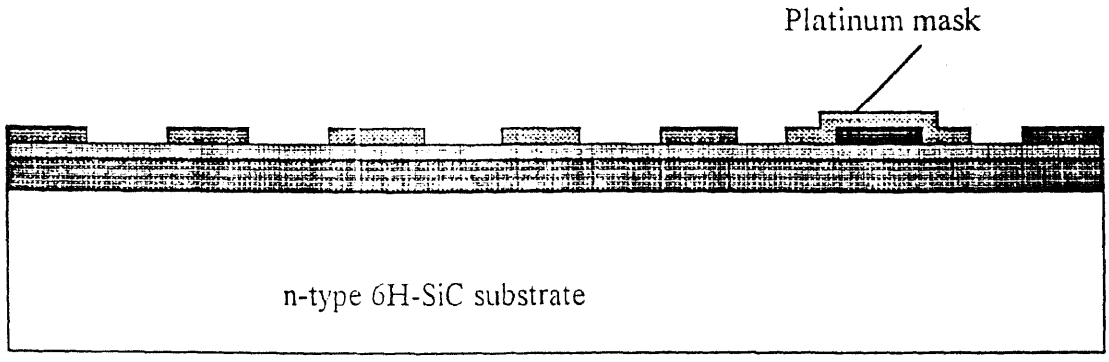

Figure A-4

Step 5

Etch sample photoelectrochemically under UV light. Strip the platinum mask and titanium ohmic contact. RCA clean sample. Selectively oxidize formed porous layer at 1150°C for two hours. Etch in 49%HF and rinse (fig. A-5).

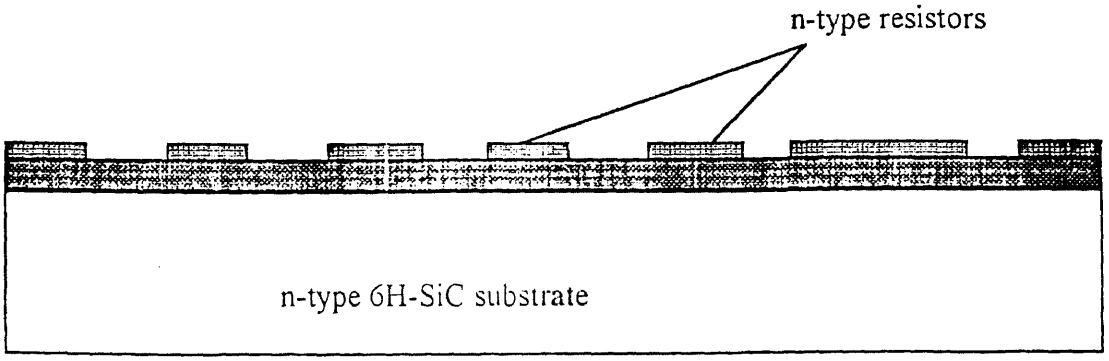

Figure A-5

Diaphragm Fabrication

Step 6

Deposit silicon nitride(2000Å), then quartz(1000Å) on back side of the wafer (fig. A-6).

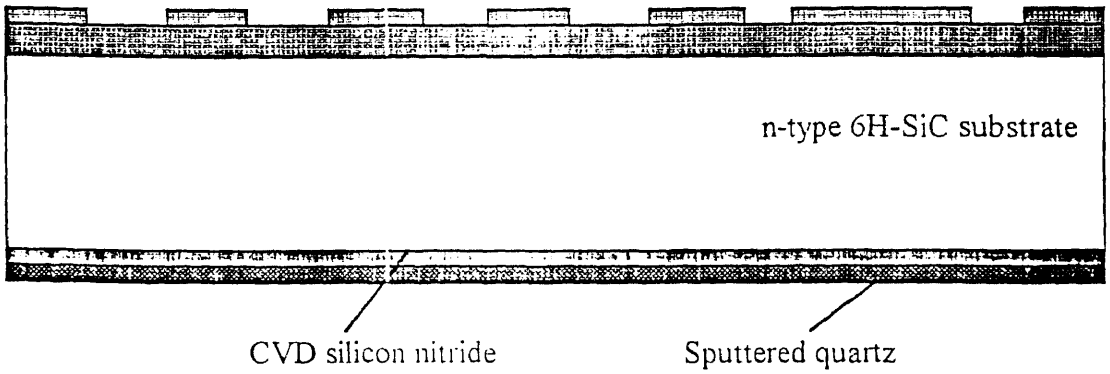

Figure A-6

Step 7

Apply photoresist and define in-plane dimensions of cavities by using photolithography. Etch quartz from the defined areas using BHF (Buffered Hydrofluoric Acid). Etch silicon nitride from the defined areas in hot (158 C) 85% phosphoric acid, using the self aligned quartz mask (fig. A-7). Apply RCA regime to clean the sample. Dehydrate the sample in Nitrogen ambient for 20 minutes, at 225 C.

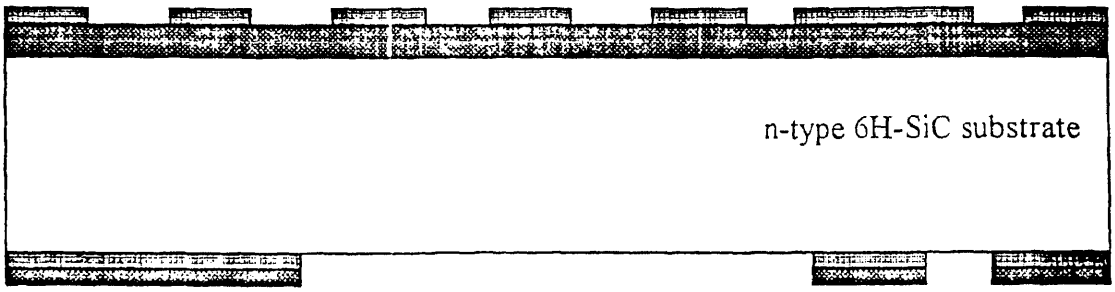

Figure A-7

Step 8

Use aluminum to shadow mask the sample leaving only a small area in the corner exposed. Deposit nickel (400Å) on the exposed area in the corner and subsequently remove the aluminum shadow mask (fig. A-8). RTP anneal at 1025°C for 30 seconds to obtain an ohmic contact.

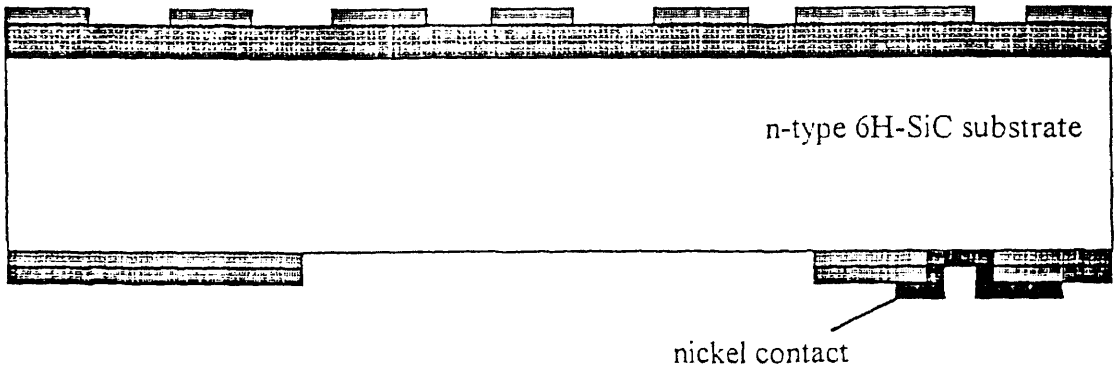

Figure A-8

Step 9

Prepare the sample for dark electrochemical etching, connect wires to the deposited nickel, encapsulate the sample in black wax, leaving exposed areas to be anodized. Anodize sample; Strip nickel, quartz, and silicon nitride after anodization (fig. A-9).

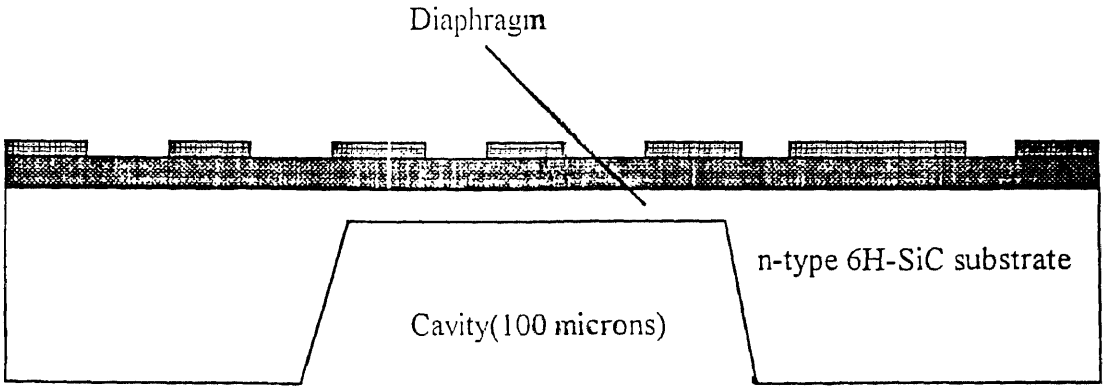

Figure A-9

Step 10

Oxidized sample; Define and metallization contact vias; Deposit Ti(1000Å)/$TaSi_2$(2500Å)/Pt(3500Å). Define metallization pads; Etch platinum in aqua regia; Etch Ti/$TaSi_2$ in buffered HF, Bond gold wires to platinum(fig. A-10).

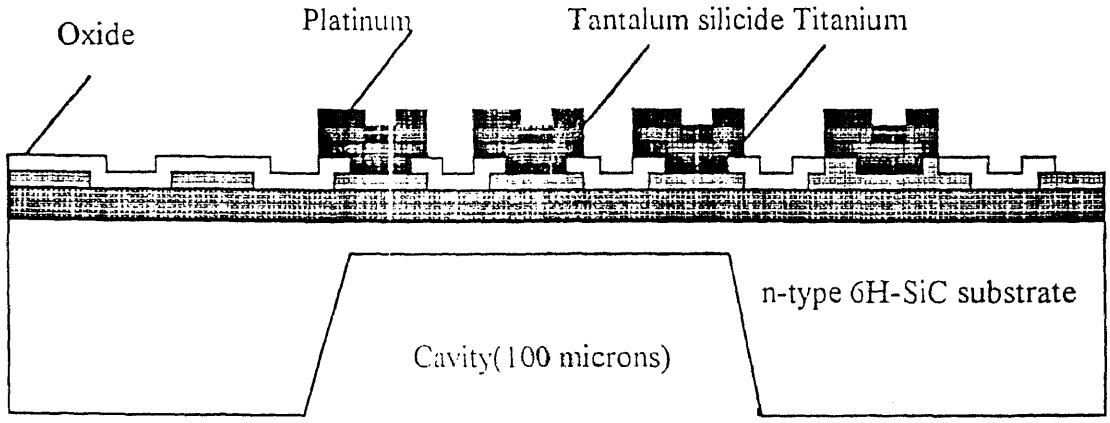

Figure A-10

APPENDIX B

SENSOR PERFORMANCE CHARACTERISTICS N-TYPE 6H-SIC PRESSURE SENSORS (N_d~$2x10^{19}cm^{-3}$)

Table B-1 First thermal cycle performance characteristics

Temp.(°F)	Characteristics	Sensor #1	Sensor #2
80	Max. Net Output(mV)	80.56	96.68
	Linearity(%/FSO)	0.6	0.94
	Hysterisis(%/FSO)	1.85	0.613
	Input Resistance(kΩ)	12.90	15.60
	Output Resistance(kΩ)	12.92	15.20
180	Max. Net Output(mV)	74.24	90.52
	Input Resistance(kΩ)	11.29	13.63
	Output Resistance(kΩ)	11.30	13.42
	Temp. Coef. Of Res.(TCR)(%/100°F)	-12.53	-12.66
	Temp. Coef. Of Gage Factor (TCGF)(%/100°F)	-7.85	-6.37
350	Max. Net Output(mV)	64.55	80.22
	Input Resistance(kΩ)	9.90	11.83
	Output Resistance(kΩ)	9.92	11.76
	Temp. Coef. Of Res.(TCR)(%/100°F)	-8.60	-8.95
	Temp. Coef. of Gage Factor (TCGF)(%/100°F)	-7.36	-6.30
450	Max. Net Output(mV)	59.63	74.40
	Input Resistance(kΩ)	9.55	11.28
	Output Resistance(kΩ)	9.56	11.26
	Temp. Coef. of Res.(TCR)(%/100°F)	-7.02	-7.48
	Temp. Coef. of Gage Factor (TCGF)(%/100°F)	-7.02	-6.22
80 (Return)	Max. Net Output(mV)	80.94	*
	Thermal null Shift(%/100°F)	0.24	0.46
	Thermal Null Set(%/FSO)	0.41	*
	Input Resistance(kΩ)	12.824	*
	Output Resistance(kΩ)	12.843	*

* Equipment failure.

Table B-2 Second thermal cycle performance characteristics

Temp.(°F)	Characteristics	Sensor #1	Sensor #2
80	Max. Net Output(mV)	79.39	93.90
	Linearity(%/FSO)	0.57	0.92
	Input Resistance(kΩ)	12.84	15.698
	Output Resistance(kΩ)	12.86	15.186
550	Max. Net Output(mV)	56.47	67.55
	Input Resistance(kΩ)	9.313	11.1
	Output Resistance(kΩ)	9.284	10.865
	Temp. Coef. of Res.(TCR)(%/100°F)	-5.85	-6.23
	Temp. Coef. of Gage Factor (TCGF)(%/100°F)	-6.36	-6.41
80	Max. Net Output(mV)	79.57	Unstable
(Return)	Thermal Null Shift (%/100°F)	-5.63	-4.52
	Thermal Null Set (%/FSO)	-4.2	-6.5
	Input Resistance(kΩ)	12.687	15.539
	Output Resistance(kΩ)	12.695	15.04

APPENDIX C

PERFORMANCE CHARACTERISTICS OF N-TYPE 6H-SIC PRESSURE SENSOR (N_d~$1x10^{18}cm^{-3}$)

Table C-1 Thermal performance characteristics

Temp.(°F)	Characteristics	Result
80	Max. Net Output(mV)	131.59
	Linearity(%/FSO)	.004
	Hysterisis(%/FSO)	.43
	Input Resistance(kΩ)	15.051
	Output Resistance(kΩ)	15.123
180	Max. Net Output(mV)	111.2
	Input Resistance(kΩ)	14.588
	Output Resistance(kΩ)	14.532
	Temp. Coef. Of Res.(TCR)(%/100°F)	-3.07
	Temp. Coef. Of Gage Factor(TCGF)(%/100°F)	-15.50
280	Max. Net Output(mV)	95.22
	Input Resistance(kΩ)	15.062
	Output Resistance(kΩ)	15.005
	Temp. Coef. Of Res.(TCR)(%/100°F)	0.04
	Temp. Coef. of Gage Factor(TCGF)(%/100°F)	-13.82
380	Max. Net Output(mV)	82.63
	Input Resistance(kΩ)	16.242
	Output Resistance(kΩ)	15.608
	Temp. Coef. of Res.(TCR)(%/100°F)	2.64
	Temp. Coef. of Gage Factor(TCGF)(%/100°F)	-12.4
400	Max. Net Output(mV)	80.33
	Input Resistance(kΩ)	16.532
	Output Resistance(kΩ)	16.414
	Temp. Coef. of Res.(TCR)(%/100°F)	3.07
	Temp. Coef. of Gage Factor(TCGF)(%/100°F)	-12.17
500	Max. Net Output(mV)	76.75
	Input Resistance(kΩ)	17.734
	Output Resistance(kΩ)	17.546

REFERENCES

1. Kulite Semiconductor Products, Inc. "6H-SiC Pressure Sensors for High Temperature Applications." *NASA SBIR Phase I Final Report*, (1992).

2. Geyling, F. T., and J. J. Forst. *Bell Syst. Tech. J.*, May, 1960. 705.

3. Lee, K. C. *J. Electrochem. Soc.* 137 (1991): 2556.

4. Kurtz, A. D., Nunn, T. A., and R. A. Weber. U.S. Patent #4,672,354 issued to Kulite Semiconductor Products, Inc., Leonia, NJ, 1987.

5. Pearson, G. L., Read, W. T., and W. L. Feldman. *Acta Met.* 5 (1957): 181.

6. Timoshenko, S., and S. Woinowsky-Krieger. *Theory of Plates and Shells*, Second Edition. New York. McGraw Hill. 1959. 402-404.

7. Samaun. "IC Piezoresistive Pressure Sensor got Biomedical Instrumentation." Ph. D dissertation, Dep. Electric Eng., Stanford Univ., Stanford, CA., Aug. 1971.

8. Rapatskaya, I. V., G. E. Rudashevskii, M. G. Kasaganova, M. I. Iglitsin, M. B. Reifman and E. F. Fedotova. *Sov. Phys. Solid State* 9 (1968): 2833.

9. Guk, G. N., N. Ya. Usol'tseva, V. S. Shadrin, and A. F. Mundus-Tabakaev. *Soviet Phys. Semicond.*, Vol. 8, No. 3, September 1974. 406.

10. Azimov, S. A., M. M. Mirzabaev, M. B. Reifman, O. U. Uribaev, Sh. Khairullaev, and Yu. M. Shashkov. *Soviet Phys. Semicond.*, Vol. 8, No. 11, May 1974. 1427.

11. Guk, G. N., V.M. Lyubimskii, E. P. Gofman, V. B. Zinov'ev, and E. A. Chalyi. *Sov. Phys. Semicond.* 9 (1974): 104

12. Cree Research, Durham, NC.

13. Ingo, Inc., Cleveland, OH.

14. Castigliano, A. *The Theory of Equilibrium of Elastic Systems and its Applications.* New York. Dover Publications. (1966). 248.

15. Herring, C., and E. Vogt. *Phys. Rev.* 101 (1956): 944.

16. Lely; J. A. *Bericht Deutsche Keram. Gesel.* 32 (1955): 229.

17. Davis, R. F., Z. Sitar, B.E. Williams, H. S. Kong, H. J. Kim, J. W. Palmour, J. A. Edmond, J. Ryu, J. T. Glass, and C. H. Carter Jr; *Mater. Sci. Eng.* B1 (1988): 77-104.

18. Davis, R. F., G. Kelner, M. Shur, J. W. Palmour, and J. A. Edmond. *Proc. IEEE* 79 [5], (1992): 677-701.

19. Edgar, J. H. *Mater. Res.* 7 [1], (1992): 235-252.

20. Shor, J. S., R. A. Weber, L. E. Provost, D. Goldstein, and A. D. Kurtz. "High Temperature Ohmic Contact Metallizations for n-type 3C-SiC Sensors." *Wide Gap Semiconductors*, Materials Res. Soc. Press, Boston, MA. (1992): 489.

21. Zeller, M. V., J. Bellina, N. Saha, J. Filar, J. Hargraeves, and H. Will. *Mat. Res. Soc. Symp. Proc.* 97 (1987): 283-288.

22. Wittmer, M., and H. Melchior. "Applications TiN Thin Films in Silicon Device Technology." *Thin Solid Films.* 93(1982): 397-405.

23. Kumar, N., J. T. McGinn, K. Pourrezaei, B. Lee, and E. C. Douglas. "Transmission Electron Microscopy Studies of Brown and Golden Titanium Nitride Thin Films as Diffusion Barriers in Very Large Scale Integrated Circuits."*J. Vac. Sci. Technol.* A 6 (3), May/Jun. 1988. 1602-1608.

24. Kuphal, E. *Solid State Elec.* 24 (1981): 69-78.

25. Ting, C. Y., and M. Wittmer. "The Use of Titanium-Based Contact Barrier Layers in Silicon Technolgy." *Thin Solid Films.* 96 (1982): 327-345.

26. Barin, I., and O. Knacke. *Thermochemical Properties of Inorganic Substances.* New York. Springer-Verlag. (1973): 696.

27. Murarka, S. P. "Refractory Silicides for Integrated Circuits." ."*J. Vac. Sci. Technol.*, 17 (4), Jul/Aug. 1980. 775-792.

28. New Jersey Institute of Technology, Dept. of Physics, Materials Science and Engineering Division.

29. Silicon Carbide-1973, ed. By R.C. Marshall, J.W. Faust and C.E. Ryan. Univ. Of S. Carolina Press. Columbia, SC, 1974.

30. Palmour, J. W., R. F. Davis, P. Astell-Burt, and P. Blackborow; *Science and Technology of Microfabrication* ed. By R.E. Howard, E. L. Hu, S. Namba and S.W. Pang. *Mat. Res. Soc.*, Pittsburgh, PA. 1987. 185.

31. Carrabba, M. M., J. Li, J. P. Hachey, R. D. Rauh and Y. Wang. *Electrochem. Soc. Extended Abstracts* 89-1 (1989): 727.

32. Shor, J. S., X. G. Zhang, and R. M. Osgood. *J. Electrochem. Soc.*, 139 (1992): 1213.

33. Shor, J. S., R. M. Osgood, and A. D. Kurtz. *Appl. Phys. Lett.* 60 (1992): 1001